ENVIRONMENTALLY ASSISTED CRACKING IN METALS UNDER EXTREME CONDITIONS

A Dissertation

by

HIEU HONG PHAM

Submitted to the Office of Graduate Studies of
Texas A&M University
in partial fulfillment of the requirements for the degree of

DOCTOR OF PHILOSOPHY

August 2011

Major Subject: Chemical Engineering

ENVIRONMENTALLY ASSISTED CRACKING IN METALS UNDER EXTREME CONDITIONS

A Dissertation

by

HIEU HONG PHAM

Submitted to the Office of Graduate Studies of
Texas A&M University
in partial fulfillment of the requirements for the degree of

DOCTOR OF PHILOSOPHY

Approved by:

Chair of Committee,	Tahir Cagin
Committee Members,	Perla B. Balbuena
	A. Amine Benzerga
	Mahmoud El-Halwagi
Head of Department,	Michael Pishko

August 2011

Major Subject: Chemical Engineering

ABSTRACT

Environmentally Assisted Cracking in Metals
under Extreme Conditions. (August 2011)
Hieu Hong Pham, B.S., Gubkin Russian State University of Oil and Gas
Chair of Advisory Committee: Dr. Tahir Cagin

Environmentally Assisted cracking (EAC) is a very critical materials science problem that concerns many technological areas such as petrochemical engineering, aerospace operations and nuclear power generation, in which cracking or sudden failure of materials may happen at stress far below the tensile strength. This type of corrosion is initiated at the microscopic level and is complicated due to the combination of chemistry (reaction caused by corrosive agents) and mechanics (varying load). As EAC is generally related to the segregation of impurity elements to defects (mainly grain boundaries), the symptoms of risk may not be apparent from the exterior of the metal components: hence EAC remains latent and gives no sign of warning until the failure occurs.

Due to its intricate nature, conducting experiments on this phenomenon involves difficulties and requires much effort. In this work, we employed advanced molecular simulation techniques to study EAC in order to give insight into its atomistic behavior. First, Density-Functional Theory (DFT) method was used to investigate the fundamental processes and mechanism of EAC-related issues at the nanoscale level, with two case studies concerning the stress corrosion in iron and hydrogen embrittlement in palladium. When segregating to the grain boundary (GB) of iron, different impurity elements such as sulfur, phosphorus and nitrogen raise corrosion failures in a variety of ways. Hydrogen atoms, due to their mobility and small atomic size, are able to form high occupation at crystal defects, but show different interactions to vacancy

and GB. Then, we used the classical Molecular Dynamics (MD) method to gain an understanding of the dynamic response of materials to mechanical load and the effects of temperature, strain and extreme conditions (high pressure shock compression) on structural properties. The MD simulations show that hydrogen maintains the highest localization at grain boundaries in the vicinity of ambient temperatures, and grain boundaries are the preferred nucleation sites for dislocations and voids. This computational work, using DFT and MD techniques, is expected to contribute to the better understanding on chemistry and mechanisms of complex environment-assisted cracking phenomenon at a fundamental level in order to beneficially complement conventional laboratory approaches.

To Mom and Dad

ACKNOWLEDGMENTS

I would like to gratefully thank Dr. Tahir Cagin for his guidance, support and encouragement over the last five years at Texas A&M University. He not only inspired me to study the world of computational materials science, but also has assisted me to develop the qualities and a foundation for becoming a true scientist. My gratitude is extended to the advisory committee, Dr. Perla Balbuena, Dr. Amine Benzerga and Dr. Mahmoud El-Halwagi for their time, kindness and useful suggestions to make this dissertation possible.

This is a great opportunity to express my appreciation to Dr. Sheng-Nian Luo for letting me take advantage of his expertise. I would also like to acknowledge Dr. Xiaowang Zhou for kindly providing me with the interatomic hydrogen-palladium potential that was used in this work.

My research and graduate study at Texas A&M would not have been the same without my group fellows; Bedri Arman, Justin Haskins, Oscar Ojeda, Alper Kinaci, Jennifer Carvajal, Cem Sevik, Kristen Williams, Jean Njoroge and Mousumi Mani. While their support and discussions were very helpful to my work, many outdoor social activities also brought an enjoyable environment to our laboratory.

A very special thank goes out to my Vietnamese companions, especially Linh T. Nguyen, Hao T. Nguyen, Hoa Q. Bui, Linh V. Nguyen, Hau T. Tran and others for making my stay in College Station a family-like experience. Last and definitely not least, this dissertation is dedicated to my parents whose constant care always kept me motivated about achieving my goals.

TABLE OF CONTENTS

CHAPTER Page

CHAPTER Page

LIST OF TABLES

LIST OF FIGURES

FIGURE Page

FIGURE Page

FIGURE Page

CHAPTER I

INTRODUCTION

A. Forms of Corrosion

Corrosion is a natural phenomenon readily seen everywhere in our daily lives. At home, it can be recognized on any metal tool or outdoor utensil. In industry, it affects all technological areas from petrochemical, mechanical, civil and nuclear to aerospace engineering. The durability and performance of many equipments and machine details significantly depend on their corrosion resistance. For instance, transformation of steel into rust by oxidation from atmospheric exposure reduces the serving time of pipelines, or an chemical plant needs a downtime schedule for corrosion-related maintenance and replacement. From economic impact, dealing with corrosion issue costs the US up to 4% of its gross natural product [1], and approximately an amount as much as one quarter of world's steel annual production is destroyed by corrosion each year [2].

In general, corrosion can be regarded as the loss of material or degradation of properties due to the reaction with its environment [3]. The cost of corrosion can be either direct or indirect. The direct losses involve the replacement of materials, equipments or machines impaired by corrosion processes. The indirect losses are incurred for cost of repair, maintenance, prevention or corrosion control, etc. In addition, problems such as loss of production, loss of life or environment contamination also cause considerable impact and addition to the total cost of corrosion [2].

The corrosion process occurs in a variety of ways or mechanisms and they can fit into one or more of the following categories [2]:

- uniform or general corrosion

The journal model is *IEEE Transactions on Automatic Control.*

- galvanic corrosion
- erosion and fretting corrosion
- crevice corrosion
- pitting corrosion
- dealloying corrosion
- intergranular corrosion
- environment-assisted cracking (stress-corrosion cracking, corrosion fatigue and hydrogen embrittlement)

Corrosion damages in the first six forms from the list above generally can by observed by visual investigation. However, the two latter types occur at microscopic or nanoscale level, which cannot be detected by external inspection. Intergranular corrosion is defined as the dissolution of grain boundaries (GBs) induced by impurity precipitations. Since the GB is a planar discontinuity where two single crystals meet, it serves as an ideal channel for the migration of atoms. Additionally, these boundaries have low coordination and are prone to mechanical damage as they are more brittle, compared to the bulk crystal. The presence of impurity elements may modify the GB energy and local crystal structure, including substantial changes in interatomic distances. Even when the cracks are initiated at GBs, the symptoms of the risk (of failure) may not be apparent from the exterior of metal or metal-alloy components of the structures, hence this type of corrosion remains latent and gives no signs of warning [4].

B. Environment-Assisted Cracking

Under certain conditions, the cracks or failure of materials happen at stress far below their tensile strength and this corrosion incident is known as environment-assisted

cracking (EAC). Actually EAC in metals is a very critical concern in areas such as petroleum, civil, aerospace operations and nuclear power generation [1]. Broadly, environment-assisted cracking includes a group of physical phenomena such as stress-corrosion cracking (SCC), corrosion fatigue (CF) and hydrogen embrittlement (HE). EAC is mainly caused by corrosive environments (depending on specific alloys and materials, different compounds of H, S, O, N, P, or Cl, etc can be responsible) and mechanical load (stress). Therefore, EAC is quite complicated since it is a combination of chemistry (reaction caused by corrosive agents) and mechanics (varying loads). Beside impurity elements, other environment factors involved in EAC may include high temperature, pH, electrochemical potential, etc [2]. Although the dissolution and diffusion of impurity particles responsible for corrosion may proceed without the assistance of stress, still the stress plays a major role in promoting crack initiation and growth [4]. More specifically, stress-corrosion cracking may be facilitated by static or residual stresses above some threshold value and corrosion fatigue can be initiated by fluctuating or cyclic stresses. Similar to intergranular corrosion, EAC is related to the dissolution of solutes, especially the ones with corrosive effects into host materials. In particular, the presence of defects such as vacancies and grain boundaries induces higher solubility of impurity atoms, and make materials more prone to cracking as a consequence. Stress corrosion may induce brittle cracks even in ductile materials. Depending on its circumstance, EAC failure can be either transgranular (ignoring grains) or intergranular (following grain boundaries). The latter case may resemble intergranular corrosion, as tensile stress can induce crack initiation along grain boundaries.

As mentioned above, due to its intricate and delayed nature, these processes are hard to be detected from inside materials' nanostructure until the failure has happened. Actually they have already accounted as the key reason behind many

major catastrophes, such as oil-pipeline failures, chemical plant explosions and bridge collapses [5]. The most well-known accident due to stress corrosion and corrosion fatigue was the collapse of the Silver Bridge over Ohio River in 1967, which resulted in loss of dozens of lives and multi-million capital cost. Hence, it is very important to understand and control the effects of impurities, extended defects and alloying in stress-corrosion for failsafe performance of materials and structures.

The goal of this work is to implement and use computational techniques to simulate processes at atomistic level for investigating the structure, properties, degradation and interactions of materials (various metals) in different conditions, including impurity segregation, defects, high temperature, strain or even more extreme such as high-pressure shock compression. This work is expected to contribute to the better understanding on chemistry and mechanisms of environment-assisted cracking phenomenon, in the context that its inherent nature is complicated and challenges the experimental studies in real-life laboratories. The next chapter presents literature reviews on crystal characterizations of metals with focus on defects, followed by a brief overview on EAC research, and available theoretical approaches for studying this phenomenon at atomistic level. The third and forth chapters detail our efforts to approach different issues by multi-scale simulation techniques (Density-Functional Theory and classical Molecular Dynamics, respectively). While part of this work has been published or in review progress, it is projected to yield totally six publications [6–11]. The dissertation is concluded by a summary along with proposed problems for future exploration in this area.

CHAPTER II

LITERATURE REVIEW

A. Crystal Characteristics of Metals

1. Crystal Structures

The properties of some materials may depend closely on their structures. Also, the same material may have exist at different structures depending on external conditions. For instance, carbon atoms arranged in various crystallographic systems will form allotropes with totally different physical properties, such as diamond, graphite, carbon nanotube or recently discovered graphene, etc. Another example is iron, which is a body-centered cubic (BCC) crystal at normal conditions, but can transform into face-centered cubic (FCC) or hexagonal close-packed (HCP) at high temperature and pressure.

The crystalline material is characterized by a long-range periodic array of atoms, i.e. a certain atomic group can be defined itself as a three-dimensional repetitive pattern. This small repeat entity is called a unit cell. The unit cell geometry can be completely described by a set of six lattice parameters: a, b, c (three edge lengths) and α, β, γ (three interaxial angles). Fig. 1 shows the conventional atomic configuration of a unit cell for several common crystal lattices. In metals, each atom has an identical number of its atomic neighbor, which is called the coordination number. Materials without this long-range atomic order belong to the amorphous or noncrystalline group.

Based on geometrical symmetry, there exist fourteen distinct crystal types called Bravais lattices [12]. These crystal lattices can be divided into seven groups of crystal systems, according to the possible combinations of lattice parameters (Table I). In

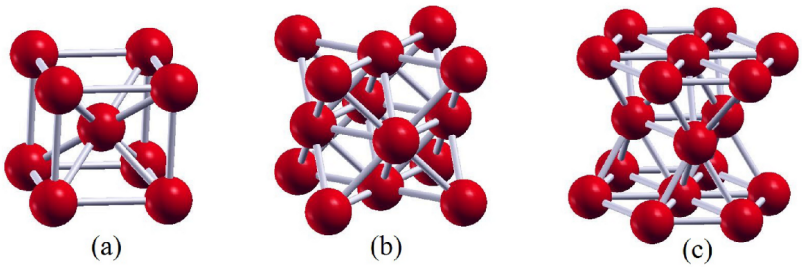

Fig. 1. Conventional unit cell of body-center cubic (a), face-centered cubic (b), and hexagonal close-packed (c) crystal structures

Table I. Bravais lattice types

Crystal system	Axial and angle relationships	Lattices
Cubic	a=b=c,α=β=γ=90°	simple body-centered face-centered
Tetragonal	a=b $\neq$ c,α=β=γ = 90°	simple body-centered
Orthorhombic	a $\neq$ b$\neq$ c,α=β=γ= 90°	simple body-centered face-centered base-centered
Monoclinic	a $\neq$ b$\neq$ c,α=β=90° $\neq$ γ	simple body-centered
Triclinic	a $\neq$ b$\neq$ c,α $\neq$ β $\neq$ γ $\neq$ 90°	simple
Trigonal	a=b=c,α=β=γ < 120 ° and $\neq$ 90 °	simple
Hexagonal	a=b $\neq$ c,α=β=90 °, γ = 120 °	simple

crystals, the properties of materials may vary depending on the crystallographic direction of its measurements. Materials therefore can be either isotropic or anisotropic, for which its properties are either independent or dependent of the direction of measurements. An crystallographic direction is defined as a vector passing through the origin of the coordinate system and has the length measured in terms of unit cell dimensions (a, b, c). For instance, the $\langle 110 \rangle$ direction is actually a reduced vector with projections on three x, y, z, axes respectively at a, b and zero points. In addition,

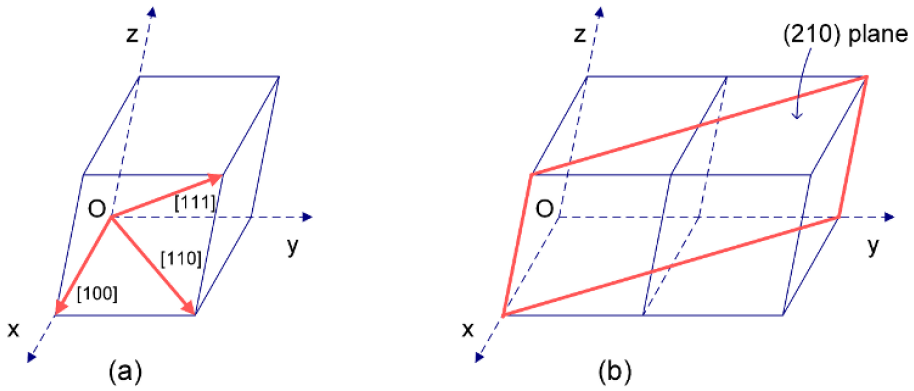

Fig. 2. Lattice directions and planes: (a) the [100], [110] and [111] directions within a unit cell; (b) lattice plane (210)

an effective study of lattice properties may require the definition of crystallographic planes which contain different lattice points. Similarly, a lattice plane can be specified by three so-called Miller indices as (hkl) [13]. All parallel planes are considered equivalent and therefore can be described by the same Miller indices. The procedure to identify Miller indices for a set of lattice planes is as follows: i) locate the intercept points of the plane with lattice axes, for instance at x = a, y = 2b, z = ∞ (when the plane is parallel to axis, as in Fig. 2, the intercept is taken to be at infinity) b) ii) find the reciprocals of these three numerical factors (i.e. 1, 2, $\infty \rightarrow$ 1, $\frac{1}{2}$, 0). The next step involves transforming these reciprocal numbers into three smallest integers (i.e. 1, $\frac{1}{2}$, 0 $\rightarrow$ 2, 1, 0). The resulting (210) is therefore Miller indices of the plane shown in Fig. 2b.

2. Crystal Defects

Crystalline materials that have atoms arranged in perfect order are called single crystals. Such idealized materials are very rare in nature; instead, they usually come with large number of imperfections or defects. More importantly, many properties

of materials, including electronic, chemical and thermodynamical properties, can be significantly influenced by presence of defects. In particular, the corrosion issues studied in this work is closely related to defect science. Based on dimensionality, defects can be classified into several groups, such as point defects (vacancy and interstitial), one-dimensional (dislocations), two-dimensional (grain boundaries, surfaces, interfaces) and three-dimensional defects (voids, pores). Relevant types of defects will be discussed in this section.

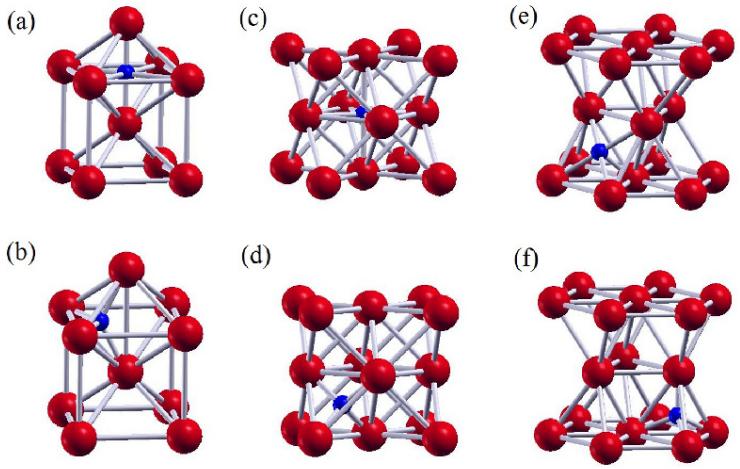

Fig. 3. Octahedral and tetrahedral interstitial sites (blue atom) in bcc (a, b), fcc (c, d), and hcp (e, f) crystal structures

a. Point Defects

Vacancy is probably the simplest type of defects in crystals. Due to some reason, atom is taken out of its position and leaves behind a missing or vacant site. In normal condition, fraction of vacancy number is insignificant, even it increases with temperature. The formation of multiple vacancies is also possible, leading to existence of voids or pores. A di-vacancy will consist of two vacancies forming at their nearest neighbor atomic sites. Phenomenon such as diffusion in metals, ceramics and

semiconductors is profoundly influenced by vacancies, in which the "flux" of vacancy can be generated by consecutive jumps of atoms into vacancy sites.

The "opposite" of vacancy is the interstitial. Because there always exists small empty space between crystal latices, another atom of the same type (intrinsic or self-interstitial) or an impurity atom (extrinsic interstitial) can find that as their occupation site. The most common types of interstice are octahedral and tetrahedral, in which the interstitial atom occupy the center of an octahedra or tetrahedra, respectively, formed by surrounding perfect lattices (Fig. 3). Beside vacancies, another diffusion mechanism of impurity atoms is through interstice.

b. Dislocations

Dislocation plays an important role in plastic deformation. This is a linear (or one-dimensional) defect of mismatched atoms. The first type, edge dislocation, is induced by an extra half-plane of atoms (Fig. 4a). The edge of this half-plane (AB) ends within the crystal and is called the dislocation line. Because of this insertion of atomic plane, original atoms above dislocation line are more compressed while ones below are more expanded. The second type, screw dislocation, can be formed by the distortion that shift some portion of atoms by one atomic distance (Fig. 4b). Again, the misalignment of atoms is along its dislocation line (AB). In real materials, a mix of both types can be found and it is called a mixed dislocation in that case.

c. Grain Boundaries

When the solid is formed from liquid, differently oriented crystallites grow until they border on each other. The boundary between these grains contains a surface across which atoms change their orientation. Despite the gaps and distortion, grain boundary width is small so that cohesion of atoms at grain boundaries is sufficiently strong

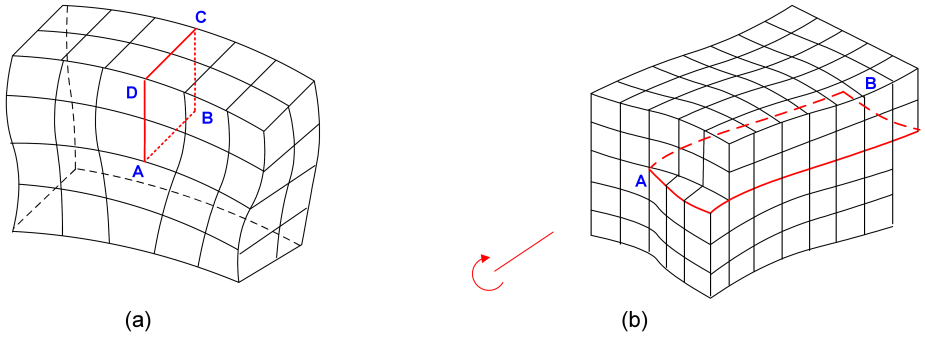

Fig. 4. Schematic representation of edge (a) and screw (b) dislocations

to keep component grains united. However, due to lower coordination number, atoms located at grain boundary have higher energy in comparison to bulk material. Grain boundaries therefore can act as a driving force to pull impurity particles and become sources for atom segregation, in tendency to reduce its energy. For these reasons, grain boundaries are more prone to mechanical weakness. The studies using electron spectroscopy proved that stress-corrosion cracking is usually related to the segregation of impurity or solute atoms to the grain boundaries, which results in grain boundary weakening [14]. Also, grain boundary diffusion is much faster than that in the corresponding bulk.

The misorientation of a grain boundary can be described by a rotation required to bring two adjoining grains back to perfect matching. This rotation is fully specified by a rotation axis $\mathbf{u}$ and a rotation angle θ. Fig. 5 presents two types of grain boundaries. When the rotation axis $\mathbf{u}$ is parallel to the boundary plane, this type is called a tilt grain boundary. The other type is the twist grain boundary that has rotation axis normal to boundary plane. Sometimes a mixed grain boundary can have both tilt and twist components. In addition, when the atoms on one side of grain boundary are symmetrical to those on the other side, this special type is called a twin

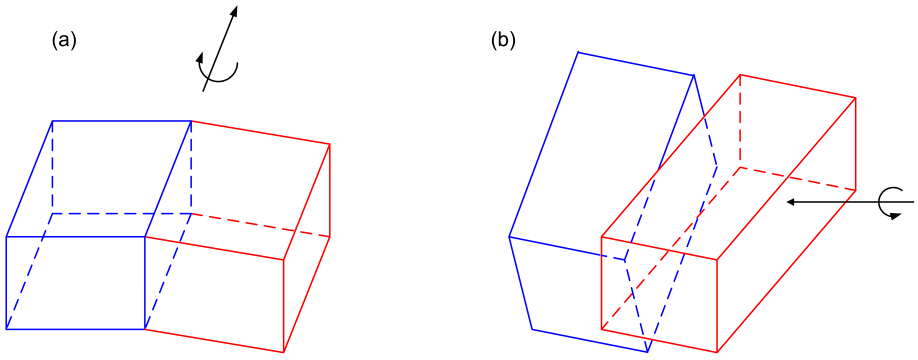

Fig. 5. Schematic descriptions of tilt (a) and twist (b) grain boundaries

boundary. Based on the degree of rotation, a grain boundary can be specified as low or high-angle.

Certain combination of rotation parameters can result in the coincidence of lattice points from two grains. The coincidence site lattice (CSL) theory suggests that grain boundary energy depends on the portion of coincidence sites. If there are more atoms coinciding between two grains, less energy is required to generate the grain boundary, since less atomic bonds are broken [15, 16]. The density of coincidence is a very important factor in CSL model and its reciprocal is denoted as an Σ number. For instance, there is 1 in every 5 lattice sites are in coincidence for a $\Sigma 5$ grain boundary. Σ values are always odd numbers in cubic system [16, 17].

For a symmetrical tilt grain boundary in cubic crystals, the Σ value and three Miller indices (hkl) of grain boundary plane can be related to each other through the following relation [16, 17]:

$$\Sigma = h^2 + k^2 + l^2 \quad if \quad h^2 + k^2 + l^2 \quad is \quad odd \tag{2.1}$$

$$\Sigma = \frac{h^2 + k^2 + l^2}{2} \quad if \quad h^2 + k^2 + l^2 \quad is \quad even \tag{2.2}$$

Using this equation, symmetrical tilt grain boundaries on (120) and (130) planes

in cubic crystals will all belong to the group of Σ 5 (1^2+2^2+0^2=5 and $\frac{1}{2}$(1^2+3^2+0^2)=5).

B. Overview on History of Environment-Assisted Cracking Research

Environment-assisted cracking was recognized as a serious engineering problem in late 1800s, when consecutive failure cases on steam boilers and brass equipments due to service conditions were reported [18]. EAC since then became a very important research area, when the development of industry and manufacturing came with growing concerns about service failures induced by environments. To these days, many aspects of this phenomenon remained unclear despite a tremendous volume of literatures and laboratory studies. This report therefore is only aimed at covering briefly main progresses of EAC research throughout its history. The author acknowledges in advance Shipilov [19], Lejček [16] and Flewitt et al [5], from which this overview significantly benefited.

Discovery of this phenomenon and pioneering contributions in this area credit the works of W. H. Johnson, O. Reynolds, W. Roberts-Austen and Adolf Ledebur in late nineteenth century, in which they conducted earliest tests on the loss of ductility of metals and alloys under exposures to selective acid and caustic environments. Towards the mid-twentieth century, EAC studies mainly focused on identifying combinations of materials and environments that lead to corrosion cracking and on explaining its mechanics. Copper (brass) and ferrous alloys (steels) drew great interest, motivated by cracking troubles with their popular usages in construction and military operations. Series of failures of brass bolts and brass cartridge cases, explosions of steam boilers and vessels were well documented during that period of time [19]. It was recognized that cracks can be either intergranular in some cases or transgranular in others.

Several early theories on EAC mechanisms were then developed and received

wide attention [19]. Electrochemical theories are based on the postulate that cracks progress along continuous localized paths such as grain boundaries, under segregation of chemically reactive elements. Due to the difference in chemical potential, those paths are more susceptible to corrosion and become sources of stress concentration. Sufficient stress might lead to mechanical fracture and as a result metal tears apart. The film theory, however, attempts to explain the crack initiation at grain boundaries through the local rupture of protective oxide films. The oxide films formed over grain boundaries are more easily broken than those formed over metal surfaces. Therefore, susceptibility to stress-corrosion cracking is subject to properties of these oxide film layers. Another hypothesis, called mechanical theory, elucidate the branching of cracks by suggesting that crack propagation can be arrested when it encounters obstacles such as grain boundaries or lattice discontinuity. As a result, while the process slows down and needs more corrosion or stress concentration at the crack tip to advance, the corrosion attack may happen on sides of cracks and lead to crack branching. In order to explain SCC in homogeneous alloys and transgranular cracking phenomenon in some metals, strain-accelerated decomposition theory was presented as an extension to electrochemical theory. This theory suggests that material in the vicinity of crack tip is decomposed faster than the metal bulk. As a result, local straining stimulates the formation of new phase with lower chemical potential (anodic) and accelerates crack propagation.

For decades from mid 20^{th} century up to now, significant efforts were dedicated to a better understanding of SCC mechanics. Also, crystal defects and their role as a key factor in SCC drew increasing attention. New testing methods and techniques offered exclusive possibility to study electronic structures of interfaces and grain boundaries. McLean, Ishida, Hondros and Seah [20–23] are among the pioneers who studied the energetics of surfaces and grain boundary segregations. The investigations on ki-

netics, chemistry and influences of impurity segregation in metal interface and grain boundaries were then pursued by numerous investigations [14, 24–32]. The effects of alloying and impurity elements to grain boundary segregation were reported for many metallic and non-metallic systems, including Fe, Cu, Ni, Al, Cr, Co, W, etc. and their alloys [33–38]. In addition to intergranular SCC, the film-induced cleavage mechanism was developed by Sieradzki and Newman to discuss about transgranular stress-corrosion cracking as observed in several metals [39].

Also, hydrogen embrittlement became an important research area [40] and it was accepted that elastic response of hydrogenated metals and alloys changes due to the lattice relaxation and local hydrogen excitation [41, 42]. Several major hydrogen embrittlement mechanisms have been widely established, including (i) hydrogen-enhanced localized plasticity (HELP) [43] (ii) stress-induced hydride formation [44], and (iii) lattice, grain boundary (GB) and interface decohesion [45].

The 1980s are marked with an significant achievement in accurate modeling of materials problems, thanks to the advances in computer resources and simulation techniques. During the early computational studies on this problem, Hashimoto, et al. [46–49] studied the grain boundary segregation in Fe-P and Fe-B alloys with molecular dynamics method, using Morse potential to describe the interatomic interactions. Briant, et al., also developed an electronic model to predict the GB embrittlement in iron and nickel-based alloys, in which the charge was reportedly drawn from the host to impurity atoms and resulted in the weakening of bonds [50–53].

In 1990s, availability of *ab initio* techniques make simulation works on the electronic structure and geometry of grain boundaries more affordable. The first-principles calculations using the full potential augmented plane wave method was successfully employed by Painter, Wu, Geng, Freeman, Yamaguchi et al., etc. to determine the intergranular influences of various impurity elements on Fe, Al and Ni grain bound-

ary and interface cohesion [54–62]. Besides calculating the changes in electron density to specify whether the precipitates weaken or strengthen the bonding between host atoms, they also applied the concept of binding energy difference at GB and fractured free surface [63] to determine the effect of impurity atoms. More recently, grain boundary supercell models have been further used by many groups to investigate the decohesion effects in Ni and Fe GB through the DFT-based relaxation of GB cell and tensile tests [64–71]. It was reported that both the tensile strength and cohesive energy of Ni and Fe GB reduce under S segregation, and the repulsion among neighbor S atoms cause a large GB expansion.

Despite a long history of recognition and investigation, there are still multiple questions about environment-assisted cracking in many metals and alloys needed to be clearly answered, namely at nano-scale or atomistic level; for instance, how the accumulation of corrosive elements induces the crack initiation, in which mechanism the hydrogen atoms degrade mechanical properties of metals when binding to different kinds of defects, what are the roles of vacancy and grain boundaries in impurity segregation, etc. In this work, we use start-of-the-art approaches (Density-Functional Theory and Molecular Dynamics simulations) to present detailed studies for several issues in EAC area, for selective metals. In addition, since materials in many key applications today, such as nuclear engineering and space operations, are commonly exposed to hash environments; we will also address the effects of extreme conditions, including high temperature, strain and high-pressure shock compression to thermodynamic and mechanical properties. The next section will discuss the principles of molecular simulation methods employed in our work.

C. Computational Approaches to Study Materials Science Phenomena in Solids

Test methods and experimental studies of environment-assisted cracking face many challenges due to the complicated nature of this phenomenon. First of all, this is an delayed process that requires an crack growth in multiple stages. The time limit of experiments therefore necessitates certain techniques to accelerate the EAC progress without affecting its mechanism and outcomes. In addition, other problems arise from the control of electrochemical and mechanical conditions at the crack tip, which are changing and difficult to evaluate during the test [1].

EAC tests can be conducted on materials by controlling either the strain or the stress load. In some case, the precracked specimen are used, i.e. the cracks were initiated in the specimen before the actual test by means of tensile or cyclic stress. This type of experiments provides information about crack propagation and threshold stress but doesn't allow one to study the crack initiation mechanism. In non-precracked samples, however, the crack initiation and growth during the test can pronounce the sensitivity of materials in selective environments to corrosion cracking.

The chemical composition of crack tips (in many cases, start at crystal defects such as vacancies, dislocations and grain boundaries) can be detected by various techniques. When the crack paths are revealed by brittle intergranular fracture, surface analysis such as Auger electron spectroscopy (AES) [72] and secondary ion mass spectroscopy (SIMS) [73], can be employed to study the chemistry and characterization of these open surfaces. However, these methods require strict conditions to preserve the fresh fracture surfaces from contamination by environment elements, which as a consequence may alter analysis results [16]. Microscopic techniques overcome these disadvantages by allowing one to conduct the measurements and obtain images of interfaces without cleavages (for instance, at grain boundaries). Major parts in this class

include analytical electron microscopy (AEM) and atom-probe field ion microscopy (AP FIM). AEM is capable of detecting the segregation sites of impurities but is ineffectual in analyzing light elements. AP FIM, on the other hand, can provide clear crystallographic observation and information on all elements. However, preparation of test specimen for all microscopic techniques above have never been easy; in fact, it is very complicated and time-consuming [16].

In recent decades, thanks to great advances in theory, simulation techniques and computer power, different computational methods were employed as effective tools to shed light on chemistry and physics of molecular interactions. Despite the fact that outputs of molecular simulations are never totally reliable, their employment meets revolutionary advantages [74]. First of all, the successful development and usage of good molecular models minimize the labor, expense and time required to prepare the real compounds. Some complex molecule systems can be modeled and computationally tested prior to being synthesized in laboratories. Secondly, computational chemistry and physics allow one to understand the phenomena more thoroughly by giving insights into atomistic or molecular behaviors, which hardly can be obtained from classical experimental methods. While the laboratory experiments present the phenomenon, the computation may explain its mechanism. Therefore, this information gives supplementary understanding, or can be used as a guideline for future experiments.

At nanoscale level, the atomic forces can be evaluated by different methods, such as quantum mechanics principles and interatomic potentials. The first approach is based on first-principles calculations from solution of many-electron Schrödinger equation. The latter can be either empirical or semi-empirical since the properties of materials or interactions between atoms are described in interatomic potentials, whose development requires the input from experiments or other first-principles calculations.

1. Quantum Mechanics and Density-Functional Theory

Quantum mechanics approach is precise but very complicated and time-consuming. In this method, the quantum state of electrons and nuclei is described by a wave function, or state function of coordinates and time Ψ(x,t). Because the location of subatomic particles can never be predicted exactly, the wave function therefore returns probability amplitude of position or momentum. In fact, some pairs of physical quantities such as position and momentum, energy and time, can simultaneously estimated only to a certain degree of precision, as stated in Heisenberg uncertainty principle:

$$\triangle x \triangle p \geq \frac{\hbar}{2} \tag{2.3}$$

where $\hbar$ is the reduced Planck constant; x and p are position and momentum of the microscopic particle, respectively. Electronic properties and energy of atomic systems in quantum mechanics are obtained by solving the time independent Schrödinger equation:

$$\hat{H}\Psi(x) = E\Psi(x) \tag{2.4}$$

where $\hat{H}$ is the Hamiltonian operator. For the non-relativistic Schrödinger equation, the Hamiltonian in general contains terms corresponding to kinetic ($\boldsymbol{T}$) and potential energy ($\boldsymbol{V}$) of the system. Since the nuclei are much heavier and their motions are at much larger time-scale (in comparison with electrons), their dynamics can be described by classical Newtonian physics, instead of Schrödinger equation, and electronic configurations can be decently assumed to be at ground state [75]. Therefore, the Born-Oppenheimer approximation simplifies this equation by decoupling the electronic and nuclear dynamics and the Hamiltonian can be broken down to the

form [75]:

$$\begin{aligned}\hat{H} &= \sum_{I}^{nuclei} \frac{p_I^2}{2M_I} + \sum_{i}^{electrons} \frac{p_i^2}{2m_i} + \sum_{i>j}^{electrons} \frac{e^2}{r_{ij}} + \sum_{I>J}^{nuclei} \frac{Z_I Z_J}{R_{IJ}} - \sum_{I}^{nuclei} \sum_{j}^{electrons} \frac{Z_I}{R_{Ij}} \\ &= T_N + T_e + V_{ee} + V_{NN} + V_{Ne} \end{aligned} \tag{2.5}$$

where the first two terms represent kinetic energies of nuclei and electrons, respectively. The latter are contributions from electron-electron, nuclear-nuclear and nuclear-electron interactions. Still, the exact solution of quantum mechanics equations can not be obtained for system with more than one electrons.

In practice, different theories were proposed for approximating the energy and properties of multiple-electron systems. Each approach in turn is accurate and valid for only a selective set of problems and materials and requires sophisticated manipulations. Recently, Density-Functional Theory (DFT) [76] has become one of the most popular and reliable methods for studying condensed phases at electronic level. It states that energy of a many-body system can be obtained from particle density, instead of wave function. More specifically, the ground-state energy is a *functional* of the electron density ρ, and has the minimum value with respect to its variation $\delta\rho$. Since electron density ρ is also a function, the energy functional is a function of a function. The electron density is obtained from the summation of all individual one-electron orbitals that represent each non-interacting reference system.

$$\rho(r) = \sum_{i} |\psi_i(r)|^2 \tag{2.6}$$

and total energy functional contains the following terms [75]:

$$E[\rho] = T[\rho] + V_{ee}[\rho] + V_{Ne}[\rho] + E^{xc}[\rho] \tag{2.7}$$

in which T[ρ] is the kinetic energy, V$_{ee}$[ρ] is the electron electron repulsion, V$_{Ne}$[ρ] is

the electron-nuclear attraction and $E^{xc}[\rho]$ is the exchange-correlation energy. Since the explicit forms of $T[\rho]$ and $E^{xc}[\rho]$ are unknown, it requires employments of further reductions.

The first approximation introduced is the local density approximation (LDA) method, in which the functionals ($T[\rho]$ and $E^{xc}[\rho]$) for a single electron are assumed to be equal to corresponding energies of an electron in homogeneous electron gas at the same local density. This method can legitimately give precise predictions of crystal structure and macroscopic properties, but underestimate lattice parameters due to its overestimation of cohesive binding. In addition, the energies of state and Van der Waals interactions may not be appropriately estimated [75]. To correct these deficiencies, another method was proposed as generalized-gradient approximations (GGA) [77–79]. This approximation includes the dependence of $E^{xc}[\rho]$ on local variations of electron density $\delta\rho$. Despite owning some limitation such as incorrect description of hydrogen bonds, this GGA implementation sufficiently corrected the shortcoming of LDA method.

The last unknown in the Hamiltonian above is description of electron-nucleus interactions, in order to calculate wavefunctions $\psi_i(r)$. This can be done by an appropriate choice of basis sets, some are already well-developed and proven effective, such as linear combinations of atomic orbitals (LCAOs), linearized augmented plane waves (LAPWs) and plane-wave/pseudopotential approaches [75].

Presently, Density-Functional Theory is one of the most precise methods to study many physics and chemistry phenomena at electronic level. However, since it deals with ground state energy and neglect the thermal contributions, all properties and calculations from DFT correspond to those at absolute zero temperature.

2. Interatomic Potentials and Classical Molecular Dynamics Methods

Another effective method to calculate the energy of molecular system is by so-called interatomic potentials. Simple approaches were first presented in form of pairwise potentials, in which internal energy depends merely on interatomic distances. For example, the internal energy based on Lennard-Jones model has a simple form as:

$$U = \frac{1}{2}\sum_{i \neq j}(-\frac{A}{r_{ij}^{6}} + \frac{B}{r_{ij}^{12}}) \tag{2.8}$$

where A and B are parameters and in general, these parameters are obtained from fitting basic properties to results either from first-principles calculations or experiments. Despite pair potentials have been successfully developed and applied to study certain simple materials and properties [16], they fail to fully reproduce the physical properties of crystalline materials, as the role of electron density and the atomic bonding in pair potentials are underestimated. For instance, pure pair potentials imply the Cauchy relation between elastic constants $C_{12} = C_{44}$, which is not necessarily true in real metals and alloys. Also, stacking fault energies, surface structure and relaxation properties cannot be accurately estimated while using pair potentials [80]. Many-body models overcome these limitations by properly treating the essential band character of the metallic bonding. The many-body potentials describe interatomic interactions as a combined effect of a short-range pair-wise repulsion and a many-body density dependent cohesion. Over the past decades, a collection of many-body potentials has been developed, including those based on effective medium theory [81], embedded atom method [82], as well as those based on the tight-biding approach, such as the Finnis and Sinclair [83], Sutton and Chen [84] and the RGL model [85]. Among them, embedded atom method, for instance, is a quite an effective technique

used for crystal and solid phase.

$$E_c = \sum_i G_i \left(\sum_{j \neq i} \rho_j^a \left(R_{ij} \right) \right) + \frac{1}{2} \sum_{j \neq i} U_{ij} \left(R_{ij} \right) \tag{2.9}$$

where the first term stands for the embedding energy and ρ is the background atomic electron density. The second term is related to the contribution from all cross-pair atomic interactions.

The second step in this method requires an good algorithm to keep track of the atomic motions and obtain equilibrium structures. Some of the most popular techniques include molecular statics (MS), molecular dynamics (MD) and Monte-Carlo (MC) simulations. While MS and MC methods were not used in this work, the focus here is directed to principles of MD. The nuclear time-dependent motions of particles in MD simulation technique is based on classical Newtonian mechanics [86], in which the interactions between atoms are characterized by the interatomic potentials explained above. The MD method inherently neglects the quantum mechanical effects, therefore make a great simplifications for phenomena where quantum effects are insignificant or unimportant. Provided decent interatomic descriptions, MD methods can be accurate in calculating many macroscopic properties (elasticity, thermal expansion, etc [87]) or simulating many physical phenomena (diffusion, shock propagations, etc [88]). A big advantage of MD method over quantum mechanics is that it allows one to include the thermal effects, therefore the calculations can be performed for any elevated temperature.

The MD simulation is usually started by a initial distribution of particle positions and velocities, to conform with the atomic structure and desired temperature. Having the knowledge of interaction energies between neighbor atoms (from the potentials) the forces acting on each particle are then computed. Based on atomic forces, the Newtonian equation of motions can be integrated to find new positions and corre-

sponding particle velocities and forces. This iteration is repeated until the structure reaches its equilibrium state.

MD simulation is actually a scheme for time evolution of molecular system. During iteration steps, introduction of various constraints (such as temperature T, pressure P, volume V, number of particles N, energy E, chemical potential μ, etc) results in different statistical average of output thermodynamic quantities. The usage of these constraints reduces the system's degree of freedom to the an expected number for possible computations and each state (with those constraints) is called an ensemble. Popular ensembles employed for molecular simulations (MD or MC) include NVE or microcanonical (constant number of particles, volume and energy), NPT or isobaric-isothermal (constant number of particles, pressure and temperature), μVT or grand-canonical (constant chemical potential, volume and temperature).

CHAPTER III

DENSITY-FUNCTIONAL THEORY STUDIES

A. Synopsis

Firstly, DFT calculations were performed to study the mechanical properties of Fe at different phases, including body-centered cubic, face-centered cubic and hexagonal closed-pack crystals. Elastic constants were extracted from the relationship between strain energy and strain tensors. Within a certain range around equilibrium states, elastic constants are linearly dependent of pressure. Later, we used this method to investigate the fundamental process and mechanism of EAC-related issues at the nanoscale level, with two case studies concerning the stress corrosion in iron and hydrogen embrittlement in palladium. When segregating to the grain boundary of iron, different impurity elements such as sulfur, phosphorus and nitrogen raise corrosion failures in a variety of ways. Hydrogen atoms, due to their mobility and small atomic size, are able to form high occupation at crystal defects but show different interactions to vacancy and GB.

B. DFT Calculations on Lattice Dynamics and High-Order Elastic Constants of Fe at Elevated Pressures*

1. Motivation

Understanding the mechanical properties of iron under high pressure and anisotropic loads is essential in order to interpret its behavior beyond elastic response regime.

---

*Reprinted with permission from "H. H. Pham and T. Cagin. Lattice dynamics and third order elastic constants of Fe from first principles. *CMC*, vol. 16, no. 2, pp. 175-194, Apr. 2010". Copyright © Tech Science Press 2010.

When dealing with the behavior of materials under infinitesimal strains, elasticity of materials is fundamental for any solid material. Broadly speaking, it is related to the internal energy and binding forces [89], as the elastic resistance of a substance emerges as response of materials to applied loads through repulsive and attractive forces between the atoms. Elastic coefficients may be important quantities to interpret the structural stability and phase transformations in materials [90]. In general, the second-order elastic constants (SOEC) describe the response of materials to the linear deformation, whereas the third- and higher-order elastic constants (TOEC and HOEC) correspond to non-linear elasticity [91]. Also, elasticity is essential in evaluating various mechanical and thermal properties, such as equation of state, pressure derivative of elastic constants [92], thermal expansion, phonon-phonon interaction [91], and acoustic amplification of microwave frequencies [93]. Particularly, studying the elasticity of hexagonal close-packed (hcp) iron is critical in explaining the elastic anisotropy, seismic behavior and differential rotation of the Earth's interior since it is the stable form at high pressures [94–96].

The measurement of elastic coefficients can be conducted by various experimental techniques. Ultrasonic measurements [97] or shock compression experiments [93] are used to obtain SOEC. TOEC can be experimentally measured through the determination of the change in the acoustic velocities under hydrostatic and uniaxial stresses [98, 99]. The forth-order elastic constants (FOEC) could also be determined by using shock-compression methods [93]. However, due to the difficulties in these works, the experimental measurements on TOEC or HOEC require that many of efforts be made [93, 100], especially for those under extreme conditions. Due to advances in computational techniques and computer resources, several theoretical approaches are nowavailable to calculate these quantities, including molecular dynamics [87, 92, 101, 102] and first-principle methods [103–108].

2. Theoretical and Computational Details

Now we describe a method for determining SOEC and TOEC from strain-energy and applied strain relationships. This relationship can be described in terms of the elasticity theory [109]. For a crystal domain, $\mathbf{X}= (\mathbf{I}+\epsilon)\mathbf{A}$ is the deformed lattice under the application of a strain matrix $\varepsilon$to the initial lattice vectors $\mathbf{A}$ **(**where $\mathbf{I}$ is the 3×3 unit matrix). The transformation from a certain point A(a_1, a_2, a_3) which is in the initial unstrained domain, into X(x_1, x_2, x_3), which is in the deformed domain, is characterized by a Jacobian matrix $\mathbf{J}$:

$$J_{ij} = \frac{\partial x_j}{\partial a_i} \tag{3.1}$$

The symmetric Lagrangian strain parameters ε_{ij} are then given as [110]:

$$\eta_{ij} = \frac{1}{2}\sum_{n=1}^{3}(\frac{\partial x_n^2}{\partial a_i \partial a_j} - \delta_{ij}) \quad or \quad \eta = \frac{1}{2}(J^T J - I) \tag{3.2}$$

where $\delta_{ij}$is the Kronecker delta. The densities in the initial undeformed and final deformed state, ($\rho_0$and ρ respectively), are related to each other through the determinant of the Jacobian (ρ_0= ρdet$\mathbf{J}$**),** then the strain matrix, ϵ yields a volume-conserving deformation [111] in the case of a unit-determinant $\mathbf{J}$. Since deformation tensors are symmetric, we use the Voigt index notation for convenience: (11)→1, (22)→2, (33)→3, (23)→4, (13)→5, (12)→6. Thus, a 3×3 symmetric strain matrix, ε

can then be simplified to a 6-dimensional vector η.

$$\varepsilon = \begin{pmatrix} \varepsilon_{11} & \varepsilon_{12} & \varepsilon_{13} \\ \varepsilon_{21} & \varepsilon_{22} & \varepsilon_{23} \\ \varepsilon_{31} & \varepsilon_{32} & \varepsilon_{33} \end{pmatrix} \quad and \quad \eta = \begin{pmatrix} \eta_1 \\ \eta_2 \\ \eta_3 \\ \eta_4 \\ \eta_5 \\ \eta_6 \end{pmatrix} = \begin{pmatrix} \varepsilon_{11} \\ \varepsilon_{22} \\ \varepsilon_{33} \\ \varepsilon_{23} + \varepsilon_{32} \\ \varepsilon_{13} + \varepsilon_{31} \\ \varepsilon_{12} + \varepsilon_{21} \end{pmatrix} = \begin{pmatrix} \varepsilon_{11} \\ \varepsilon_{22} \\ \varepsilon_{33} \\ 2\varepsilon_{23} \\ 2\varepsilon_{13} \\ 2\varepsilon_{12} \end{pmatrix} \tag{3.3}$$

Stress components $\sigma_{\alpha\beta}$ (α, β =1, 2, 3 in Cartesian coordinates) are defined as the force in α^{th} axis on the plane with outward normal in β^{th} direction. The generalized Hooke's law [112] gives the relation between the stress, elastic modulus and strain: $\sigma_{\alpha\beta} = \mathrm{C}_{\alpha\beta\mu\nu}\eta_{\mu\nu}$ or, $\sigma_I = \mathrm{C}_{IJ}\eta_J$ in Voigt notation.

In addition, the thermodynamic definition of adiabatic (constant S) and isothermal (constant T) n-order elastic constants given by Brugger [98, 110] are widely used:

$$C^S_{ijkl..mn} = \rho_0 (\frac{\partial^n U}{\partial\varepsilon_{ij}\partial\varepsilon_{kl}\cdots\partial\varepsilon_{mn}})_S \tag{3.4}$$

where U and F are internal energy and free energy, respectively and ρ_0 is the specific density of the unstrained medium.

In our work, total energy was calculated by DFT at 0K; therefore elastic constants can be referred to as isothermal. The tensor stress is described by following equation:

$$\sigma_{\alpha\beta} = \frac{\rho}{\rho_0} \sum_{m,n=1}^{3} \frac{\partial x_\alpha}{\partial a_m} \frac{\partial U}{\partial \varepsilon_{mn}} \frac{\partial x_\beta}{\partial a_n} \tag{3.5}$$

The elastic energy per crystal unit volume upon application of a Lagrangian strain tensor, η, may be expanded in terms of elastic constants as the expansion

coefficients [98]:

$$\rho_0 \Delta F(\eta) = \frac{1}{2!} \sum_{IJ=1\cdots6} C_{IJ}\eta_I\eta_J + \frac{1}{3!} \sum_{IJK=1\cdots6} C_{IJK}\eta_I\eta_J\eta_K + \Theta(\eta^4) \tag{3.6}$$

Due to high symmetry in the stress and strain tensors of a cubic crystal has, a fourth-rank SOEC tensor can be reduced to a 6x6 symmetric matrix with only 12 non-zero SOEC terms, and three of them are independent (C_{11},C_{12} and C_{44}):

$$\begin{aligned}
&\sum_{IJ=1\cdots6} C_{IJ}\eta_I\eta_J \\
= \;& (\eta_1,\eta_2,\eta_3,\eta_4,\eta_5,\eta_6).\begin{pmatrix} C_{11} & C_{12} & C_{12} & 0 & 0 & 0 \\ C_{12} & C_{11} & C_{12} & 0 & 0 & 0 \\ C_{12} & C_{12} & C_{11} & 0 & 0 & 0 \\ 0 & 0 & 0 & C_{44} & 0 & 0 \\ 0 & 0 & 0 & 0 & C_{44} & 0 \\ 0 & 0 & 0 & 0 & 0 & C_{44} \end{pmatrix}.\begin{pmatrix} \eta_1 \\ \eta_2 \\ \eta_3 \\ \eta_4 \\ \eta_5 \\ \eta_6 \end{pmatrix} \\
= \;& C_{11}(\eta_1^2+\eta_2^2+\eta_3^2) + 2C_{12}(\eta_1\eta_2+\eta_2\eta_3+\eta_3\eta_1) + C_{44}(\eta_4^2+\eta_5^2+\eta_6^2) \\
= \;& C_{11}(\varepsilon_{11}^2+\varepsilon_{22}^2+\varepsilon_{33}^2) + 2C_{12}(\varepsilon_{11}\varepsilon_{22}+\varepsilon_{22}\varepsilon_{33}+\varepsilon_{33}\varepsilon_{11}) + 4C_{44}(\varepsilon_{23}^2+\varepsilon_{13}^2+\varepsilon_{12}^2)
\end{aligned} \tag{3.7}$$

Under the uniaxial strain (i.e η_i=0 for i≠1), this expression will remain the only contribution from C_{11}. The biaxial strain (η_i=0 for i≠1,2) contribution is given in terms of C_{11} and C_{12}; likewise, a strain tensor with zero diagonal components leads to a contribution of C_{44} alone. Hence, choices of strain tensors will result in a system of linear equations on elastic constants as variables, which will give the value of each coefficient after solving equations.

The symmetry analysis leads to 6 distinct TOEC for cubic crystals [113]; therefore, the expansion of the third-order term in equation 3.6 yields the following com-

bination of cubic crystal TOEC:

$$\begin{aligned}
&\sum_{IJK=1\cdots6} C_{IJK}\eta_I\eta_J\eta_K \\
= \;& C_{111}(\eta_1^2+\eta_2^2+\eta_3^2)+3C_{112}(\eta_1^2\eta_2+\eta_2^2\eta_1+\eta_2^2\eta_3+\eta_3^2\eta_2+\eta_3^2\eta_1+\eta_1^2\eta_3) \\
& +6C_{123}\eta_1\eta_2\eta_3+3C_{144}(\eta_1\eta_4^2+\eta_2\eta_5^2+\eta_3\eta_6^2) \\
& +3C_{155}(\eta_2\eta_4^2+\eta_3\eta_4^2+\eta_1\eta_5^2+\eta_3\eta_5^2+\eta_1\eta_6^2+\eta_2\eta_6^2)+6C_{456}\eta_4\eta_5\eta_6
\end{aligned} \tag{3.8}$$

Low symmetrical crystals have more distinct elastic constants than high symmetrical crystals. Specifically, the hcp crystals have 5 independent SOEC, and the 2-order term in equation 3.6 can be given the following way:

$$\begin{aligned}
&\sum_{IJ=1\cdots6} C_{IJ}\eta_I\eta_J \\
= \;& (\eta_1,\eta_2,\eta_3,\eta_4,\eta_5,\eta_6,).\begin{pmatrix} C_{11} & C_{12} & C_{13} & 0 & 0 & 0 \\ C_{12} & C_{11} & C_{13} & 0 & 0 & 0 \\ C_{13} & C_{13} & C_{33} & 0 & 0 & 0 \\ 0 & 0 & 0 & C_{44} & 0 & 0 \\ 0 & 0 & 0 & 0 & C_{44} & 0 \\ 0 & 0 & 0 & 0 & 0 & (C_{11}-C_{12})/2 \end{pmatrix}.\begin{pmatrix} \eta_1 \\ \eta_2 \\ \eta_3 \\ \eta_4 \\ \eta_5 \\ \eta_6 \end{pmatrix} \\
= \;& C_{11}(\eta_1^2+\eta_2^2+\frac{1}{2}\eta_6^2)+C_{12}(2\eta_1\eta_2-\frac{1}{2}\eta_6^2)+2C_{13}(\eta_1\eta_3+\eta_2\eta_3)+C_{33}\eta_3^2+C_{44}(\eta_4^2+\eta_5^2)
\end{aligned} \tag{3.9}$$

For completeness, the expression below is derived for contribution to strain energy from TOEC in the hcp phase, using the symmetry table given by Fumi [113]:

$$\begin{aligned}
&\sum_{IJK=1\cdots6} C_{IJK}\eta_I\eta_J\eta_K \\
= \;& C_{111}(\eta_1^3+3\eta_1\eta_2^2-\frac{3}{2}\eta_1\eta_6^2+\frac{3}{2}\eta_2\eta_6^2)+C_{112}(3\eta_1^2\eta_2+3\eta_1\eta_2^2-\frac{3}{4}\eta_1\eta_6^2-\frac{3}{4}\eta_2\eta_6^2)
\end{aligned}$$

$$+C_{113}(3\eta_1^2\eta_3 + 3\eta_2^2\eta_3 + \frac{3}{2}\eta_3\eta_6^2) + C_{114}(3\eta_1^2\eta_4 + 3\eta_1\eta_5\eta_6 - 3\eta_2^2\eta_4 + 3\eta_2\eta_5\eta_6)$$
$$+C_{123}(6\eta_1\eta_2\eta_3 - \frac{3}{2}\eta_3\eta_6^2) + C_{124}(6\eta_1\eta_2\eta_4 + 9\eta_1\eta_5\eta_6 - 6\eta_2^2\eta_4 - 3\eta_2\eta_5\eta_6 + 3\eta_4\eta_6^2)$$
$$+C_{133}(3\eta_1\eta_3^2 + 3\eta_2\eta_3^2) + C_{134}(6\eta_1\eta_3\eta_4 - 6\eta_2\eta_3\eta_4 + 6\eta_3\eta_5\eta_6)$$
$$+C_{144}(3\eta_1\eta_4^2 + 3\eta_2\eta_5^2 - 3\eta_4\eta_5\eta_6) + C_{155}(3\eta_1\eta_5^2 + 3\eta_2\eta_4^2 + 3\eta_4\eta_5\eta_6)$$
$$+C_{222}(-3\eta_1\eta_2^2 + \frac{9}{4}\eta_1\eta_6^2 + \eta_2^3 - \frac{3}{4}\eta_2\eta_6^2) + C_{333}(\eta_3^3)$$
$$+C_{344}(3\eta_3\eta_4^2 + 3\eta_3\eta_5^2) + C_{444}(\eta_4^3 - 3\eta_4\eta_5^2) \tag{3.10}$$

Due to the sensitivity of elastic constants calculations, especially TOEC, to the maximum value of strains, the strains are applied within the range of -0.035 to +0.035.

We present associated first-principles calculations for SOEC and TOEC of iron using the Density Functional Theory [76], which is implemented in Vienna Ab initio Simulation Package (VASP) [114]. We use the Projector-Augmented Wave (PAW) methods [115] to simulate the magnetic and crystal properties of iron. The PBE Generalized Gradient Approximation (GGA) exchange-correlation [79] is employed. In the k-point sampling, we use the Monkhorst-Pack grid [116] for the plane wave basis. In case of a magnetic phase, the spin-polarized calculations are carried. The computational tests for sufficient k-mesh and cut-off energy are conducted until the free energy converged within 1 meV/atom.

3. Results and Discussions

a. Equations of State

Depending on the external conditions, iron is observed to have various phases, which includes body-centered cubic (bcc), face-centered cubic (fcc), and hexagonal close-packed (hcp) [117]. Crystal structure of ground-state iron is ferromagnetic bcc with 2 atoms contained in the conventional cubic unit cell. Upon increased pressure and

Table II. EOS parameters of bcc, fcc and hcp Fe

Fe polymorphs	Methods	Atomic volume, $Å^3$	B_0, GPa	dB_0/dP
BCC Fe	Theory, bcc Fe	11.44	177.9	5.09
	Expt., bcc Fe [118]	11.78	172	5.0
	Comp. ref., bcc Fe [121]	11.33	174	–
FCC Fe	Theory, fcc Fe	10.24	285.4	4.70
	Comp. ref., fcc Fe [121]	10.27	282	–
HCP Fe	Theory, hcp Fe	10.18	290.3	4.71
	Expt., hcp Fe [90]	11.2	208	–
	Comp. ref., hcp Fe [90]	10.26	288	–

temperature, iron undergoes phase transformations into close-packed structures: fcc and hcp. The hcp iron was reported to be the stable phase at the Earth's interior conditions [118, 119]. The transition of iron from bcc to hcp begins at 9-13 GPa [90], and the transformation to fcc occurs around 1150K [120].

The equilibrium state of iron is determined by studying the behavior of the energy and pressure, i.e., the EoS for bcc, fcc, and hcp Fe at 0K. The atomic energy curves are shown for different structures in Fig. 6a, in which bcc Fe is considered to be ferromagnetic, and fcc and hcp are both non-magnetic phases. In fact, magnetic versions of fcc and hcp were also simulated but yielded no difference in total energy, which in turn confirms that no contribution from magnetization is expected in fcc and hcp Fe. From the plot, the bcc crystal appears to be more stable at 0K condition and has a smaller atomic packing factor (APF). This observation is consistent with theoretical calculations, in which bcc has an APF of 0.64 vs. 0.74 of fcc and hcp. If far from the zero pressure, the hcp phase could be more favorable than the bcc. The calculation shows that the critical point is determined to be around 70 GPa (Fig. 6b). This work is more focused to on bcc and hcp calculations because they are naturally observed crystalline phases of Fe.

Based on the plots, the equilibrium lattice parameter can be determined as the

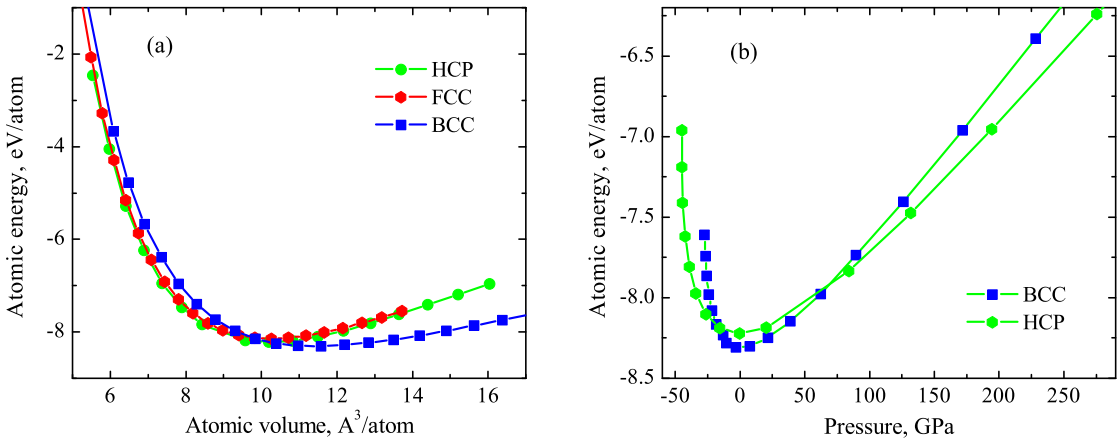

Fig. 6. Equation of states for Fe in bcc, fcc and hcp phases. (a): Variation of atomic energy as a function of atomic volume. (b): Variation of atomic energy as a function of external pressure

point of minimum energy and hence the zero pressure. The visual inspection gives a value approximately at two-thirds the distance between 2.80 and 2.85 for bcc iron. However, the zero-pressure lattice parameter, bulk modulus and its pressure derivative were also obtained by fitting the data to an EoS expression for metals. The E-V and P-V relations introduced by Li, et al. [122] was used, which was a modified version of the Vinet and Rose equation [123].

The EoS results show a good agreement with the experimental and previous theoretical calculations (Table II). The theoretical lattice parameter calculated using DFT seems to be slightly below that of measurements. In addition, the theoretical calculations of the hcp bulk modulus, as well as the report by Lew et al. [90] yields a value 40% different from the experimental value (290 GPa compared to 208 GPa). The difference may result from the fact that in nature hcp phase exists in extreme conditions, while this DFT calculation performed with the 0K and 0 GPa. Also, the experimental evaluations of bulk modulus at high pressures generally come with large fluctuation error in measurements.

Table III. Calculated elastic constant of fcc Fe at zero pressure, GPa

C_{11}	C_{12}	C_{44}	C_{111}	C_{112}	C_{123}	C_{144}	C_{166}	C_{456}
418.85	217.56	238.63	-4345.45	-926.34	-553.66	-297.33	-1077.43	-93.7

b. Elastic Constants: Second and Third Order

Calculations were made of SOEC and TOEC of bcc (Fig. 7) and hcp Fe (Fig. 8, 9) at various points around zero pressure by fitting the strain energy to equations 3.6 - 3.10. Also, a set of elastic constants was reported for fcc phase at zero pressure in Table III. Using the relationship of $B_0=(C_{11}+C_{12})/3$ for cubic crystals, the bulk modulus, B_0, can be obtained from the values of C_{11} and C_{12}, in addition to the value derived from the EoS fit. From those two methods, the data still gave close agreements for bcc Fe (188.4 vs. 177.9 GPa) and fcc Fe (284.7 vs. 285.4 GPa). In addition, both bcc and fcc phases obey the lattice stability criteria for cubic crystals [124], i.e., $B_0>0$, $G=C_{44}>0$, $C_s=(C_{11}-C_{12})/2>0$, and both comply with the general rule: $B_0 > G > C_s$.

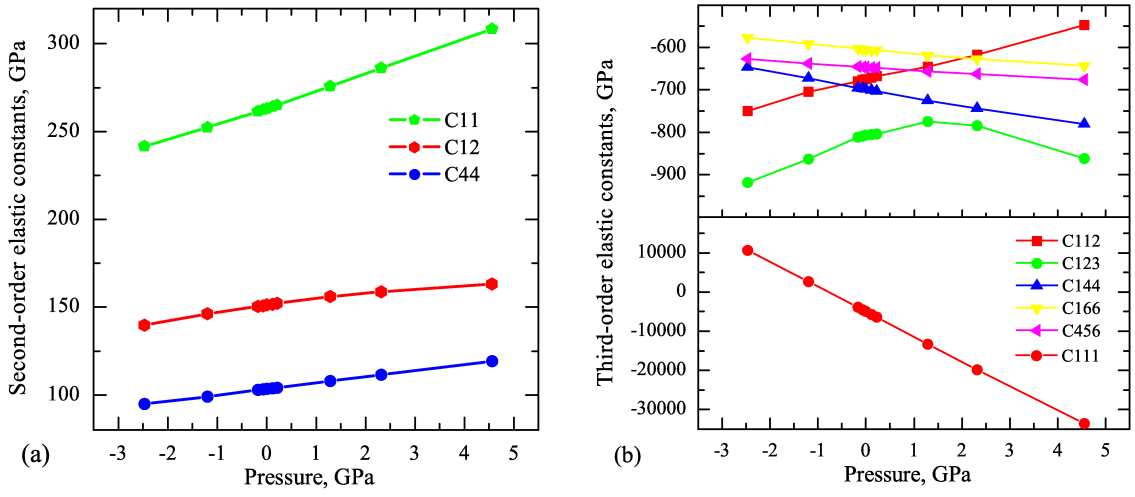

Fig. 7. Variation of SOEC (a) and TOEC (b) of bcc Fe as a function of pressure

According to these calculations, most of the elastic constants (second and third-

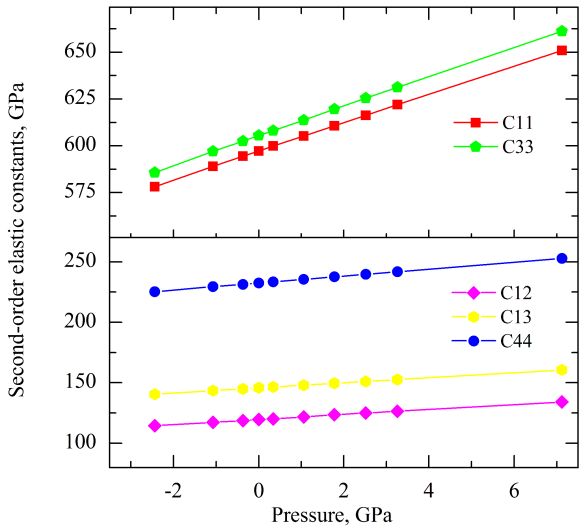

Fig. 8. Variation of hcp Fe SOEC as functions of pressure

order) follow a linear dependence with respect to pressure. The values of TOEC and especially C_{111} are very sensitive to pressure. For example, a 0.1 GPa variation of external pressure may cause a change in C_{111} by 600 GPa in bcc Fe.

The SOEC of bcc and hcp Fe positively vary with pressure, and this is a normal behavior for solids. The derivatives of SOEC can either be determined either directly from the slope of the line or be calculated analytically, requiring the knowledge of some TOEC.

$$\frac{\partial C_{11}}{\partial P} = -\frac{2C_{11}+2C_{12}+C_{111}+2C_{112}}{C_{11}+2C_{12}} \tag{3.11}$$

$$\frac{\partial C_{12}}{\partial P} = -\frac{-C_{11}-C_{12}+2C_{112}+C_{123}}{C_{11}+2C_{12}} \tag{3.12}$$

$$\frac{\partial C_{44}}{\partial P} = -\frac{C_{11}+2C_{12}+C_{44}+C_{144}+2C_{166}}{C_{11}+2C_{12}} \tag{3.13}$$

The results dC_{11}/dP, dC_{12}/dP, and dB/dP are very consistent in two ways, while there is an observable difference in dC_{44}/dP (Table IV). The negative TOEC values of bcc and fcc Fe indicate that the increasing pressure will cause an increase in vibration

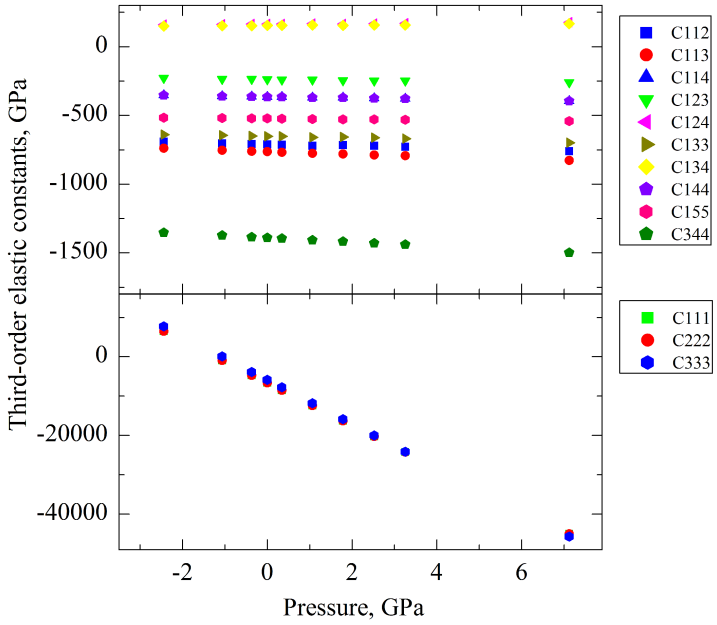

Fig. 9. Variation of hcp Fe TOEC as functions of pressure

Table IV. Calculated first pressure derivative of SOEC for bcc Fe

	dC_{11}/dP	dC_{12}/dP	dC_{44}/dP	dB/dP
From values of TOEC	9.72	4.55	2.20	6.27
From plot of SOEC	9.70	4.35	3.57	6.13
From EOS	–	–	–	5.09
Expt.[118]	–	–	–	5.0

frequencies. The behavior of bcc Fe under compression can be verified by studying the phonon dispersion curves in the next section.

c. Phonon Dispersion of Iron Polymorphs and Pressure Dependence

The calculated phonon dispersion curves of bcc, fcc, and hcp Fe are displayed in Fig. 10, in addition to the corresponding density of states (DOS) along the high symmetry lines of the Brillouin zone (BZ). Consistency is observed between the experimental and our theoretical calculations and experimental data [125], which were

collected at room temperature and 0 GPa.

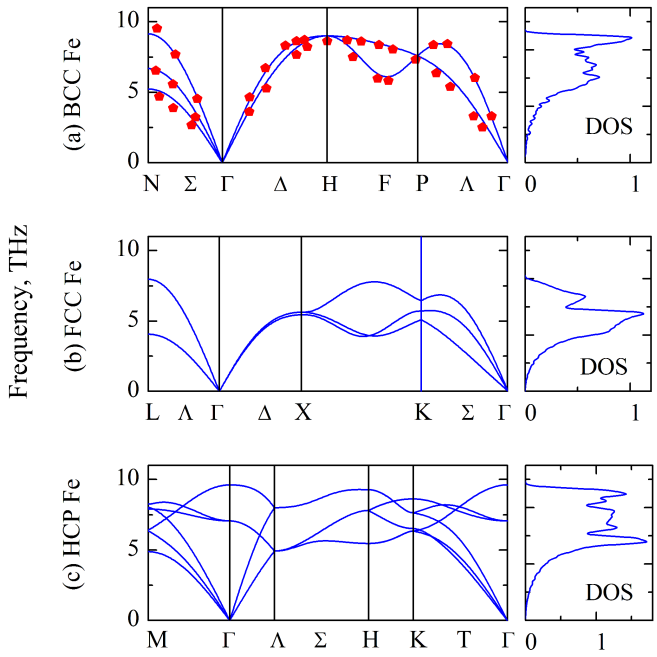

Fig. 10. Phonon dispersion curves of bcc, fcc and hcp Fe at equilibrium. The dots in bcc phonon are experimental data

In order to assess the stability of Fe crystal at high pressures, the phonon spectra of bcc Fe is calculated under various compressions, displayed in Fig. 11a. Besides the expansion of the frequency range, negative frequency values were found for the optical branch after 200 GPa. This negative vibration frequency indicates the instability in bcc Fe structure at high pressures. Similarly, the hcp Fe is studied under "negative" pressures by expanding the unit cell volume beyond zero pressure volume (Fig. 11b). After approximately a pressure value of -40 GPa an imaginary frequency for an acoustic branch is observed, i.e. indication of an unstable hcp. This observation suggests that bcc Fe is more favorable at equilibrium, whereas hcp is dominant at extreme conditions.

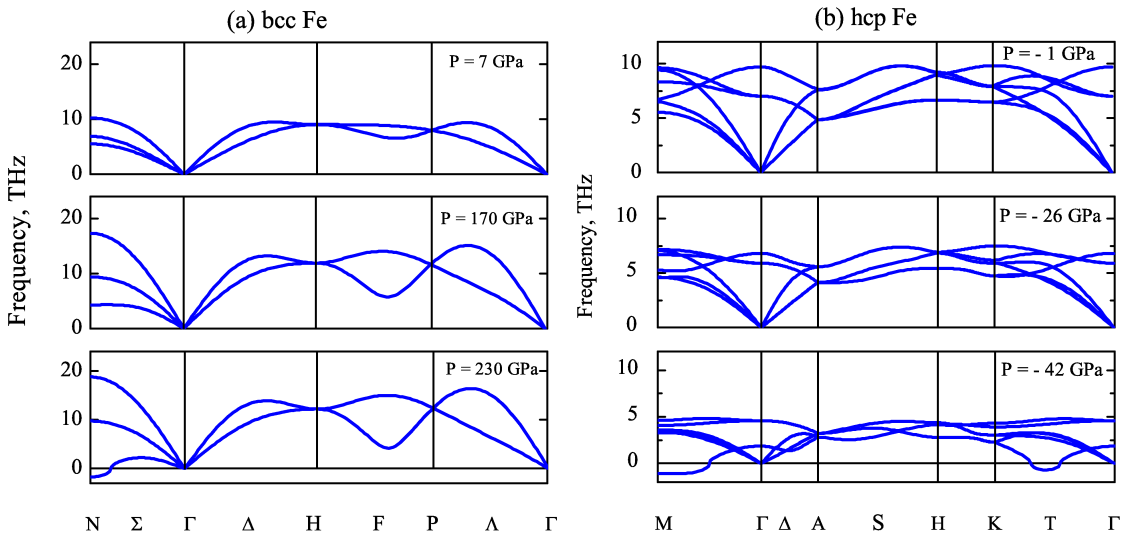

Fig. 11. Phonon spectra of bcc Fe at increasing pressure (a) and hcp Fe at decreasing pressure (b)

4. Concluding Remarks

For conclusion, a complete set of SOEC and TOEC has been reported in three common phases of Fe: bcc, fcc and hcp. The calculations of their values at different pressures show a fairly linear dependence. Among the TOEC, C_{111} is most affected by the external stress. The study on phonon spectra confirms the instability of lattice vibration for bcc at high pressure and for hcp under tension.

C. Stress-Corrosion Cracking in Fe and the Mechanisms[†]

1. Motivation

Since Fe and its alloys are among the most widely used materials, the problem of SCC in Fe needs to be completely understood in order to minimize the possibility of failures, as well as to help with the manufacturing of high corrosion-resistant steels. SCC is closely related to the segregation of impurities to GBs, which are the planar discontinuity where two single crystals meet and they can serve as ideal channels for the migration of atoms. Additionally, these boundaries have low coordination and are prone to mechanical damage as they are more brittle, compared to the perfect crystal. The presence of impurity elements may modify the GB energy and local crystal structure, including substantial changes in interatomic distances. Even when the cracks are initiated at GBs, the symptoms of the risk (of failure) may not be apparent from the exterior of metal or metal-alloy components of the structures, hence the SCC remains latent and gives no signs of warning [4].

Due to its intricate nature, conducting experiments on this phenomenon faces many difficulties and requires a lot of effort. The question regarding how the accumulation of these corrosive elements induces the crack initiation has not yet been reported. Therefore, this work will present an analysis on the behavior of $\Sigma 3$ (111) Fe grain boundary under segregation of various impurity atoms (S, P, N, C, and B) and will explain various SCC mechanisms of each element.

[†]Reprinted with permission from "H. H. Pham and T. Cagin. Fundamental study on stress-corrosion cracking in iron and underlying mechanisms. *Acta Materialia*, vol. 58, no. 15, pp. 5142-5149, Sep. 2010". Copyright © 2010 Acta Materialia Inc.

2. Computational Details

The Density Functional Theory (DFT) [76], as implemented in Vienna Ab-initio Simulation Package (VASP) [114], was employed to perform the first-principles calculations. The magnetic and crystal properties of iron were described by the electron Projector-Augmented Wave (PAW) methods [115] with the PBE Generalized Gradient Approximation (GGA) exchange-correlation [79]. In the k-space sampling, we have used a 4x3x1 Monkhorst-Pack grid [116] for the plane wave basis in all model systems.

In this work, a model system of 96 atoms with three-dimensional periodic boundary conditions was constructed to mimic a clean $\Sigma 3$ (111) grain boundary in body-centered cubic (BCC) Fe. This GB (with the misorientation of 70.53° between two grains) belongs to the family of high-angle grain boundaries (HAGBs), which is differentiated from low-angle grain boundaries (LAGBs) by higher degree of grain disorder and considerable open space. HAGBs, therefore, offer more free volume for impurity segregations and may be more vulnerable to impurity-induced embrittlement as a consequence. Also, our choice of $\Sigma 3$ (111) GB follows a conventional model as introduced in previous works [68, 126].

By investigating the geometry of the grain boundary, the hollow sites were located on GB (Fig. 12). There are four such hollow sites on GB plane in a 96-atom model cell. These sites are the most likely ones to host impurity atoms (S, P, N, C, B), which can easily fit into these vacancy sites. Since there are no any hollow sites on other layers when moved into crystals away from the GB plane, in the context of this paper, we always refer to substitutions of host Fe, when dealing with the precipitations of impurity atoms to those layers. To differentiate between possible binding locations for impurity elements, the interstitial sites on GB are denoted as

GB0, and the substitution sites (or layers) as GB1, GB2, GB3 and etc, depending on how far they are located from the GB plane, and the layers with opposite indices are equivalent due to the model used represents a twin (Fig. 12). There are a total of 24 such layers with four atom sites per layer in the GB model cell. In calculating the total energy, the equilibrium grain boundary cell is obtained by relaxing the positions of atoms and changing the lattice vectors until stresses in x, y and z directions are well below one kbar. It is worth mentioning that this work models the BCC Fe in ferromagnetic state.

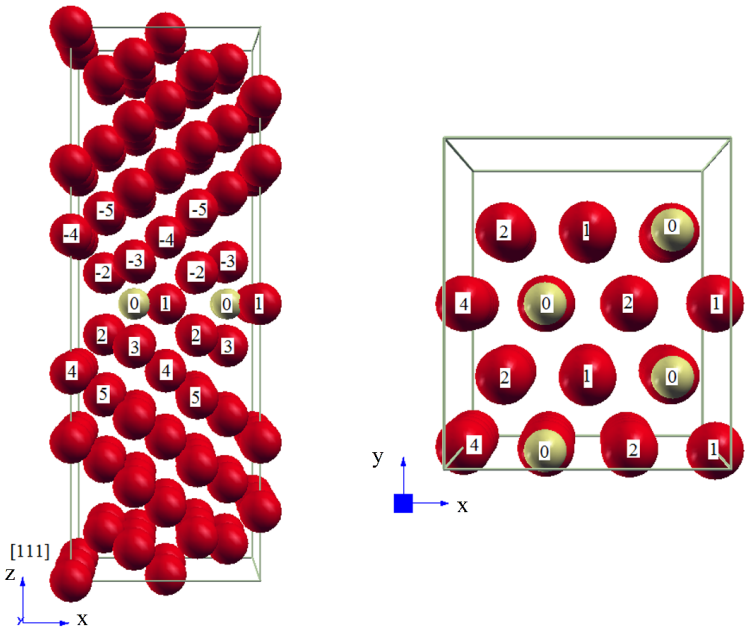

Fig. 12. The model system with 96 Fe-atoms containing a Σ3 (111) grain boundary. Red spheres indicate the Fe and yellow ones represent S at the hollow sites of GB0 layer

The precipitation of impurity atoms ensues from the migration through grain boundaries, as well as the generation of vacancies. To demonstrate the tendency for an atom to be bound to the GB, the concept of binding energy with respect to its

atomic gas state, -E_b, is used, which is calculated by the following equation [68]:

$$nE_b = E_{tot}^{GB}(Fe_mI_n) - nE_I - E_{tot}^{GB}(Fe_{m0}) - \frac{m - m_0}{m_0}E_{tot}^{bulk}(Fe_{m0}) \tag{3.14}$$

where $E_{tot}^{GB}(Fe_mI_n)$describes total energy of the GB unit cell containing m iron atoms and n impurities. $E_{tot}^{GB}(Fe_{m0}$ and $E_{tot}^{bulk}(Fe_{m0})$ indicate the total energy of an impurity-free GB system and a BCC cell, respectively, which contains m_0 iron atoms. E_I, the total energy of one isolated impurity atom, is calculated by placing that atom in a large super-cell (15×15×15 Å) with spin polarization.

3. Results and Discussions

a. Influence of Sulfur Segregation to GB Behavior

The crystal structure is characterized by the nature of atoms and atomic bonds, which determine the minimum energy configuration. Because of the misfit, GBs have higher energy than that of the perfect crystal. In addition, the GB's energy may be modified in the presences of other species of atoms such as phosphorus, sulfur, or nitrogen. Therefore, during heat treatment or exposition of materials to the external environment [5], the minimization of the interfacial free energy is considered to be the driving force for those impurities to concentrate at the surfaces, interfaces, or GBs. The modification of GB nano-chemistry in metal and alloys, induced by the segregation of impurities, has a significant effect in altering the properties of material, including mechanical, chemical, electrical, and magnetic. Although certain elements may promote segregation or help with co-segregation, the context of this work solely focuses on the influences of each individual type of atom.

The model GB cell was first optimized using ionic relaxation before the impurities are inserted or substituted. To understand the mechanism of impurity segregation,

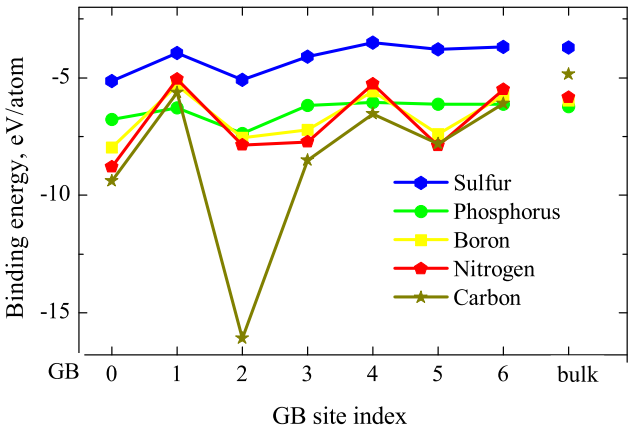

Fig. 13. The behavior of binding energy per impurity atom at different layers. GB0 and GB2 are more stabilized locations for impurity occupations

equation 3.14 is used to assess the binding strength of S, P, N, C and B to the vicinity of Fe grain boundary based on the calculated binding energy. First, each impurity atom is placed or substituted one after the other to different layers, from GB0, GB1 to GB6. Fig. 13 shows the variation of binding energy for different individual solute introduced to each of these GB layers, compared with the binding energy of that solute inside the bulk. Among these layers, GB0 and GB2 always result in providing energetically more favorable sites for solute segregation, (indicated by local minimums of the curve at these layers). Yamaguchi et al. has also reached the same conclusion on Fe-S system in their work [69], which shows that segregation of impurity atoms near GB are energetically more propitious than within the bulk. The graph reveals a steady binding of C to Fe grain boundary (GB2) than four other elements. The curves of S and P cases are more flat, compared to B, N, and C; however the variations are still large enough to make a difference (for example, the deflections of binding energy for S at GB0 and GB2 from that at GB1, respectively, are 1.2 and 1.14 eV/atom). For elements such as boron and nitrogen, GB3 and GB5 also appear to be favorable segregation sites, in addition to GB0 and GB2. However, to ensure consistency when

comparing the relative influence of different elements, we assume that GB2 and GB-2 will become the next occupied locations after GB0 vacancy sites have been filled. For boron and nitrogen, GB2 and GB-2 are closer to the boundary and have more probability to host the precipitates, even with the same affinity in comparison to GB3 and GB5. Specifically, the first four impurity elements will be inserted to GB0, followed by four substitutions at GB2, and the last four atoms will be placed at GB-2. Therefore, there will be an addition of up to 12 impurity atoms to the model cell.

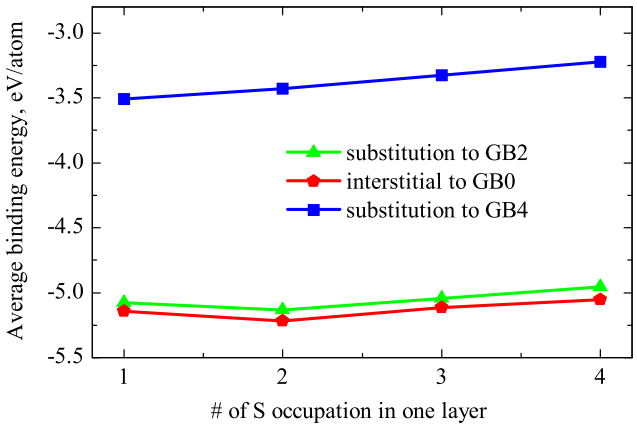

Fig. 14. Average binding energy of S as a function of layer occupations

This section will discuss the influence of S to the Fe grain boundary in detail. To understand the interaction between the neighboring sulfur atoms on the same layer, the average binding energy for sulfur was studied with respect to its occupation number, separately at GB0, GB2 and GB4 levels (Fig. 14). The average binding energy of one sulfur atom is shown to have changed only slightly with the concentration increase on the same layer (i.e., from 5.08 eV/S with one sulfur to 4.95 eV/S for four sulfur atoms substituted at GB2). This suggests that, the precipitation of the next sulfur to the same layer would be lightly affected by the presence of neighboring sulfur substitutes. The explanation may be due to the fact that the atomic distance on the

same layer is rather high (at the order of 4Å), and this is out of the strong interaction range. This plot also indicates that the tendency to attach to the last available site on GB2 or GB0 is still more probable than the first one on the other layer, eg., GB4.

Table V. Behavior of GB cell under S attachment. a, b, c - size of GB cell in x, y, and z dimensions, respectively. d - distance between GB2 & GB-2 layers

Layer occupied	# of occ.	a, Å	b, Å	c, Å	d, Å	Eb/S, eV
Clean cell	0	6.92	7.99	20.29	2.19	–
GB0	1	6.92	8.00	20.47	2.29	-5.14
GB0	2	6.92	8.03	20.60	2.39	-5.22
GB0	3	6.96	8.00	20.75	2.44	-5.11
GB0	4	6.96	8.02	20.84	2.52	-5.06
GB0, GB2	4+4	6.89	7.96	22.12	3.99	-4.86
GB0, GB2 & GB-2	4+4+4	6.94	8.02	22.12	4.49	-4.46

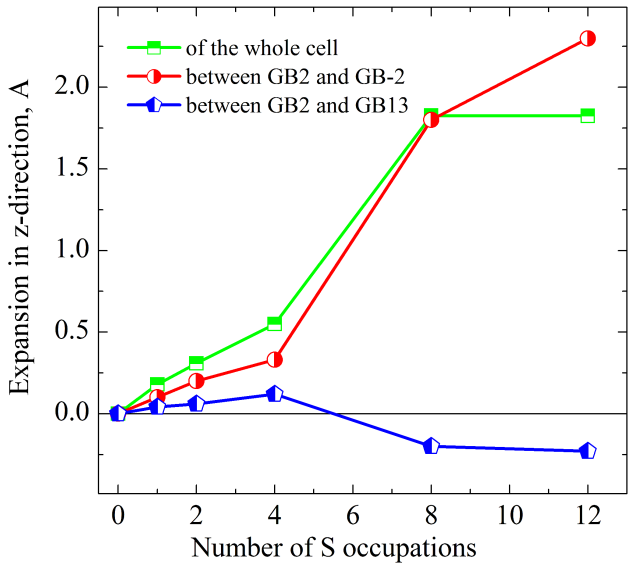

Fig. 15. Expansion of GB in z-dimension due to the S attachment

To investigate the effect of S to Fe grain boundary structure and stress state, computations were performed with model systems containing 12 sulfur atoms or less. The S arrangements create a substantial stretch in the z-direction (normal-to-grain-

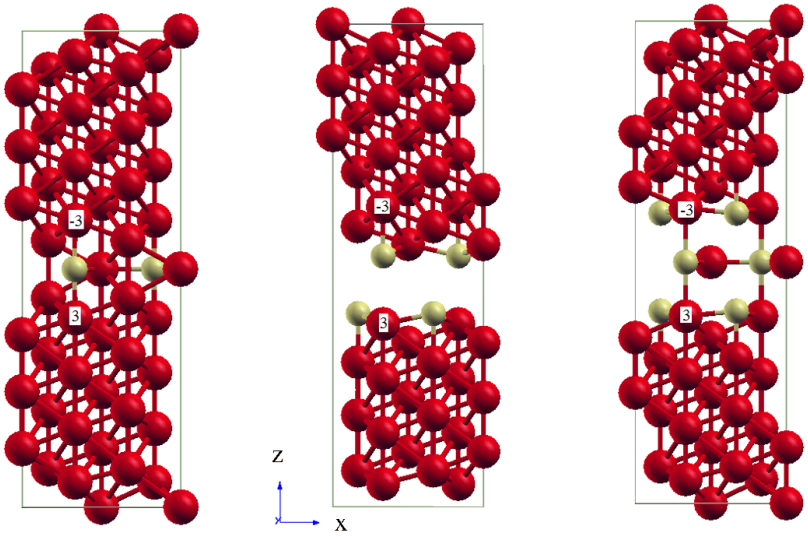

Fig. 16. Separation of Fe Σ3 (111) GB due to the precipitation of Sulfur (with 4, 8 and 12 sulfur atoms at GB). Red balls indicate the Fe and yellow balls represent S

boundary plane); however the impurities all have a small effect on the cell in x- and y-directions – parallel to GB plane (Table V). To understand the nature of this expansion in the z-direction, the distance between layers GB2 and GB-2 was measured, which covered the broadening around GB. Fig. 15 indicated that the expansion of the cell is inherently due to the expansion of grain boundary, and there is little relaxation between the layers GB2 through GB13 (and GB-2 through GB-13). This separation of grain boundary can be explained by the fact that sulfur atoms exert a repulsive force to each other and prefer to form sulfides by bonding with Fe atoms rather than to bond with other sulfur atoms. Also, atomic detail views of GB cells are presented in Fig. 16 with 4, 8 and 12 sulfur atoms precipitated at GB models, respectively. For 12 sulfurs, the gap (between GB3 and GB-3) is exactly the width of grain boundary.

b. Segregation Effects of Other Impurity Elements: P, N, C and B

In addition to influence of S, the respective effects of P, N, C and B atoms on Fe Σ3 (111) GB as a function of concentration for each impurity element was also studied. Table VI summarizes the influence of P, N, C and B to the GB cell under their segregation. Similar to the case of sulfur, all of the impurities have caused more or less separations around the grain boundary of Fe, but have little effect on the cell size in x and y dimensions. Again, the investigation on GB showed that its expansion is always larger than the overall stretch of the simulation cell. In other words, the expansion of the model cell in z-direction is mainly due to the expansion at the GB, and there is no significant influence of impurity atoms to other domains within the bulk grains.

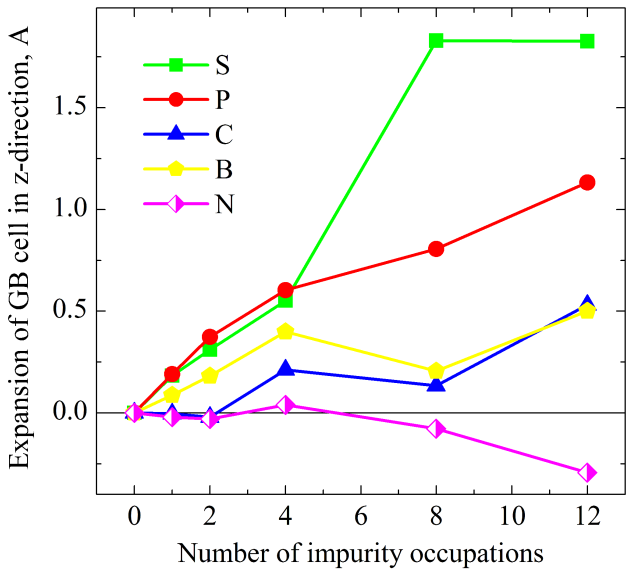

Fig. 17. Comparative separation of Fe Σ3 (111) GB under the attack of different impurity atoms (S, P, N, C, B). S and P render more GB detach when their concentrations are high

The behavior of Fe GB with increasing concentration of impurity atoms are plotted in Fig. 17, where S and P causes the appreciable extension of GB cell in

z-direction and is significantly more than C, B and N cases. When the concentration of impurity atoms is low, where one or two atoms are added to GB0, the separation effects are small and comparable for different kinds of impurity elements. Since the first four impurity atoms, in this simulation, are always added to GB0 as interstitial, various solutes will be able to create stress in the direction normal to the grain boundary plane, thus giving rise to an extension that is a more or less between two grain domains. In order to understand the mechanism of how these impurity particles can change the appearance of GB, the structure of the GB models under the C, B, P, and N attachments are displayed in Fig. 18.

Table VI. Behavior of GB cell under P, N, C and B attachment

Elements	# of occ.	Δa, Å	Δb, Å	Δc, Å	Δd, Å	Eb/S, eV
P	1	0.00	0.00	0.19	0.1	-6.78
	2	0.00	0.00	0.37	0.15	-7.46
	4	0.01	0.02	0.60	0.29	-7.41
	8	-0.04	-0.06	0.80	0.46	-6.22
	12	0.10	-0.14	1.13	1.44	-5.91
N	1	0.03	-0.01	-0.02	0.18	-8.80
	2	0.02	0.05	-0.03	0.04	-8.95
	4	0.09	-0.01	0.04	0.11	-7.92
	8	0.16	-0.10	-0.08	0.49	-8.15
	12	0.22	-0.21	-0.30	0.7	-7.74
C	1	0.02	0.00	-0.01	0.02	-9.38
	2	0.02	0.04	-0.02	0.04	-9.40
	4	-0.02	-0.01	0.21	0.11	-8.85
	8	-0.05	-0.05	0.13	-0.27	-7.92
	12	-0.19	-0.23	0.53	1.28	-7.42
B	1	-0.01	-0.01	0.08	0.04	-7.98
	2	-0.01	-0.02	0.18	0.05	-7.96
	4	-0.04	-0.04	0.40	0.13	-7.94
	8	-0.07	-0.10	0.20	0.05	-6.98
	12	-0.16	-0.18	0.50	1.07	-6.39

Large partitions of grain boundary, which are induced from high sulfur and phosphorus concentrations, imply their strong corrosive effects. The impact becomes more

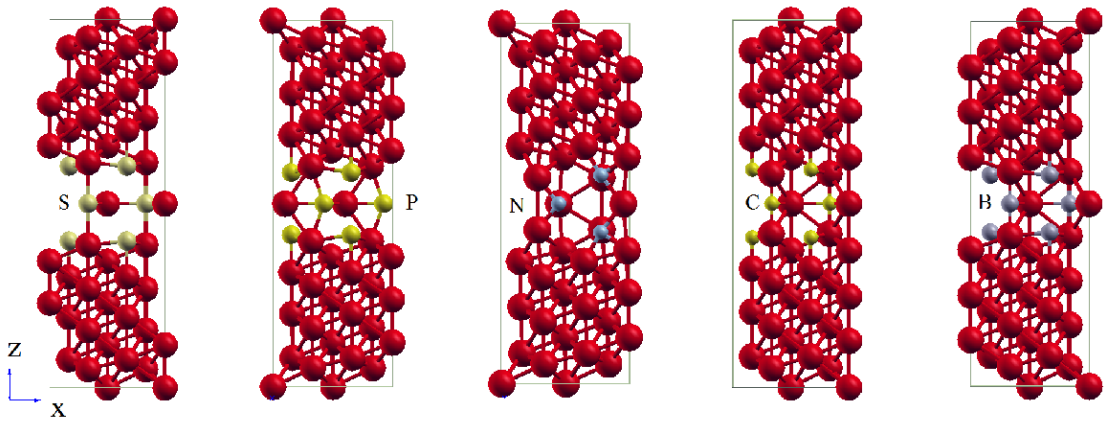

Fig. 18. Behavior of Fe Σ 3 (111) GB due to the precipitations of S, P, N, C and B, in which S and P result in greater separations at GB than C and B. N segregation causes the formation of voids

intense as the concentrations of S or P increases. Fig. 17 infers that the corrosive influence of P is less than that of S, as the intergranular separation caused by P is more moderate. Also, after P atoms filled four-twelfths of the available sites around grain boundary, the GB expansion becomes similar for further P segregation. Again, the GB extensions are due to the repulsion between P atoms, as the fact that P atoms favor phosphide formation when they are enclosed by Fe atoms. These GB extensions may lead to the initiation and growth of intergranular cracks, under sufficient impulses of external stress.

However, when more impurities are substituted at GB2 and GB-2, for B and C, two grain sides tend to pull back together, which indicates no corrosive effect is expected from B and C in contrast to S and P. In fact, it was reported that boron can be used as an additive to increase the hardening of ferrite steels [5]. Also, the implicit benefit of C or B precipitations may come from their site competition to constrain the segregation of S, P, or any other corrosive elements, to a boundary [5, 28]. Boron and carbon, therefore, show no corrosive effect on Fe. Nitrogen does not enhance GB

Table VII. Free volume of GB cell after occupation of 12 impurity elements

Structure	Total volume, Å^3/cell	Free volume, Å^3/cell	% free
Perfect BCC	1122.66	229.77	20.47
Clean GB	1122.66	263.59	23.48
GB + 12S	1231.19	296.65	24.09
GB + 12P	1181.85	247.56	20.95
GB + 12N	1111.12	177.25	15.95
GB + 12C	1127.19	55.3	4.91
GB + 12B	1098.36	69.41	6.32

separation either. Fig. 18 shows that once the nitrogen atoms are bound to the Fe GB, the formation of nitrides results in the emergence of voids. This phenomenon assists the rearrangement of the grain boundary atoms. Table VII provides an analysis on free volume calculation of the GB cell after occupations of 12 S, P, N, C, and B atoms. Due to its vacancy space, GB cell has more free volume than the perfect crystal with the same atom number. Large available volumes, observed in the cases of S and P segregation, are contributed from free spaces between two detached grains. The N precipitations, however, do not cause a GB separation, but a significant free volume is still available that is contributed by multiple void spaces.

The unique reconstruction behavior of GB was tested under the segregation of each solute species. In the final relaxed Fe-S GB cell, S is replaced by N and the structure is re-optimized. The computational optimization then leads to the rearrangement of atomic geometry, and its final configuration is the same as the one obtained earlier for Fe-N. Then, when N is replaced back by S, the system returns to the Fe-S GB structure as obtained in Fig. 18.

4. Concluding Remarks

The same binding tendency of different kinds of solutes to specific locations of the grain boundary could be explained from geometric aspects, other than the chemistry of impurity atoms. Specifically, besides vacancy sites on GB0, for Σ3 (111) Fe GB, there is a fair inclination for the impurity particles to precipitate at GB2 and GB-2.

The investigation of grain boundary structures after the possible maximum numbers of impurity atoms are inserted or substituted at the vicinity of grain boundary reveals that impurity particles on the same layer show little interaction with each other. However, impurity atoms in different layers exert repulsion to the particles of the same kind. In the case of S and P, this repulsive force is especially high, and it causes the GB grain boundary to expand enough for an intergranular crack to initiate and grow.

The stress corrosion effect may have various mechanisms. Typical examples of corrosive elements studied in this paper include sulfur and phosphorus. Carbon and boron have a little effect towards the strength of Fe grain boundary, whereas nitrogen acts in another mechanism. Nitrogen does not cause any extension around grain boundary; however, its presence at a high concentration leads to the growth of cavities and voids. The interesting question of how this structure rearrangement caused by N influences the material strength needs further investigation to elucidate whether these cavities at the GB weaken the material, and to which extent their interlinking may raise the failures.

D. Hydrogen Embrittlement in Palladium Crystal

1. Motivation

Hydrogen-palladium system was of great interest due to its exceptional properties. A unique solubility of hydrogen by palladium was first reported as early as mid-nineteenth century [127, 128]. High activity of hydrogen in palladium found practical applications in a wide range of area, not limited to catalysis [129–132], composite membranes [133–136], nanosensors [137–139], hydrogen storage and fuel cells [140, 141]. Also, hydrogen has been a great candidate for the future's eco-friendly and renewable energy resources.

However, hydrogen content in crystalline materials generally degrades their mechanical properties and performance. In fact, hydrogen-related failures have become increasingly critical issues in various industries, showing great impact on economy, safety and environment [142, 143].

Defects such as vacancy, dislocations and grain boundary can attract high localization of hydrogen, and as a result, the interactions of H with these defects considerably affect mechanical behavior of the materials. Therefore, the issues of saturated local H concentration at these locations are of significant important in order to interpret hydrogen embrittlemnt problem. It was suggested that the coalescence of vacancies in the presence of H will provide source for microcrack initiation and subsequent embrittlement [144]. Numerous experiments have evidenced that high H absorption can introduce the formation of superabundant vacancies in metals [145–147]. Grain boundaries, on the other hand, can serve as transport channels of impurity atoms. It was suggested by experiments that hydrogen causes embrittlement by decreasing the cohesive strength of GB, since H acts electron-receptor and weaken the bonding of host atoms across GB [148, 149].

Due to their intricate nature, real-time measurements and observations on these defect problems faces many challenges and requires much effort [150]. However, advances in computer resources and theoretical techniques have made the simulation work on the electronic structure and geometry of crystal defects more affordable. First-principles calculations have succeeded in describing structural properties of metals and alloys at electronic level, particularly for these issues of impurity and defect behaviors [56, 63, 64, 68, 70, 151].

In this work, we examine the interactions of H with defects (vacancy and grain boundary) in Pd system as a case study. The segregation of H at palladium grain boundary and vacancy with critical concentration was investigated in order to understand the behavior of high H occupation and the possible embrittlement mechanisms introduced by H.

2. Computational Details

The Density Functional Theory (DFT) [76], as implemented in Vienna Ab-initio Simulation Package (VASP) [114], was employed to perform the first-principles calculations. In this work, the crystal properties of Pd were described by the electron Projector-Augmented Wave (PAW) methods [115] with the PBE Generalized Gradient Approximation (GGA) exchange-correlation [79], unless noted otherwise. Bulk Pd crystal was simulated using a supercell of 108 face-centered cubic (FCC) atoms; in which the convergence of total energy is 0.1 meV per atom. Additionally, a bicrystal model of 80 atomic sites was constructed to simulate a symmetric tilt $\Sigma5/(210)/\langle100\rangle$ grain boundary in Pd. In the k-space sampling, we have used a Monkhorst-Pack grid [116] of $4\times4\times4$ for the single-crystal and $4\times4\times2$ for bicrystal supercells, for the plane wave basis, respectively. In calculating the total energy, equilibrated structures are obtained by relaxing the atomic positions and the lattice vectors until stress com-

ponents σ_{xx}, σ_{yy} and σ_{zz} are all well below 1.0 kbar. Periodic boundary conditions are always imposed in three dimensions.

The precipitation of impurity atoms ensues from the migration through grain boundaries, as well as the generation of vacancies. To demonstrate the binding tendency between hydrogen impurity and palladium host atoms, the concept of absorption energy is used; its average value, $E_{abs}{}^{avg}$, from absorption of n hydrogen atoms, is calculated by the following equation [68, 152]:

$$nE_{abs}^{avg}[nH] = E_{tot}^{nH} - E_{tot}^{0H} - \frac{n}{2}E^{H_2} \tag{3.15}$$

where $E_{tot}{}^{nH}$ and $E_{tot}{}^{0H}$ describe total energy of systems with n hydrogen segregation and at clean state, respectively. E^{H_2} is the total energy of one isolated hydrogen molecule, calculated by placing that molecule in a large supercell (20×20×20 Å).

The formation energy of one vacancy in any system is obtained from the change in total energies of that system before (E_{tot}) and after the formation of vacancy ($E_{tot}{}^{v}$), adding the average energy of one Pd atom in bulk state ($E_{bulk}{}^{Pd}$)

$$E_f = E_{tot}^{v} - E_{tot} + E_{bulk}^{Pd} \tag{3.16}$$

In order to illustrate the site competition between H segregation in vacancy (or grain boundary) with H binding in interstitial, we calculate the trapping energy of H. Its average value therefore is calculated with respect to the change in total energy of bulk palladium $E_{tot}{}^{1H}$-$E_{tot}{}^{0H}$, by adding one H as interstitial [144, 152].

$$E_{tr}^{vac}[nH] = \frac{1}{n}(E_{tot}^{nH-v} - E_{tot}^{0H-v}) - (E_{tot}^{1H} - E_{tot}^{0H}) \tag{3.17}$$

$$E_{tr}^{gb}[nH] = \frac{1}{n}(E_{tot}^{nH-gb} - E_{tot}^{0H-gb}) - (E_{tot}^{1H} - E_{tot}^{0H}) \tag{3.18}$$

where $E_{tot}{}^{xH-v}$ (or $E_{tot}{}^{xH-gb}$) denotes the total energy when we have a complex of x

H atoms segregated at a vacancy (or grain boundary) in the system. The trapping energy of the single nth H atom can be estimated by the difference in total trapping energies between n and (n-1) H atoms.

$$\Delta E_{tr}^{vac}[n] = nE_{tr}^{vac}[nH] - (n-1)E_{tr}^{vac}[(n-1)H] \tag{3.19}$$

$$\Delta E_{tr}^{gb}[n] = nE_{tr}^{gb}[nH] - (n-1)E_{tr}^{gb}[(n-1)H] \tag{3.20}$$

3. Results and Discussions

a. Hydrogen Binding at Interstitial and Vacancy

The nearest tetrahedral interstitial (T) is in $\langle 111 \rangle$ direction. The nearest octahedral interstitial (O1) is in $\langle 100 \rangle$ and the second nearest one (O2) is in $\langle 111 \rangle$ as at the center of the unit cell body (Fig. 19a). Using equation 3.15, the calculations on bulk Pd show that absorption energy of H to O-site is -0.1 eV, which is stronger than that at T-site (-0.05 eV). This suggests a preference of H occupation at O-site over another in Pd bulk. However, as the magnitude of this binding energy is low, the stability of H-interstitial complex is subject to other factors.

Usually hydrogen binds stronger to other type of defects such as vacancy and grain boundary. In Fig. 19b we present the variation of H trapping energy along diffusion paths into the vacancy. Trapping energy is calculated with respect to binding energy of one H atom to the octahedral interstitial (the zero level corresponds to the binding energy of H to octahedral interstitial). In agreement with previous works in metals [144, 152], our calculation showed that center of vacancy is a very unfavorable binding site for H (as its trapping energy is very positive). Parts of the curves below octahedral line (zero level) showed possible regions around a vacancy in which H binding is stronger than that at octahedral interstitial in bulk. It indicated that the formation of the nearest-neighbor vacancy makes H binding at octahedral site

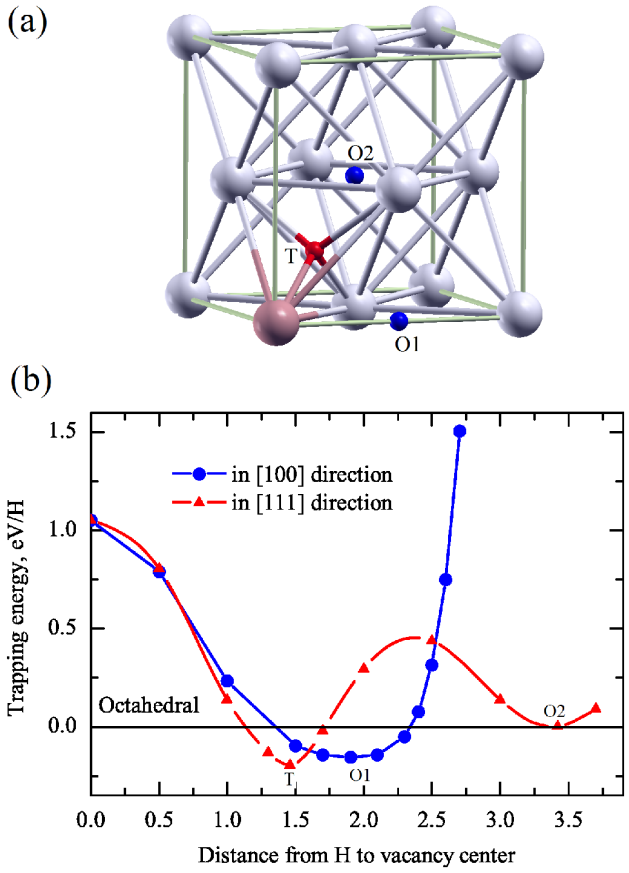

Fig. 19. (a) Atomic configuration of a palladium face-centered cubic unit cell, showing tetrahedral (red) and octahedral (blue) interstices. (b) Variation of trapping energy of H along diffusion paths into the vacancy. The zero level corresponds to energy of H to octahedral interstitial.

stronger (O1 in Fig. 19). However, it is interesting that the most energetically stable site for H-vacancy binding is in ⟨111⟩ direction, close to its tetrahedral position (T in Fig. 19) . This H bonding will be threefold, instead of fourfold, due to one missing Pd (vacancy). Farther in that ⟨111⟩ direction, vacancy has no effect on H binding at its second nearest octahedral interstitial (trapping energy at O2 is zero).

Using local-density approximation (LDA) method, Vekilova et al. [152] reported about a possibility of multiple hydrogen occupancy, in which maximum of six hydro-

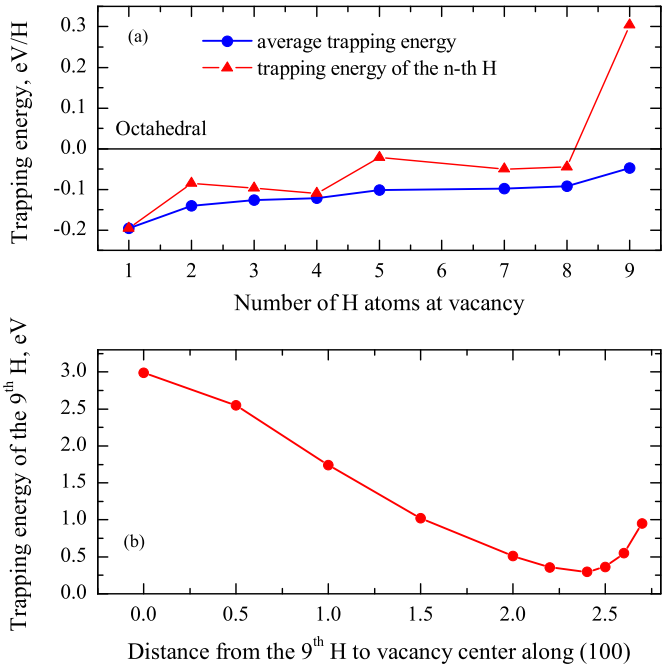

Fig. 20. (a) Variation of H trapping energy as a function of H number at vacancy site. (b) Trapping energy of the 9^{th} H as function of distance in $\langle 100 \rangle$ from vacancy center

gen atoms can be trapped in a monovacancy. The most favorable sites were found to be along directions of $\langle 100 \rangle$ family, as six octahedral sites coordinate a Pd atom. However, in our work with GGA, that configuration of $VacH_6$ is not energetically favorable. Instead, we found that the stable structure of monovacancy with most H will contain eight H atoms, which surround the vacancy at its tetrahedral sites. With this maximum number of H occupations, the H binding is compatitively stronger than that at octahedral site in bulk (Fig. 20a). However, the insertion of any extra H into this $VacH_8$ configuration will result in a positive trapping energy, i.e. the extra H needs to get out and occupy an interstitial site. Fig. 20b shows the variation of trapping energy of the 9^{th} H with respect to its distance from vacancy center in $\langle 100 \rangle$ direction. There is nowhere to fit the 9^{th} H into this $VacH_8$ complex to make a

energetically stable system.

Table VIII. Formation energy of monovacancy, divacancy and influence of hydrogen segregation

Vacancy type	Formation energy E_f, eV
Mono-vacancy	1.17
Mono-vacancy expr. [153]	1.50
Second vacancy in $\langle 100 \rangle$ of $VacH_0$	1.19
Second vacancy in $\langle 110 \rangle$ of $VacH_0$	1.13
Second vacancy in $\langle 100 \rangle$ of $VacH_8$	1.22
Second vacancy in $\langle 110 \rangle$ of $VacH_8$	1.04
Forth vacancy as NN of $VacH_8$	0.36

The vacancy formation process can be affected by different factors, including vacancy at its neighbor sites and concentration of impurity atoms. As shown in Table VIII, GGA method underestimates the vacancy formation energy. Generally, the formation of a di-vacancy is less costly than the formation of two separate vacancies. However, our calculations show that this is correct only in $\langle 110 \rangle$ direction, i.e. di-vacancy formed by the pairing of two nearest neighbors. The formation of the second vacancy site in $\langle 100 \rangle$ direction requires even more energy than that of a new single one. However, occupation of H in the vacancy further reduces the formation energy of the vacancy site in $\langle 110 \rangle$, but increases vacancy formation energy in $\langle 100 \rangle$ direction (Table VIII).

b. Hydrogen Segregation at Grain Boundary

Grain boundaries play a very important role in the issue of impurity transport and segregation. In this subsection, we will discuss the occupation of H at a $\Sigma 5$ (210) grain boundary. Using equation 3.17, the average trapping energy was calculated as a function of H occupation at this GB and presented in Fig. 21. The absorption energy differs from trapping energy by the value of one H binding energy at octahedral

interstitial site. By studying segregation energy, it was widely accepted that H is an interfacial embrittler [154], using Rice-Wang theory [63]. In this work we will reveal the saturated concentration of H segregation at GB and study its total effects, which have been yet reported.

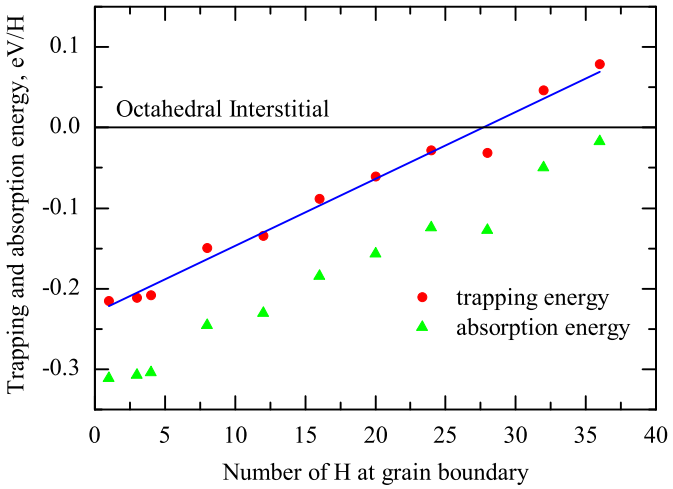

Fig. 21. Average trapping energy as a function of H number at grain boundary region

The average binding energy is negative for H occupations up to 36 atoms, which means an energetically possible complex of GBH_{36}. However, with more than 28 H occupations, the average trapping energy is positive, i.e. further absorption of H is unfavorable; instead, extra H atoms will diffuse into octahedral interstitial sites in bulk. Fig. 22 shows the atomic configuration of Pd bicrystal cells at H-clean state and with 28 H occupation around GB plane. If we take into account only five Pd atom layers around GB, then the local H concentration is roughly $Pd_{20}H_{28}$.

Due to the geometry of GB, there are hollow sites located on GB plane, which will likely host impurity atoms. However, H atoms don't stay in those empty spaces or form hydrogen gas themselves; instead, they bind closely with Pd. The average H-Pd bond length is approximately 1.8 Å, which is roughly equivalent to a bond between a tetrahedral H and Pd in bulk. Interestingly, we found that the most common H-Pd

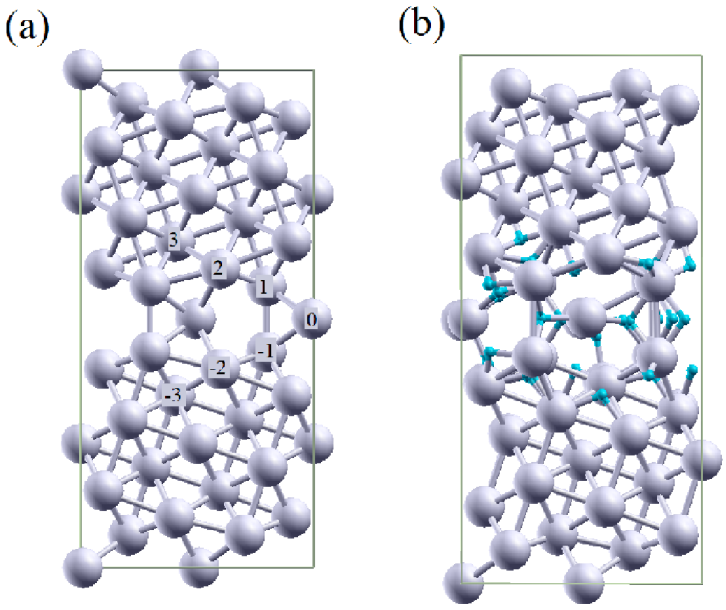

Fig. 22. Atomic configurations of Pd bicrystals: (a) at H-clean state and (b) with saturated segregation of 28 H atoms. Large spheres demonstrate palladium and small ones are hydrogen atoms

bonding around GB is also threefold. This configuration contains an H atom bound with Pd at three vertices of a (quasi-)tetrahedron, while the the forth Pd vertex is missing. This H-Pd binding is identical to the configuration of H-vacancy complex, while H found itself most comfortable at the tetrahedral interstitial, but bonds with only three Pd due to one missing Pd vacancy (Fig. 19a). We should note that while H binds threefold, one Pd atom can also participate in several H-Pd bonds (Fig. 22b).

To differentiate between Pd atom layers at grain boundary, we name them GB1, GB2 ..., depending on how far they are from the grain boundary plane (Fig. 22a). Due to the symmetry characterization of this GB, layers with opposite indices are equivalent (e.g. GB1 and GB-1). When H atoms surround Pd, firstly, they weaken Pd-Pd bond. Secondly, Pd-Pd can even be broken, as there is an expansion between Pd layers due to high H-GB occupancy. For instance, the distance between layers

GB2 and GB-2 increase from 3.83 Å (at H-clean state) up to 4.82 Å at saturated H concentration (28 H atoms for this 80-Pd bicrystal supercell).

Table IX. Formation energy of monovacancy at different sites around grain boundary

Vacancy site	Formation energy E_f, eV
GB1	1.29
GB2	0.48
GB3	1.00
GB4	1.04
GB5	1.06
GB6	1.09

Next, we visit the problem of how H occupation at GB influence the formation of vacancy around GB domain. As presented in Table IX, Pd atoms close to GB plane are easy prone to vacancy formation, except GB0 position (according to formation energy calculation, GB0 is even more stable than a bulk site). After several layers, grain boundary will have no effect on vacancy formation, and E_f value will be equal to that in bulk. It was noted that GB2 (or GB-2) is the most unstable site to form the vacancy. However, the presence of hydrogen doesn't help forming vacancy at grain boundary. For instance, with eight (or twenty-eight) H atoms segregation at grain boundary, the vacancy formation energy at GB2 even increases slightly to 0.55 eV (or 0.63 eV), compared to its value of 0.48 eV in H-clean state. Therefore, unlike H-vacancy binding, H-GB segregation will not initiate hydrogen embrittlement through microvoid formation. Instead, high H occupation at GB results in a decohesion across Pd grain boundary and the hydrogen embrittlement may start by the grain separation at sufficient external stress load. This observation is in agreement with calculations using Rice-Wang model, in which single H was reported to bind stronger to a free surface, other than to a grain boundary in metals [154–156], which implies that H is a GB embrittler by reducing the grain cohesion.

4. Concluding Remarks

We have found the critical or saturated concentrations of H binding at vacancy and grain boundary in Pd crystals. Suggestion for favorable configurations of H-vacancy and H-GB complexes from low to high H occupation were also presented.

While H prefers to occupy octahedral interstitial position in bulk, they are anticipated to fill in tetrahedral sites in case of vacancy. Our calculation showed that one Pd vacancy is capable of storing up to eight H, instead of six as reported previously [152]. Pairing of vacancies is directional and encouraged in $\langle 110 \rangle$ direction, and H presence will further assist multi-vacancy formation or pairing process, which implies the hydrogen embrittlement by connections of microvoids. Numerous experimental observation and theoretical calculations have reached to the same conclusions on hydrogen behavior induce vacancy formation.

In both cases (at vacancy and at grain boundary), hydrogen prefers a threefold bonding with palladium. However, segregation of H at GB results in weakening Pd-Pd bonds across grain boundary. This observation supports the decohesion mechanism of hydrogen embrittlement as evidenced by many experiments.

CHAPTER IV

MOLECULAR DYNAMICS STUDIES

A. Synopsis

Density-Functional Theory method is based on first-principles calculations from solution of many-electron Schrodinger equation and is able to provide fundamental information of physical and chemical processes at electronic level, but its limitation is the size of atomic system and the lack of finite temperature implementation. Molecular Dynamics approach, however, is based on classical mechanics, in which the motions of particles are predicted from the calculations of energy and forces. Compared to quantum methods, Molecular Dynamics made a significant simplifications since it neglects the quantum mechanical effects. If given decent potentials, this method can be accurate in calculating many macroscopic properties and simulating physical phenomena. It allows one to include thermal effects so the calculations can be performed at any elevated temperature.

In this chapter, we used classical molecular dynamics (MD) method for an better understanding on dynamic response of materials structures and effects of temperature, strain and high pressure. Firstly, the fluctuation-based formalism was used to assess thermoelasticity of Al and the behavior of this material. Later, simulations on hydrogen-palladium systems were performed to study the effects of hydrogen interaction, diffusion and segregation in different crystal nanostructures, including defects such as vacancies and grain boundaries. The last project deals with high-pressure shock compression and spallation of Pd bicrystals with a $\Sigma 5$ (210) grain boundary. The MD simulations show that hydrogen maintains highest localization at grain boundaries in the vicinity of ambient temperatures, and grain boundaries are

the preferred nucleation sites for dislocations and voids.

B. Calculations on Finite Temperature Elasticity of Al*

1. Motivation

Development and selection of new materials requires accurate knowledge of their properties as well as reliable experimental and theoretical tools for their characterization. In the particular case of high-temperature structural materials, the component designer needs (at the very least) reliable information on their thermo-elastic behavior over a wide temperature range [157]. Although one may think that this information is readily available, the truth of the matter is that there are significant discrepancies among different experimental studies, even for the most widely used materials.

As an example, we summarize in Fig. 23 published experimental data on the adiabatic C_{12} elastic constant of fcc aluminum as a function of temperature from three different studies [158–161]. In all those experimental investigations, the elastic constants were determined by identifying the resonant frequencies of single crystalline specimens within the kHz to MHz range. In this figure, quantitative and even qualitative differences can be seen among the three different experimental data sets. While the measurements by Gerlich [158], Kamm and Alers [159] and Sutton [160] show a softening of this shear constant with increasing temperature, Tallon [161] (the most recent experimental work on elastic properties of aluminum) reports an actual increase of the C_{12} elastic constant with temperature. Although some of the discrepancies can be explained by the use of different frequency ranges (lower frequencies are used in the

---

*Reprinted from "H. H. Pham, M. E. Williams, P. Mahaffey, M. Radovic, R. Arroyave and T. Cagin. Finite temperature elasticity of fcc Al: Atomistic simulations and ultrasonic measurements. *Physical Review B*, accepted, Apr. 2011".

earlier study by Sutton [160]), the qualitative differences—softening vs. hardening - observed indicate significant systematic problems in at least one of the experimental investigations.

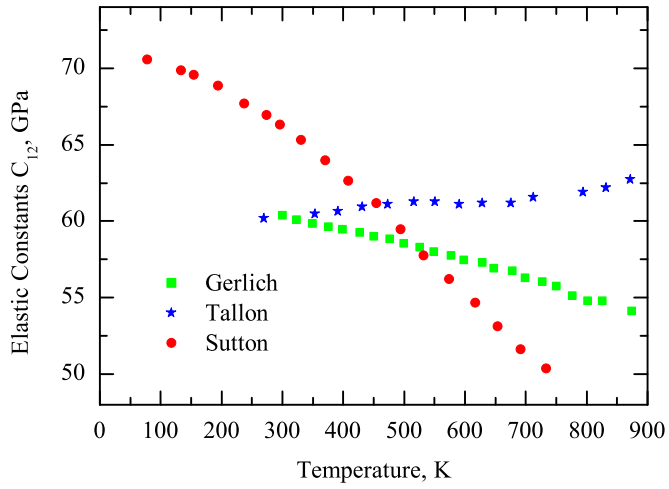

Fig. 23. Experimental adiabatic C_{12} elastic constant as a function of temperature

Given the fact that aluminum has been one of the most widely characterized and simulated metals [160–168], these results are rather surprising. However, it is important to note that the accurate determination of elastic constants through resonance techniques is far from trivial [169], and the actual results are subject to non-negligible degrees of interpretation. Based on the published experimental results [158–161] alone, it is impossible to determine *a priori* which of the published data most accurately represents the actual thermo-elastic behavior of fcc aluminum. In this work, we determine the temperature dependence of the elastic tensor of aluminum. It is expected that computational methodology presented in this work can in turn be used to assess the quality of published thermo-elastic data for other important high temperature structural materials and to predict these properties in cases where no experimental information is available.

2. Computational Details and Thermodynamic Definitions of Elastic Constants

We performed molecular dynamics (MD) calculations on the elastic constants of Al using tight-binding potentials suggested by Rosato et al., which is often referred as RGL [80, 85]. The functional form of RGL interaction potential for an atom $\boldsymbol{a}$ can be described as follows [80, 85]:

$$E_a = AV(r_{ab}) - \xi\rho_a \tag{4.1}$$

in which

$$V(r_{ab}) = \sum_{b\neq a} \exp(-p(\frac{r_{ab}}{r_0} - 1))$$
$$\rho_a = (\sum_{b\neq a} \phi(r_{ab}))^{1/2}$$
$$\phi(r_{ab}) = \exp(-2q(\frac{r_{ab}}{r_0} - 1))$$

where r_0 is the first neighbor atomic distance, and A, ζ, p, q are empirical parameters whose values are obtained by fitting to 0 K properties such as cohesive energy, elastic coefficients and structure stability and they are all published in the work of Cleri et al. [80].

Compared to the Sutton-Chen scheme, which has been successfully utilized to study various bulk properties of metal and metal alloys [170–172], the RGL model is fairly similar in terms of its functional expression and number of fitting parameters. The first term in Eq. 4.1 indicates the atomic repulsions that take into account the increase in kinetic energy of bonding electrons when two ions get close to each other. The Sutton-Chen model introduces a power form instead of an exponential expression to describe these ion-ion repulsions. The second term, having a general formulation of the type -ζ $[\sum_{b\neq a} \psi\ (r_{ab})]^{1/2}$, specifies a many-body cohesion that accounts for the nature of the effective band energy and it balances with repulsion forces in order to

stabilize the crystals. The function $\varphi(r_{ab})$ corresponds to the local electronic charge density induced at site $\boldsymbol{a}$ from atoms at site $\boldsymbol{b}$, and is also described by a power function in the case of the Sutton-Chen model.

The adiabatic (C^S_{ijkl}) and isothermal (C^T_{ijkl}) second-order elastic constants can be defined as second derivatives of internal energy E and the Helmholtz free energy F, respectively, with respect to the homogeneous deformation of the unit cell [110].

$$C^S_{ijkl} = \frac{1}{V_0}\frac{\partial^2 E}{\partial\varepsilon_{ij}\partial\varepsilon_{kl}} \tag{4.2}$$

$$C^T_{ijkl} = \frac{1}{V_0}\frac{\partial^2 F}{\partial\varepsilon_{ij}\partial\varepsilon_{kl}} \tag{4.3}$$

where V_0 and ε_{ij} are the reference volume and strain tensor of the system, respectively.

In turn, the total free energy of a system is described by a Hamiltonian $\boldsymbol{H}$, which is the sum of kinetic contribution and the potential interactions between particles,

$$H = \sum_{a=1}^{N}\frac{p_a^2}{m_a} + \sum_{a<b}U(r_{ab}) \tag{4.4}$$

where p_a and m_a correspond to momentum and mass of the particles, while r_{ab} corresponds to the interatomic separation between atom pairs ***a-b*** and U is the potential energy of the crystal.

Using the definition given above, the statistical fluctuation formula for second-order elastic constants can be derived and presented as follows [87, 92].

$$C_{ijkl} = \frac{2Nk_BT}{V_0}(\delta_{ik}\delta_{lj} + \delta_{il}\delta_{kj}) + \langle\chi_{ijkl}\rangle - \frac{V_0}{k_BT}\left(\langle\sigma_{ij}\sigma_{kl}\rangle - \langle\sigma_{ij}\rangle\langle\sigma_{kl}\rangle\right) \tag{4.5}$$

where N -number of particles, δ - Kronecker delta and σ - microscopic stress tensor.

The first term has a direct connection with temperature and is the kinetic energy component. The second one is called the Born term and related to the strain derivative of the interaction potentials U, in which $< >$ sign denotes ensemble averaging

at the reference volume of the system. The averaging over an adiabatic (NVE) or isothermal (NVT) ensemble will correspond to adiabatic or isothermal elastic constants, respectively.

$$\langle \chi_{ijkl} \rangle = \frac{1}{V_0} \frac{\partial^2 U}{\partial \varepsilon_{ij} \partial \varepsilon_{kl}} \tag{4.6}$$

Both kinetic and Born terms contribute to the intrinsic stiffness of the crystal. The last term in equation 4.5 corresponds to contributions from the fluctuations in the microscopic stress tensor of the crystal. While the Born term can be affected by anharmonic contributions to the free energy, it is the third term in which these contributions become more apparent.

Our MD simulation model consists of 500 Al atoms, in which the cut-off distance covers up to the fifth nearest neighbor [163] (corresponding to $a\sqrt{5/2}$ in fcc crystals), and the simulation time step is chosen to be 1 fs. At first, a thermalization process is conducted by slowly heating the system from 0.001 K (with the temperature increment of 1 K per step) until it reaches the desired temperature. The zero strain state is determined from constant temperature and stress ensembles, by changing the volume of the supercell. Once the reference volume has been obtained, a strict velocity scaling in 50 ps is performed, followed by a preliminary molecular dynamics run of 20 ps to equilibrate the system at the temperature of interest. The elastic constants are then derived from the second derivative of the total energy with respect to the homogeneous deformation of unit cell, as given in equation 4.5, by performing 250,000 steps of constant shape and constant energy simulations (EhN ensemble). The nine elastic constants were calculated separately in order to ensure convergence. It was then verified that the resulting stiffness tensor's symmetry was cubic (i. e. non-vanishing C_{11}, C_{12}, and C_{44}).

3. Results and Discussions

The MD simulations show that the elastic constants of Al decrease with temperature, as a softening in materials is expected. This is in agreement with the DFT calculations as well as with the experimental results by Gerlich [158] and Sutton [160]. The stability criteria for cubic crystals was held for Al, as $C_{44}>0$, $C_{11}>0$ and $C_{11}>C_{12}$. As demonstrated in Fig. 24d, C_{44} declines and the divergence between C_{11} and C_{12} diminishes as temperature increases. Beyond the equilibrium melting point, vanishing C_{11}-C_{12} and C_{44} would correspond to Born melting.

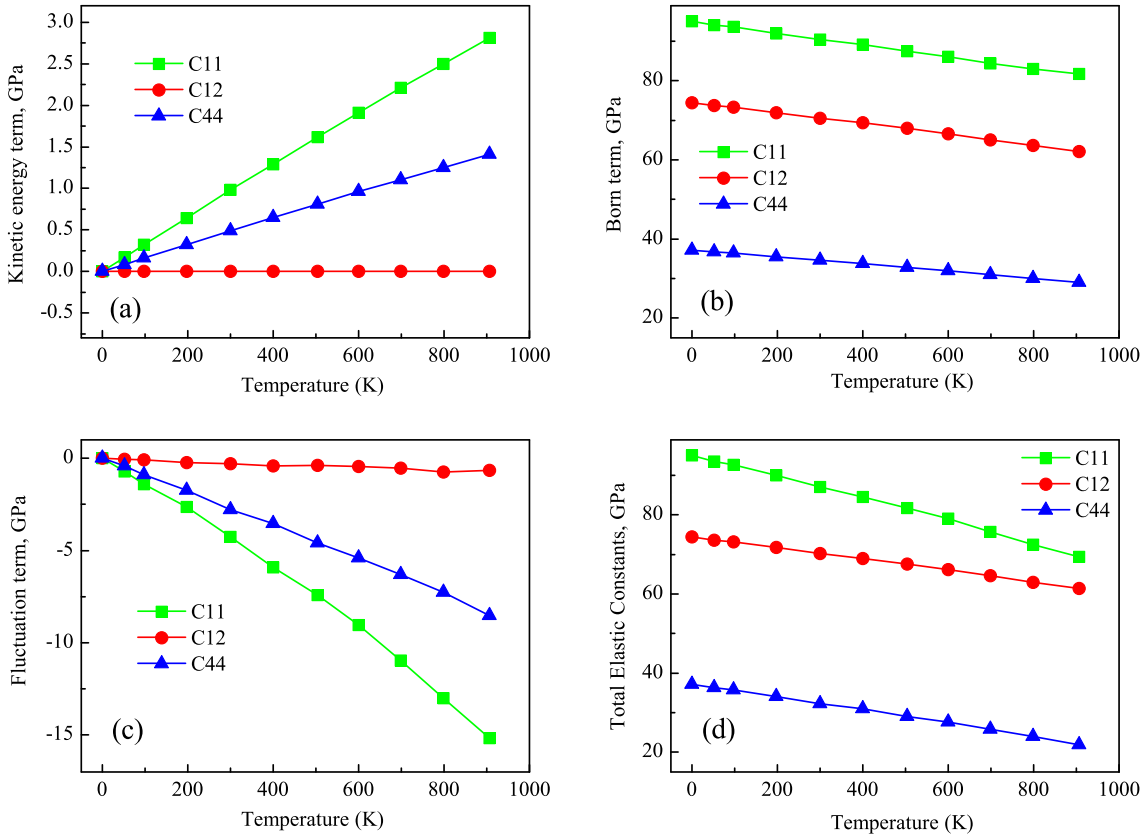

Fig. 24. Calculations on C_{11}, C_{12}, C_{44} at elevated temperatures: (a) kinetic energy contributions, (b) Born term contributions, (c) fluctuation term contributions and (d) total

The kinetic energy, Born term and fluctuation contributions are plotted separately (Fig. 24a-c) in order to elucidate their individual contributions to the stiffness tensor. As can be seen in Fig. 24a, the kinetic contributions are rather small, compared to the other two, and even vanish for C_{12} due to the symmetry of the thermal expansion tensor. Although the kinetic term contributes to a stiffening of C_{11} and C_{44}, its relative contribution to the total elastic constants (Fig. 24d) is insignificant.

It can be seen that the Born term (Fig. 24b) constitutes the most important contribution to the stiffness tensor. It also suggests that this term has almost the same temperature dependence for all three elastic constants. Our calculations indicate that the Born stiffness tensor softens as temperature increases, which is consistent with weakening of interatomic bonds as interatomic distance increases. The fluctuation term (Fig. 24c) represents the contributions to the stiffness tensor due to fluctuations in the microscopic stress tensor. Since these fluctuations are related to the amplitude of atomic displacements, as temperature increases fluctuation contributions to the stiffness tensor also increases. It was shown that fluctuation contributions to the temperature dependence are strongest for C_{11}, almost comparable to the temperature dependence of the Born contribution. In the case of C_{12} and C_{44}, the temperature dependence of the fluctuation term is 100 and 10 times weaker than the corresponding Born term, respectively.

Since the temperature dependence of the Born term is similar for all the elastic coefficients and the contributions from kinetic energy terms are relatively small, the difference in the temperature dependence of the total elastic constants is mostly determined by the behavior of the fluctuation components. Those contributions increase continuously and get up to about 18% and 29% of the Born terms for C_{11} and C_{44}, respectively, at 900K (which is slightly below the experimental melting point of aluminum). In contrast, fluctuation terms in the C_{12} constant are almost negligible.

Fig. 24d shows clearly a linear dependence of elasticity with respect to temperature in the region after room temperature up to 900K. Also, the slopes of C_{11}, C_{12} and C_{44} with respect to temperature reported by these molecular dynamics calculations are in relatively good agreement with those obtained from DFT calculations [7]. In fact, the major disagreement between the classical MD and DFT calculations corresponds to the low temperature C_{12} elastic constant, with C_{44} differing by less than 10% and C_{44} agreeing almost perfectly.

4. Concluding Remarks

Our MD calculations consider all the possible contributions to the stiffness tensor. These calculations suggest that anharmonic contributions (manifested in the fluctuation term) seem to contribute significantly to the temperature dependence of the elastic constants, particularly C_{11}. These anharmonic effects are partly cancelled by the intrinsic kinetic stiffness of the crystal. While the calculated C_{12} obtained through MD simulations is significantly higher than the DFT-calculated and experimentally measured elastic constant, C_{11} and C_{44} agree well with the DFT calculations (errors of less than 10%). In fact, MD and DFT calculations predict a change between 300K and 900K of around 17, 9 and 10 GPa for C_{11}, C_{12} and C_{44}, respectively. More importantly, this is also what we can extract from the data reported by Gerlich [158].

C. Hydrogen Segregation in Palladium Defects and Effects on Mechanical Properties

1. Motivation

In the last decades, molecular simulation emerged as a powerful tool to investigate the crystal structure and geometry of materials. Daw and Baskes [173] developed a semiempirical model of metals and impurities and successfully applied it to treat the problem of brittle fracture in hydrogen-metal system. The method was also used later by Zhong et al. [174] to study fracture of hydrogen-loaded palladium under tensile stress. They reported about the pre-melting disorder caused by hydrogen in single crystal palladium.

Actually, it was accepted that elastic response of hydrogenised metals and alloys changes due to the lattice relaxation and local hydrogen excitation [41, 42, 175, 176]. In general, diffusion of hydrogen atoms in crystals is enabled by their occupations of interstitial positions until they are trapped in open volumes or defects such as vacancies and GBs. In addition, a GB potentially acts as a transport channel and sink of impurity atoms. Therefore, vacancies and GBs may lead to significant localization of hydrogen, with potentially strong consequences on the mechanical behavior of crystalline materials [4].

In this section, we will use classical molecular dynamics (MD) method to direct theoretical investigations on hydrogen diffusion and segregation in palladium single crystal, vacancy-defective crystal and bicrystals, under various conditions (hydrogen concentration, temperature and stress) by means of tensile loading. The interatomic interaction is described by the embedded-atom method (EAM) [82, 173]. This semi-empirical, many-body model describes the total energy of a metal atom as the energy obtained by embedding that atom into the local electron density of its atomic neighbors. Unlike pair potential models, in which the energy is just the sum over pair

Table X. Free volume and free surface in single crystal, vacancy-defective crystal and bicrystal supercells (at 300K)

Crystal models	total vol., nm^3	% free vol.	free surface, nm^2
Single crystal (Pd_{10000})	148.28	1.37	23.79
1%-vacancy crystal ($Pd_{9900}Vac_{100}$)	147.41	1.73	42.39
Bicrystal ($Pd_{5000}Pd_{5000}$)	148.95	1.63	36.71

bonds, the total energy in EAM consists of an embedding energy term and the electrostatic interaction term. The EAM approach was reportedly capable of solving various problems of interests in metals and metal alloys, including defects, impurities, surface, fracture, etc [177]. More specifically, it was also successfully applied to metal hydride problems and hydrogen embrittlement phenomena [178–181]. We used in this work the tabulated hydrogen-palladium EAM interatomic potential provided by Zhou et al. [182].

2. Computational Details

We used a supercell model of 10,000 atoms to simulate face-centered cubic (FCC) single crystal palladium. In case of a bicrystal (i.e. fcc Pd bulk containing a grain boundary), we studied specifically a $\Sigma 5$ (210) grain boundary that separates the supercell into two differently-oriented grains of 5000 Pd atoms on each (Fig. 25). This supercell size (10,000 Pd atoms) yields the convergence of GB surface energy as low as 0.1 meV/Å^2. As a high-angle grain boundary, this GB plane offers considerable free volume for impurity transports and segregation and therefore can be vulnerable to impurity-induced embrittlement (Table X).

Initial H-Pd configurations are always prepared by randomly inserting H into interstitial or empty space inside Pd cells (single crystal, high-vacancy and bicrystal supercell). Afterwards, mechanical properties of H-Pd systems were studied by means

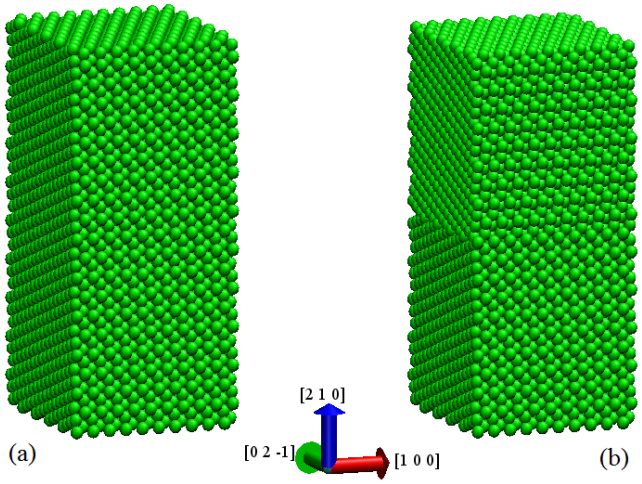

Fig. 25. (a) A 10000-atom model of a FCC Pd_{10000} single crystal tensile specimen and (b) $Pd_{5000}Pd_{5000}$ bicrystal with a $\Sigma 5$ (210) GB

of tensile test simulation. The MD time-step is chosen as 0.5 fs and the periodic boundary conditions are imposed in all x, y and z directions. At each temperature T and hydrogen concentration x_H, the reference zero-strain state was firstly obtained from constant temperature and stress ensembles, by optimizing the volume of the supercell. The uniaxial tension is then applied in the z-direction (which is $\langle 210 \rangle$ for all supercell models, and normal to the GB plane in case of the bicrystal), and is increased gradually in steps of 50 MPa, followed by adequate relaxation to optimum volume (for that external pressure). The tensile strength σ_{TS} is defined as the maximum tensile stress at which the system is sustained as stable. The tensile modulus in the applied tension direction is calculated by fitting the linear stress-strain relation 54 within a small range of strain (up to 0.5%):

$$E_z = \frac{d\sigma_z}{d\varepsilon_z} \tag{4.7}$$

where σ_z and ε_z correspond to stress and resulting strain along applied tension direction (z-axis).

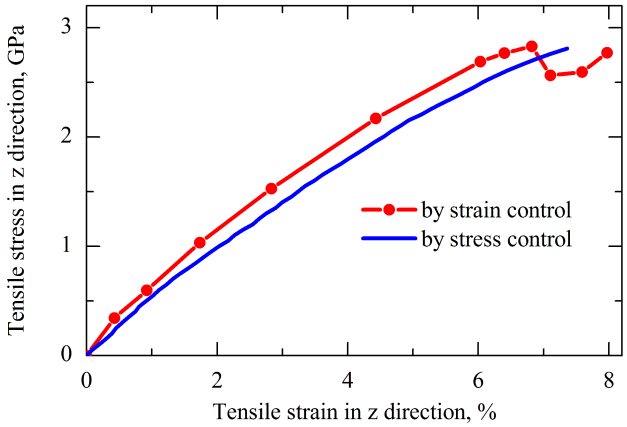

Fig. 26. Stress-strain curves for a Pd single crystal at T=300K and x_H=0.1, obtained using two simulation approaches. Under stress-control, the tensile stress is increased in z-direction and kept as zero in others. Under strain-control, a constant temperature and constant volume ensemble is used to calculate the stress

Fig. 26 shows the stress-strain relationship for a bicrystal at x_H=0.1 and T=300K, from which tensile modulus and tensile strength can be attained. When the applied stress is increased in the z-direction, boundaries of simulation box are allowed to shrink or dilate in order to maintain zero stress in x and y dimensions. In other words, in this method, we control the stress and calculate the subsequent strains (positive along z and negative along x and y), induced by that uniaxial stress. Having knowledge of these domain changes, we were able to conduct a separate simulation, in which the strains are totally controlled and then stress could be calculated based on kinetic energy and interatomic interactions, using canonical ensemble (NVT). This simulation approach is actually a more precise reproduction of the tensile test experiment. However, the stress-strain curves obtained by theses two approaches (stress control and strain control) are virtually similar to each other. In the later method, the stress drops when the material is pulled up to a certain stretch, which indicates the breaking of some interatomic bonds. The ultimate tensile strength, or the maxi-

mum tensile stress at which the material can sustain stable deformation, is identical in both approaches. In this work, we follow the stress-control procedure.

3. Results and Discussions

a. Hydrogen Distributions in Bicrystals

In single crystal and high-vacancy crystal, the crystal structure is homogenous; therefore the distribution of hydrogen is uniform throughout the supercell. However, with the presence of grain boundary in the bicrystal, the segregation of hydrogen is more complicated. At low temperature, hydrogen tends to stick around their initial occupation (where it was assigned by random insertion) due to low diffusion coefficient. However, upon temperature elevation, H gains high kinetic energy and the diffusion process is active. Our simulation showed that GB provides a great gradient for hydrogen diffusion and there is an exceptional activity of hydrogen absorption and segregation in the presence of GB.

At high temperatures (above 400K), the equilibrium distribution of hydrogen was reached quickly in the bicrystal. In addition, tension facilitates the process of hydrogen segregation at the grain boundary. However, we found that, in the vicinity of room temperature, the saturation concentration of H at GB is very high and the diffusion process of H is still very active and far from balance state, even after the zero-stress equilibrium volume has been obtained. Therefore, in order to obtain final H-Pd bicrystal configurations, we firstly heat the initial H-Pd systems up to 300K and maintain at this condition until the saturation of hydrogen at grain boundary was fully reached (approximately after lengthy 10^7 time-steps). The structures used for tensile test then will be obtained from this configuration by heating (or cooling) and sufficiently equilibrating at desired temperatures.

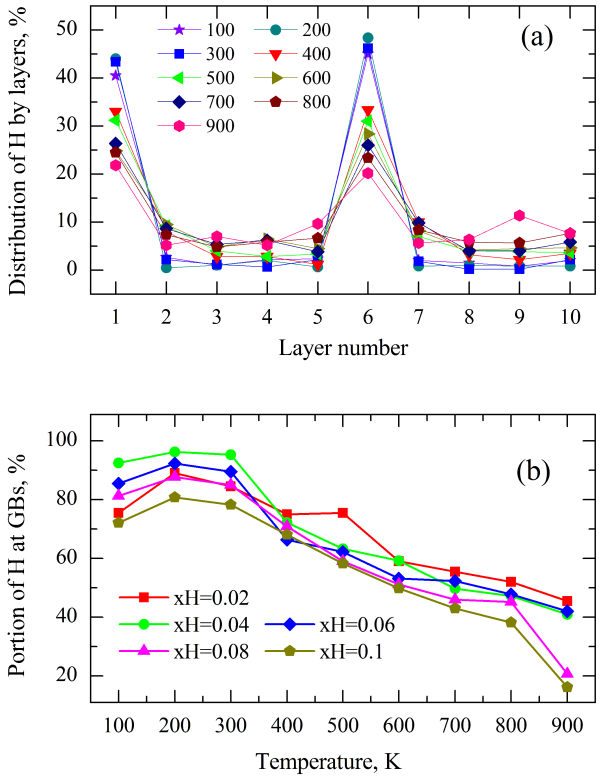

Fig. 27. Distribution of hydrogen inside the bicrystal supercell. (a): Distribution of H by layers when H concentration is 6% atomic. The whole supercell model is divided by 10 layers, in which layer number 1 and 6 contain the grain boundary. (b): Comparison of H content at GB layers for different hydrogen concentration

Fig. 27a showed the final hydrogen distribution along z direction at different temperatures (for the case of $x_H = 0.06$). Hydrogen distribution is monitored by dividing simulation box into 10 layers along z-direction, in which layers number one and six are GB-layers (demonstrated by high peaks). We saw that between 100 and 300K, two GB-layers are able to trap totally up to 90% of all hydrogen throughout the bicrystal cell, therefore the remaining of H inside the bulk becomes trivial. Interestingly, H-GB segregation reduces significantly after transition from 300 to 400K. The percentage of hydrogen atoms that precipitate at GB layers are also shown in Fig. 27b for different

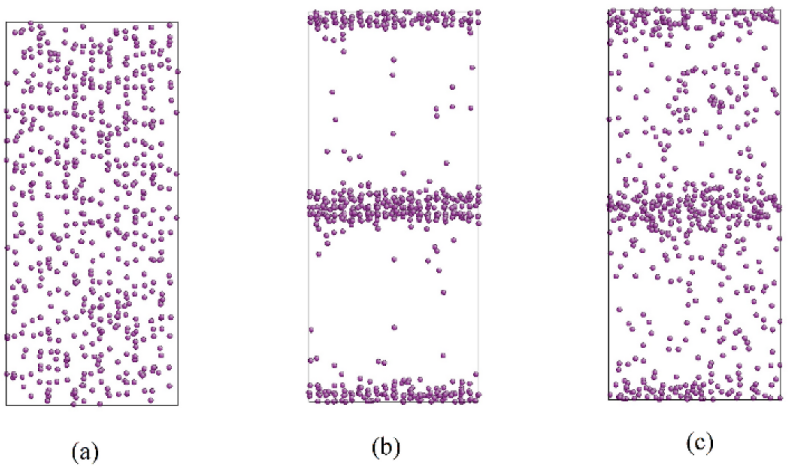

Fig. 28. Atomic configurations of hydrogen at x_H=0.06 (Pd atoms are not shown): (a) Fairly uniform distribution of H in a single crystal at 300K. (b) Final H distribution in the bicrystal at 300K. (c) Final H distribution in the bicrystal at 600K

values of x_H. H distribution is high and consistent in the range of 100-300K and always decreased above 300K (visualization of H distribution with x_H=0.06 is shown in Fig. 28). This phenomenon can be explained by the suggestion that at elevated temperature (above room temperature) H gains sufficiently high energy of motion which exceeds the trapping H-GB energy and therefore is capable of escaping from its GB trap. With increasing x_H, the real number of H atoms segregated at GB increases, but its relative portion compared to total amount of H is highest at moderate x_H= 0.04 (making up to 95% of total H). In fact, there is always a certain amount of H left in crystal bulk and this amount doesn't increase when x_H is low, because extra H will diffuse into grain boundary domains. When there is more excessive amount of hydrogen, the trapping energy of H at GB decreases and therefore its value is no more too high compared to that at interstitial sites in crystal bulk. For that reason, bulk H concentration starts to rise and reduces the portion of H segregated at GB.

In addition, our simulation also shows that external tensile stress facilitates hydrogen segregation at grain boundary.

When hydrogen diffusion is in active progress and H-GB accumulation increases, the simulation box expands as the result of GB expansion. At that moment, it requires less effort to strain the system in normal direction of GB. The tensile test conducted during that transition state will return much lower tensile modulus for output. For that reason, the tensile test should be conducted in bicrystal only after full occupation of H at GB has been reached and H distribution is quite at its final stop.

b. Effects of Various Factors on Pd Mechanical Strength

In this subsection, we will address the combined effects of temperature, hydrogen accumulation and defects (vacancy, grain boundary) on mechanical properties of palladium. As a tensile stress is applied in the $\langle 210 \rangle$ direction, the quantities obtained will correspond to those in $\langle 210 \rangle$, i.e. tensile modulus $E_{[210]}$ and tensile strength $\sigma_{[210]}$.

Table XI. Tensile modulus $E_{[210]}$ of Pd single crystal

T	clean Pd	$PdH_{0.02}$	$PdH_{0.04}$	$PdH_{0.06}$	$PdH_{0.08}$	$PdH_{0.10}$
100	96.44	92.77	89.55	86.36	83.79	80.99
200	91.73	88.70	86.07	83.90	80.68	77.17
300	87.02	83.95	80.71	79.24	76.83	73.53
400	82.93	81.37	78.26	74.47	72.20	69.26
500	78.61	75.93	74.35	69.45	67.87	62.10
600	74.38	69.83	67.58	64.03	58.88	56.52
700	67.91	64.77	61.84	59.68	54.04	51.35
800	63.93	60.23	57.13	53.49	49.34	45.02
900	58.26	54.20	51.27	47.88	44.16	39.16
$\frac{\partial E}{\partial T}$, 10^{-2}	-4.71	-4.83	-4.81	-4.91	-5.19	-5.35

In Table XI and Table XII we listed the tensile modulus $E_{[210]}$ and tensile strength $\sigma_{[210]}$ at different T and x_H for the single crystal; and the data is also visualized in

Table XII. Tensile strength $\sigma_{[210]}$ in Pd single crystal

T	clean Pd	$PdH_{0.02}$	$PdH_{0.04}$	$PdH_{0.06}$	$PdH_{0.08}$	$PdH_{0.10}$
100	5.30	4.80	4.30	4.15	3.65	3.45
200	4.70	4.30	4.05	3.70	3.30	2.99
300	4.30	3.90	3.50	3.10	3.00	2.65
400	3.90	3.45	3.15	2.80	2.45	2.45
500	3.55	3.25	2.95	2.55	2.20	2.10
600	3.25	2.95	2.65	2.35	2.10	2.00
700	2.90	2.70	2.45	2.15	1.95	1.80
800	2.65	2.45	2.20	2.00	1.80	1.65
900	2.30	2.20	1.95	1.70	1.65	1.50
$\frac{\sigma}{\partial T}$, 10^{-3}	-3.60	-3.14	-2.93	-2.88	-2.49	-2.33

Fig. 29. The maps reveal a monotonous decrease for both $E_{[210]}$ and $\sigma_{[210]}$ with increased temperature and hydrogen concentration. The contour lines of $\sigma_{[210]}$ and $E_{[210]}$ surfaces on x-y plane are relatively straight, which suggests that variations of $\sigma_{[210]}$ and $E_{[210]}$ can be locally treated as plane surfaces with respect to T and x_H. However, on a bigger domain, those surfaces have some curvature, as the value of $\frac{\partial \sigma}{\partial T}$ and $\frac{\partial E}{\partial T}$ are not constant. While absolute value of $\frac{\partial \sigma}{\partial T}$ decreases, the magnitude of $\frac{\partial E}{\partial T}$ increase with respect to higher x_H. In other words, the effects from temperature and hydrogen are not totally independent from each other.

In polycrystalline materials, defects such as grain boundaries and vacancies offer open volume, which can alter the mechanical, electrical and optical properties. Also, these domains are accessible to impurity segregation, as a result may lead to stress corrosion. Our calculations show that the presence of vacancy or grain boundary reduces both tensile modulus and tensile strength of the crystal. For instance, at 300K and H-free state, tensile moduli $E_{[210]}$ of vacancy crystal and bicrystal are 82.02 and 73.58, respectively, compared to 87.02 GPa of a single crystal. The reductions in tensile strength are from 4.3 GPa (single crystal) to 3.45 (vacancy crystal) and 3.75 GPa (bicrystal). Zugic and coworkers reported an increase of Young modulus across

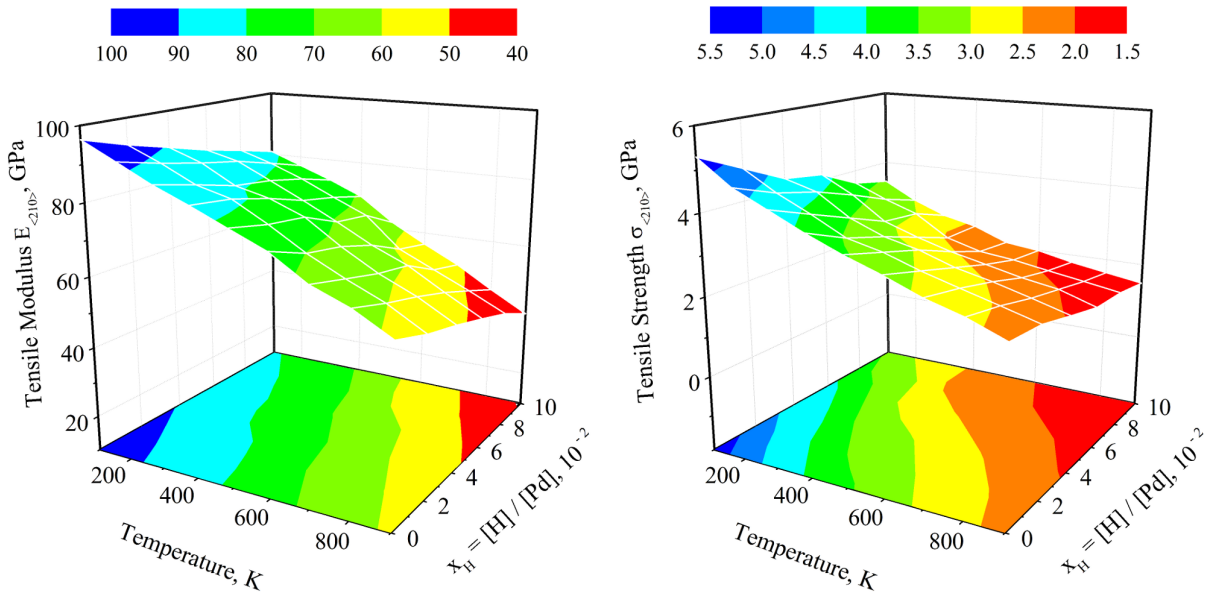

Fig. 29. Maps showing the linear variations of tensile modulus $E_{[210]}$ and tensile strength $\sigma_{[210]}$ as functions of temperature and H concentration x_H

a $\Sigma5$ (100) grain boundary in nickel [183]. In a separate calculation, we also achieved the same conclusion for a $\Sigma5$ (100) GB in palladium. This discrepancy between $\Sigma5$ (100) and $\Sigma5$ (210) can be explained by the geometry factor of each GB type, in which a portion of atoms situated at $\Sigma5$ (100) GB in FCC crystals has short interatomic distance and overweighed the atoms with expanded distances in their contribution to elastic response, due to the anharmonicity of interatomic potential [183]. Meanwhile, the large grain misorientation and big free volume in $\Sigma5$ (210) GB, instead, can result in material softening.

In Fig. 30, we presented tensile modulus and tensile strength of vacancy crystal and bicrystal, for hydrogen concentration $0 \leq x_H \leq 0.1$ and temperatures from 100 to 900K. As stated in the precious subsection, hydrogen atoms are distributed quite uniformly in single crystal and high-vacancy crystal and the hydrogen concentration in these crystals can be referred as a global quantity. Contrariwise, as hydrogen

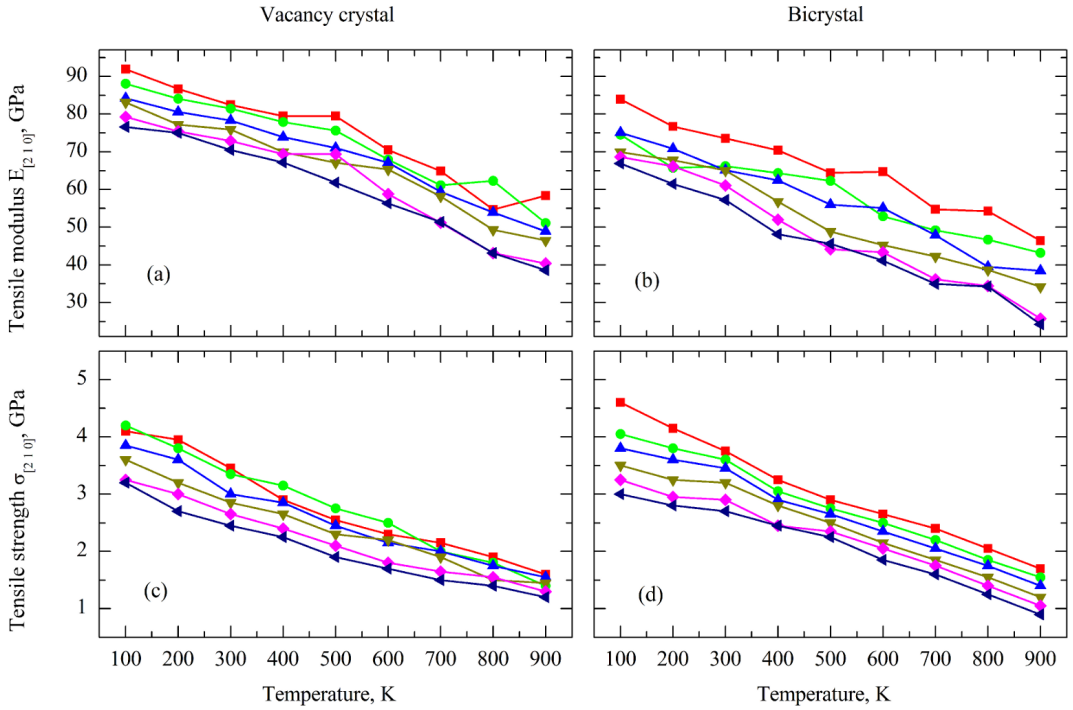

Fig. 30. Tensile modulus $E_{[210]}$ (a and b) and tensile strength $\sigma_{[210]}$ (c and d) as functions of T and total H absorption in high-vacancy crystal and bicrystal

accumulates densely at GB in the bicrystal, then the local concentration of H at GB indeed far exceeds its global value in the whole model cell.

In the presence of a vacancy or a $\Sigma5$ (210) GB, $\sigma_{[210]}$ and $E_{[210]}$ still decrease monotonously with increasing either T or x_H, similar to what was observed in the single crystal case. These fairly linear behaviors of $\frac{\partial\sigma}{\partial T}$ and $\frac{\partial E}{\partial T}$ (with respect to x_H) imply nearly constant second derivatives $\frac{\partial^2\sigma}{\partial C\partial T}$ and $\frac{\partial^2 E}{\partial C\partial T}$ and this suggests to fit the data using $\sigma(T,x) = \sigma_1 T + \sigma_2 x + \sigma_3 Tx + \sigma_4$ and $E(T,x) = e_1 T + e_2 x + e_3 T + e_4$ for tensile strength and tensile modulus, respectively, as functions of temperature and hydrogen absorption. We tabulated the fitting coefficients for palladium single crystal, vacancy-defective crystal and bicrystal in Table XIII.

The values of σ_4 and e_4 correspond to σ and E at infinitesimally low temperature

Table XIII. Fitting coefficients of $E_{[210]}$ and $\sigma_{[210]}$

Fitting coef., GPa	single crystal	1%-vacancy crystal	bicrystal
e_1, 10^{-2}	-4.655	-4.368	-4.081
e_2	-1.291	-1.191	-1.295
e_3, 10^{-2}	-0.062	-0.058	-0.122
e_4	101.313	96.442	84.343
σ_1, 10^{-2}	-0.349	-0.337	-0.345
σ_2	-0.20	-0.132	-0.140
σ_3, 10^{-2}	0.012	0.010	0.009
σ_4	5.353	4.541	4.759

and hydrogen-free state, which stand for characterization of the crystal defects only. With presence of defects, these values drop, for instance, by 16% in tensile modulus and 11% in tensile strength with the effect of grain boundary. Coefficients σ_1, σ_2, e_1, e_2 come from the independent effects of temperature T and hydrogen x_H and their negative values indicate that the increasing T and H absorption will degrade mechanical properties. The weight of temperature effect (σ_1) to tensile modulus doesn't change regardless of different crystals. Also, with the introduction of defects, the hydrogen effect on tensile modulus decreases but its effect on tensile strength varies only slightly. Coefficients σ_3 and e_3 are added as correlated terms that characterize the contribution from T or x_H when the other one is changing. Positive σ_3 also plays its role in describing the concave surface of $\sigma_{[210]}$and an convex surface of $E_{[210]}$ is characterized by a negative e_3. These terms have no significant change for different structure.

To make a specific comparison, in Fig. 31 we showed their stress-strain behaviors at 300K and $x_H = 0.1$, in which the curves for single crystal and vacancy crystal are quite compatible. The bicrystal has a lower tensile modulus (57.2 GPa), compared to single crystal (73.5 GPa) and vacancy-crystal (70.5 GPa). This is also a big degradation (34%) from that of the H-clean single crystal (87 GPa). Interestingly,

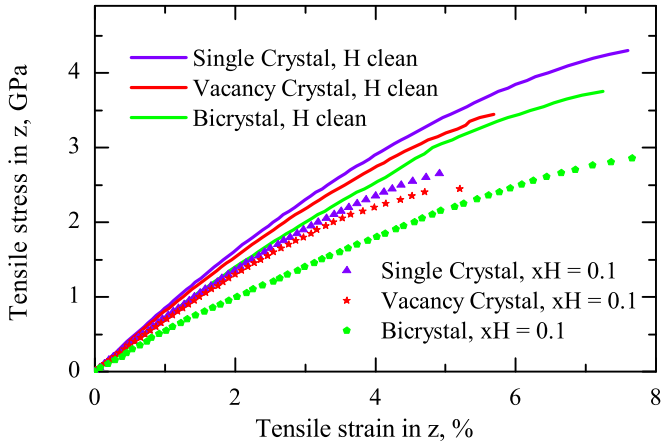

Fig. 31. Comparison of stress-strain curves for different H-Pd systems (T = 300K)

the bicrystal has the same tensile strength with single crystal and vacancy crystal, regardless of being softer. In other words, the bicrystal is more ductile, but still comes to unstable state at the same stress with other two crystals, under high H absorption (x_H= 0.1 cause a 40% reduction in tensile strength). The explanation for a higher ductility in bicrystal is that the mechanical degradation in a single crystal occurs throughout the whole crystal cell rather than at one specific location.

Fig. 32 showed the atomic configuration of defective palladium atoms in single crystal, vacancy crystal and bicrystal, respectively, with x_H= 0.1 at zero tress (a-c) and corresponding maximum tensile strength (d-f). The visualization is based on centrosymmetry parameter [184]. The concentration of defective Pd induced by vacancy and hydrogen is pretty high and this can be the reason why vacancy crystal has a little lower tensile strength compared to bicrystal and single one. We also observed a formation of dislocations that start at grain boundary when external tensile stress reaches to its value of ultimate strength (Fig. 32f). This specific atomic dislocation plane was detected to be $(11\bar{1})$ and belongs to the general family of close-packed slip planes in FCC metals (111). This emission of dislocations could infer

about hydrogen-enhanced localized plasticity (HELP) mechanism [43] and that the failures at stress above tensile strength are plastic rather than brittle. Also, it conforms to experimental observations that fracture process occurs in the vicinity of grain boundary by highly localized plasticity rather than an embrittlement along the grain boundary [43, 185].

4. Concluding Remarks

Grain boundaries are easily exposed to hydrogen segregation due to their tendency to trap H, which can cover up to 90-95% of hydrogen throughout the whole system. Starting at ambient conditions, H atoms are accommodated with sufficient kinetic energy to diffuse from bulk into grain boundaries. Temperatures around ambient conditions provide best conditions to maintain high local H concentration at GBs. Above room temperature, H-GB segregation remarkably decreases. This result supports experimental observations that materials are more susceptible to hydrogen-induced failure around ambient temperatures [149].

In different palladium crystalline structures, the tensile strength and tensile modulus in general decrease monotonously with increasing temperature or total H absorption. The hydrogen effect in mechanical degradation was observed in all single crystal, vacancy-defective crystal and bicrystal. With hydrogen segregation at the grain boundary, the strain or external stress may induce plastic failure in the vicinity of GB.

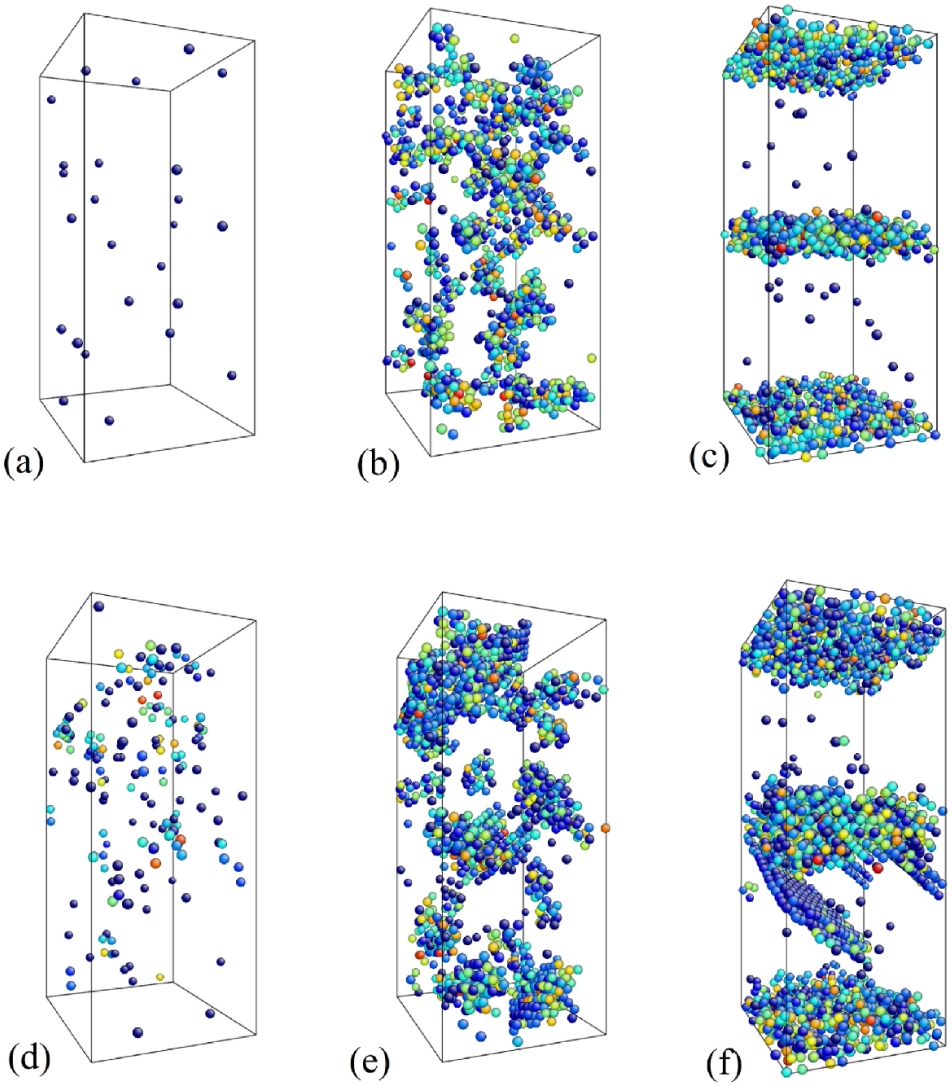

Fig. 32. Atomic configurations of Palladium with x_H=0.1 in single crystal, vacancy crystal and bicrystal, respectively, at zero tensile stress (a,b,c) and ultimate tensile strength (d,e,f). Only defective Pd atoms are shown, based on centrosymmetry parameters

D. Shock Compression and Spallation of Palladium Bicrystals with a Σ5 Grain Boundary[†]

1. Motivation

Shock waves are of interest in a wide range of disciplines and have found a variety of applications [186, 187]. While the highly transient nature of shock events makes extremely challenging the real-time measurements of structure responses, molecular dynamics simulations are useful for understanding at atomistic scales shock physics of a wide range of materials/microstructure, including single crystals, nanocrystalline materials, glasses, polymers, and composites [188–198]. In polycrystalline and nanocrystalline materials, the presence of defects such as grain boundaries (GBs) may have significant effects on "shock response", including dislocation activities, spall damage and wave propagation [189–191, 196, 197]. It is sometimes beneficial to investigate the interaction of a single GB with shock waves; nonetheless, such studies are scarce and limited to Cu and Al [194, 197, 199]. Pd, a platinum group metal, is widely used in many applications but the microstructure effect on its shock response is essentially unexplored. Here as a case study, we perform MD shock simulations of a symmetric $\langle 100 \rangle$ tilt GB in Pd bicrystals [$\Sigma 5/(210)/37°$].

2. Computational Details

We use the Large-scale Atomic/Molecular Massively Parallel Simulator (LAMMPS) and an embedded-atom method potential for Pd [182]. Shock wave simulations adopt the flyer-plate−target impact geometry [88]. The impact direction is along $\langle 210 \rangle$ (the

---

[†]Reprinted with permission from "H. H. Pham, B. Arman, S-N. Luo and T. Cagin. Shock compression and spallation of palladium bicrystals with a Σ5 grain boundary. *Journal of Applied Physics*, vol. 109, no. 8, pp. 86107-86110, Apr. 2011". Copyright © 2011 American Institute of Physics.

x-direction) in both the flyer plate and the target, and it is normal to the GB in the latter. The y- and z-axes are along $\langle\bar{1}20\rangle$ and $\langle001\rangle$, respectively. The single crystal flyer plate and bicrystal target are constructed separately, and then relaxed and equilibrated at ambient conditions; their dimensions are $525\times87\times86$ Å^3 and $1050\times87\times86$ Å^3, respectively. A bicrystal consists of Crystal 1 and 2 (from left to right), and the GB is located either 525 Å or 700 Å away from the impact plane (corresponding to 1/2 or 2/3 of the bicrystal length). We also construct single crystal target of similar dimensions for comparison. The flyer plate and target are assigned positive and negative velocities along the x-axis, respectively, and then combined (about 800 000 atoms in total). The impact velocity of the flyer plate relative to the target is denoted as $u_{\rm imp}$ (approximately two times the shock-state particle velocity), and is in the range of $0.5-1.3$ km s^{-1} in our simulations. Shock simulations are performed with the microcanonical ensemble; periodic boundary conditions are applied only along the y- and z-axes, so there are two free surfaces along the x-axis. The time step for integration of the equation of motion is 1 fs. The local structure is characterized with the centrosymmetry parameter (CS) [200], and local shear, the atomic von Mises shear strain ($\eta_{\rm vM}$) [184]. At a given time t, we obtain the profiles of stress (σ_{ij}), velocity (u), density (ρ) and CS via one-dimensional (1D) binning analysis along the shock direction. Similar simulation and analysis details were presented elsewhere [88, 195].

3. Results and Discussions

a. Dynamic Response of Palladium Σ5 Grain Boundaries to Shock Loading

The $x-t$ diagrams in Fig. 33 show the sequence of shock compression, release, tension and spallation for the single crystal−bicrystal impact at $u_{\rm imp}$=1.3 km s^{-1} (the GB is in the middle of the bicrystal). Upon collision, shocks propagate into the flyer plate

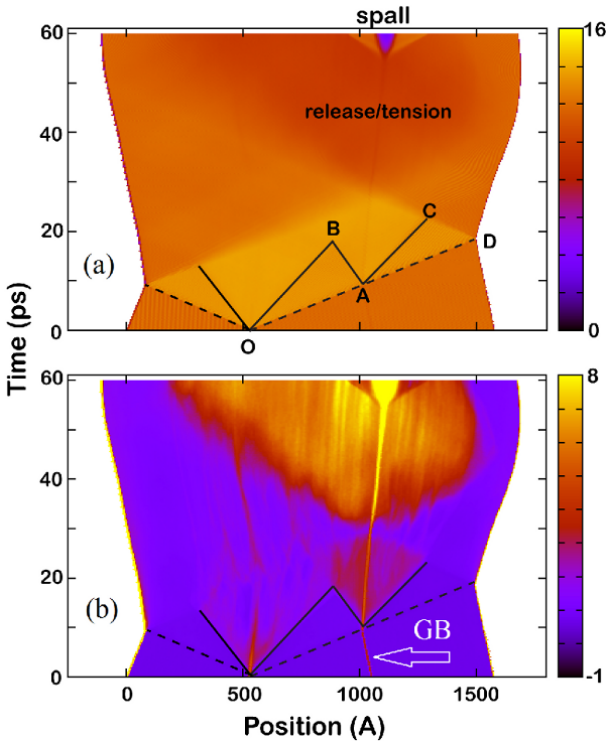

Fig. 33. The $x-t$ diagrams of single crystal−bicrystal impact in terms of ρ (a; in $\mathrm{g\,cm^{-3}}$) and CS (b). Dashed lines denote elastic wave fronts, and solid lines, plastic shock fronts. The labels are the same in (a) and (b)

and the target, and are then reflected at the respective free surfaces (e.g., D) as release fans. The superposition of these two release fans induces a tensile region in the target, and leads to spallation if u_{imp} is sufficiently high. Such processes are manifested in, e.g., the evolution of ρ and CS. We observe two-wave structures (elastic and plastic shocks) in the shock regime originating from the impact plane (OA−OB) and GB (OA−AB, and AD−AC). The GB plasticity (AB and AC) is triggered by the elastic precursor (OA) initiated on the impact plane at $t\approx$9 ps, before the arrival of the plastic shock (OB). During release, compression-induced dislocations are partially reversed, followed by tensile plasticity and solid-state disordering at the GB and around void during spallation; the spallation plane coincides with the GB

[Fig. 33(b)]. If the GB is located at 2/3 the bicrystal length, spallation occurs in Crystal 1 (off the GB). The elastic shock (or precursor) induces a two-wave structure at the GB for $u_{\rm imp}\geq$1.3 km s^{-1}, and this lower limit of $u_{\rm imp}$ is the same for spallation to occur in bicrystals and single crystals. The focus of current work is on sliding, plasticity and void nucleation at GBs, and the case of $u_{\rm imp}$=1.3 km s^{-1} with the GB in the middle of the bicrystal is representative to this end. The following discussion refers to this case unless noted otherwise.

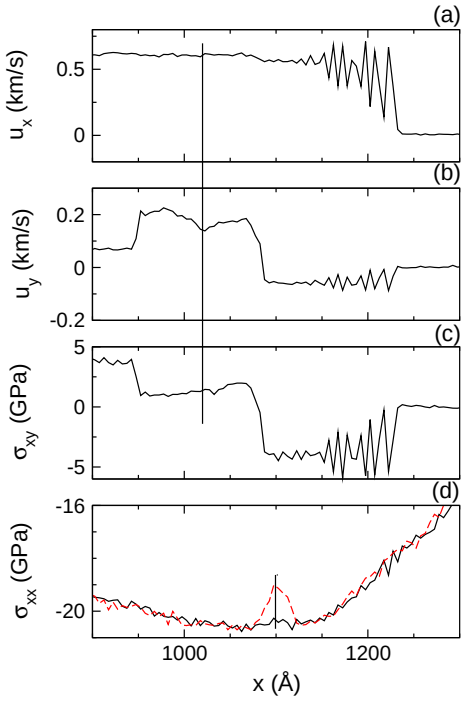

Fig. 34. Profiles of $u_x(x)$ (a), $u_y(x)$ (b) and $\sigma_{xy}(x)$ (c) under the elastic shock (t=13.5 ps), and $\sigma_{xx}(x)$ (d) at tensile states (t=54 ps and 54.5 ps). Vertical bars denote the GB

For single crystals under shock compression, the loading axis and corresponding transverse axes are not necessarily the principal axes of the stress tensor, i.e., σ_{xy}, σ_{yz} or σ_{zx} may not be zero, and u_y or u_z can be finite, depending on the loading geometry. In the case of $u_{\rm imp}$=1.3 km s^{-1} [Fig. 34(b)- 34(c)], σ_{xy} is about 3.7 GPa and u_y is small

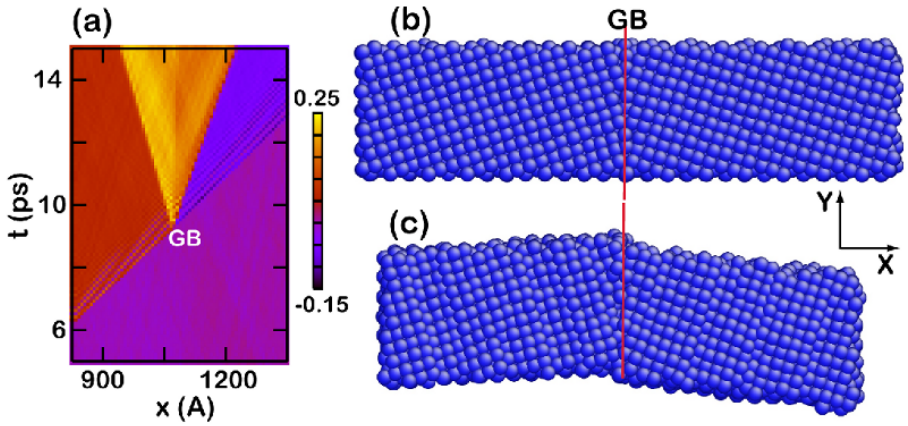

Fig. 35. The $x-t$ diagram in terms of u_y in km s^{-1} (a), and configurations of the same atoms near the GB region before (b) and at 7 ps after the arrival of the elastic shock (c). Only a small portion along the y-axis is shown in (b) and (c)

but finite ($\sim$0.07 km s^{-1}), while σ_{zx}, σ_{zy} and u_z are all zero in Crystal 1 for the elastic shock. When the elastic shock crosses the GB, u_x remains constant but u_y increases; u_y is higher in Crystal 1 than Crystal 2 (an overall negative gradient along the $+x$ direction). The increase in u_y is simply due to the lower shear resistance of the GB to σ_{xy}; this sudden increase leads to "shock waves" propagating into both crystals, which define the affected GB region. Crystal 1 also drags Crystal 2 moving in the $+y$ direction. Thus, the GB region as a whole moves upward with an increase in u_y. When the leading, directly transmitted wave propagates away from the GB region, u_y changes the sign and is reduced slightly in amplitude (~-0.06 km s^{-1}), i.e., the wave undergoes a phase shift of 180°. The dynamics of u_y under the elastic shock is illustrated in Fig. 35(a). The observed GB uplift and phase shift of the transmitted wave, loosely referred to as wave scattering, give rise to the overall distortion of the bicrystal [Fig. 35(b) vs 35(c)]. The gradient in u_y right at the GB (largely from the phase shift) induces GB sliding. The grain orientations are also changed as a result. The GB uplift and sliding occur for all $u_{\rm imp}$ simulated regardless of GB dislocation

activities (see below), but are less pronounced at low values (e.g., 0.5 km s^{-1}). Phase shift also occurs for σ_{xy}, but it relaxes to around zero as a result of GB uplift and sliding. For this particular loading geometry, other stress components, σ_{xx}, σ_{zx} and σ_{zy}, remain unaffected; σ_{yy} and σ_{zz} increase in the GB region due to GB sliding (to relax the von Mises shear stress in a sense). Wave scattering and GB sliding were reported previously in shock and nonshock conditions [190, 196, 201], consistent with present observations.

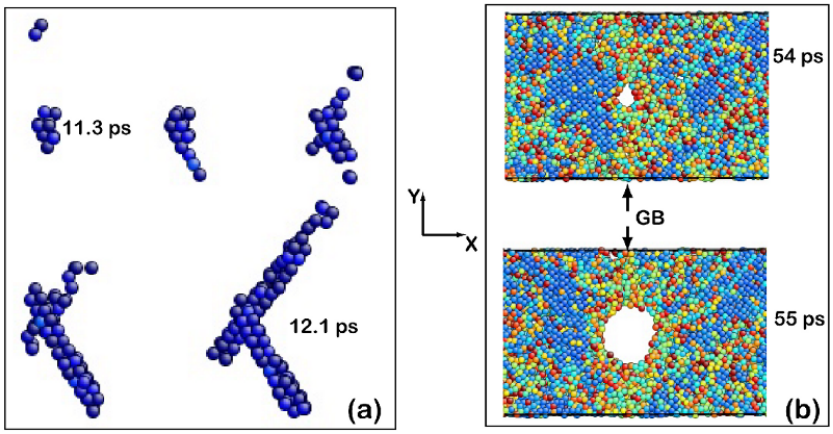

Fig. 36. Snapshots of nucleation and growth of dislocations (stacking faults; a) and a void (b; thin sections) at the GB

Fig. 33(b) shows the structural evolution of Pd crystals during shock, release and tension, and the elastic−plastic transitions are clear in Crystal 1 and the GB region. The higher values of CS is due to the dislocation activities as well as disordering to a lesser extent. Dislocations are emitted immediately from the GB into Crystal 1 and 2, upon the arrival of the elastic shock (OA); an example of dislocation nucleation and growth is shown in Fig. 36(a). The dislocations at GB also contribute to the dip at the GB in $u_y(x)$ [Fig. 34(b)]. During the path of the elastic shock (OA), Crystal 1 remains elastic (until the arrival of the ensuing plastic shock, OB), but it induces plastic waves

emitting from the GB since it is weaker and the source of dislocations. At lower u_{imp}, the GB dislocations are negligible, but GB uplifting and distortion as well as sliding are observed, i.e., GB deformation does not necessarily involve dislocations, although they can interact with each other [196, 201]. The regions near the free surfaces are elastic simply because of the release of the leading elastic shock (DC). During release, dislocations near and away from the GB are largely reversed [Fig. 33(b)], as observed previously in Cu [88, 196]. The opposing release fans induce an evolving tensile region in the target and tension-induced dislocation activities. The GB "disordering" and plasticity during tension are more pronounced than during compression [Fig. 33(b)].

b. Spallation and Void Nucleation at GBs

During tension, the maximum tensile stress ($\sigma_{xx,\text{max}}$) is achieved approximately at the half target thickness, but it does not necessarily represents the spall strength (σ_{sp}) since spallation depends on microstructure. Fig. 34(d) shows the stress profiles $\sigma_{xx}(x)$ near spallation, which is characterized by stress increase or tensile stress relaxation near the spall plane, the GB. (Spallation is also manifested as density reduction and solid-state disordering; Fig. 33). σ_{sp} at the GB is about 20.5 GPa, and $\sigma_{xx,\text{max}}$ is about 20.7 GPa in Crystal 1. σ_{sp} for the single crystal under similar loading conditions is about 20−21 GPa. The GB is not considerably weaker likely because the microstructure effect on σ_{sp} is less pronounced at extreme strain rates as in our simulations. However, the GB is the preferred void nucleation site. The 1D analysis of ρ and CS shows that spallation plane coincides with the GB (Fig. 33), consistent with direct visualization of the voids during spallation [Fig. 36(b)]. (For the GB located at 2/3 the target length, spallation occurs in Crystal 1 rather than the GB because of insufficient tensile stress at the GB.) Prior to void nucleation, the GB itself undergoes disordering under tension, and tension also induces dislocations emitting from the GB.

Similar to compression, tension may also lead to GB sliding and bicrystal distortion. Local heating may be involved as well. These processes as a whole favor the GB for void nucleation. During the void growth, the region immediately surrounding the void is disordered, accompanied by dislocation activities. Such characteristics are also well observed in void nucleation and growth in single crystals and crystals with different defects [88, 196].

4. Concluding Remarks

For conclusion, the results show that for the loading geometry explored, the GB serves a wave scattering center for the transverse motion perpendicular to the GB rotation axis and the shock direction: it induces a phase shift of 180°, an increase in the amplitude of the particle velocity, GB sliding and grain orientation distortion. The GB is the preferred nucleation site for dislocations and voids. Both microstructure and the loading geometry contribute to the dynamic response, and their individual contributions and coupling should be incorporated statistically for developing models of complex solids.

CHAPTER V

SUMMARY

In this work, we used advanced molecular simulation approaches to study the mechanical properties and interactions of materials, related to environment-assisted cracking phenomenon. While Density-Functional Theory can provide fundamental understanding of atomistic behavior at electronic level, classical Molecular Dynamics method allows one to study the dynamic response of particles and include the effects of various conditions such as temperature, strain and high-pressure shock compressions.

The thermo-elastic properties were calculated by means of both DFT and MD, making use of strain energy or fluctuation-based formalism in particular their dependence on increasing pressure and temperature, to assess the behavior of materials beyond elastic limit. It was shown that elasticity is linearly dependent on temperature and pressure. The DFT calculations in this work correspond to properties of materials at 0K conditions; however, the quasi-harmonic theory can be incorporated in order to take into account the thermal effects [7]. Still, the Molecular Dynamics calculations consider all the possible contributions to stiffness tensor.

In the context that the fundamental information is usually hard to obtained using conventional laboratory experiments, Density-Functional Theory and Molecular Dynamics simulations are powerful and accurate tools to give access to nature of many physical and chemical phenomena at atomistic level.

The Density-Functional Theory calculations in this study detail our works on stress-corrosion cracking in Fe and hydrogen embrittlement in Pd, namely the segregation of impurity elements to grain boundaries and vacancies. The bicrystal models with periodic boundary conditions were used to simulate the presence of grain bound-

aries in body-centered cubic Fe and face-centered cubic Pd. The Fe and Pd bicrystal cells contain 24 and 20 layers, respectively, but that is proved sufficiently large for this type of first-principles simulation. The size of cell models guarantees no interactions between grain boundaries due to the boundary conditions. Due to geometry characteristics of grain boundaries, there are certain locations that are more energetically stabilized for occupation of impurities. The impurity elements such as S, P, N, C and B can segregate at Fe grain boundaries by layers and the particles on the same layer have little effects on each other. However, S and P atoms from different layers exert repulsion to the particles of the same kind, subsequently cause the grain boundary separation and open possibility of intergranular crack initiation. N atoms, while segregating to Fe grain boundary, will form the nitride and induce significant volume of void space. This suggests another mechanism of grain boundary degradation. The case of N is worth a further consideration and investigation. The actual effect of N can be clarified by means of tensile test. In addition, we only considered the influence of individual elements in this work; therefore, for a future investigation, we would suggest the study in interaction between different types of impurities. For instance, some experiments offer evidence that the corrosion effect of P is strongly altered in the presence of other alloying elements [58].

In our study, we found the saturated H concentration and configuration of H-Vaccancy and H-GB complexes. Due to the small size of H atoms, they may react to grain boundary space as they do on a surface. H atoms prefer to bind with Pd rather than with each other and the favorite H-Pd bonding is threefold. Since the binding energy of the hydrogen molecule is positive, the formation of hydrogen bubble in gas phase is energetically unfavorable; therefore this mechanism of hydrogen embrittlement is not observed at vacancy and grain boundary in our study. Our DFT study on H-vacancy complex conforms to experimental results that H induces the

formation of superabundant vacancies. This superabundant vacancy formation is a very interesting process in transition metals such as Ni, Pd, etc. To the best of our knowledge, that phenomenon was never studied by means of atomistic simulations.

In order to study the dynamic response of palladium, we use the interatomic potential described by Embedded-Atom Method, which proved capable in dealing with various physical processes and characteristics of metals, including cracks, surfaces, impurities, defects, plasticity, etc. In working with hydrogen diffusion, one issue needing attention is that the relaxation time should be chosen so that it allows the full equilibrium. For instance, in our MD simulation, at 300K and below, it takes about 10 - 20 nanoseconds for hydrogen to achieve the equilibrium state of diffusion in the bicrystal cell. Also, in term of simulation technique regarding the tensile tests, the issue of stress-control and strain-control would also be carefully considered, since it may affect the outcome of simulation results. In the last project, molecular simulation technique proves to be a very convenient approach to study shock phenomenon. Due to the difficulties in measuring shock processes in laboratories, the molecular dynamics simulation is a very efficient tool to tackle this problem. The short nature of shock phenomenon can be simulated by MD method with decent computational expense.

Molecular simulation, in general computational experiments, will never replace the conventional laboratory experiments. However, with its increasing power and fast development, it is expected to be more popular and capable of involving in more area of physics, chemistry and materials science. The results of simulation, more or less, are never totally reliable but the information yielded from simulation will provide supplementary understanding to experiments, as well as guide the directions of future experiments. The biggest advantage of molecular simulations is that it provides fundamental information from the most basic electronic and atomistic level.

REFERENCES

[1] D. Landolt, *Corrosion and Surface Chemistry of Metals*, Lausanne: EPFL Press, 2007.

[2] J. R. Davis, *Corrosion: Understanding the Basics*, Materials Park, Ohio: ASM International, 2000.

[3] M. G. Fontana, *Corrosion Engineering*, New York: McGraw-Hill, 1986.

[4] R. H. Jones, *Stress Corrosion Cracking*, Materials Park, Ohio: ASM International, 1992.

[5] P. E. J. Flewitt and R. K. Wild, *Grain Boundaries: Their Microstructure and Chemistry*, New York: Wiley, 2001.

[6] H. H. Pham and T. Cagin, "Fundamental studies on stress-corrosion cracking in iron and underlying mechanisms," *Acta Materialia*, vol. 58, no. 15, pp. 5142–5149, Sep. 2010.

[7] H. H. Pham, M. E. Williams, Mahaffey. P., M. Radovic, R. Arroyave, and T. Cagin, "Finite temperature elasticity of fcc Al: Atomistic simulations and ultrasonic measurements," *Physical Review B, accepted*, Apr. 2011.

[8] H. H. Pham, A. A. Benzerga, and T. Cagin, "Hydrogen segregation in palladium and effects on mechanical degradation," *APS March Meeting*, vol. 56, no. 1, Mar. 2011.

[9] H. H. Pham and T. Cagin, "Lattice dynamics and third order elastic constants of Fe from first principles," *CMC*, vol. 16, no. 2, pp. 175–194, Apr. 2010.

[10] H. H. Pham and T. Cagin, "Mechanisms of hydrogen embrittlement in palladium crystals: Critical hydrogen binding at vacancy and grain boundary," *in preparation*, 2011.

[11] H. H. Pham, B. Arman, S.-N. Luo, and T. Cagin, "Shock compression and spallation of palladium bicrystals with a Sigma 5 grain goundary," *Journal of Applied Physics*, vol. 109, no. 8, pp. 86107–86110, Apr. 2011.

[12] J. I. Gersten and F. W. Smith, *The Physics and Chemistry of Materials*, New York: John Wiley & Sons, 2001.

[13] W. D. Callister and D. G. Rethwisch, *Materials Science and Engineering : An Introduction*, New York: John Wiley & Sons, 2010.

[14] J. K. Heuer, P. R. Okamoto, N. Q. Lam, and J. F. Stubbins, "Disorder-induced melting in to intergranular sulfur nickel: Implication embrittlement," *Journal of Nuclear Materials*, vol. 301, no. 2-3, pp. 129–141, Mar. 2002.

[15] M. L. Kronberg and F. H. Wilson, "Secondary recrystallization in copper," *Transactions of the American Institute of Mining and Metallurgical Engineers*, vol. 185, no. 8, pp. 501–514, Nov. 1949.

[16] P. Lejček, *Grain Boundary Segregation in Metals*, New York: Springer-Verlag, 2010.

[17] V. Randle, *The Measurement of Grain Boundary Geometry*, Philadelphia: Institute of Physics, 1993.

[18] F. H. Keating, "Chemical manifestations of internal stress," *Journal of the Institute of Metals*, vol. 73, no. 4, pp. 311–331, Jun. 1947.

[19] S. A. Shipilov, "Stress corrosion cracking and corrosion fatigue: A record of progress, 1873-1973," in *Environment-Induced Cracking of Materials*, S. A. Shipilov, R. H. Jones, J.-M. Olive, and R. B. Rebak, Eds. Amsterdam: Elsevier, 2008, pp. 507-557.

[20] Y. Ishida and T. Ozawa, "Grain boundary segregation of tin and electronic and vibrational-state in Zn-Al eutectoid," *Scripta Metallurgica*, vol. 9, no. 10, pp. 1103–1106, Jul. 1975.

[21] E. D. Hondros, "Influence of phosphorus in dilute solid solution on absolute surface and grain boundary energies of iron," *Proceedings of the Royal Society of London Series A*, vol. 286, no. 1407, pp. 479–498, Aug. 1965.

[22] M. Mclean and E. D. Hondros, "Study of grain-boundary grooving at platinum/alumina interface," *Journal of Materials Science*, vol. 6, no. 1, pp. 19–24, Jun. 1971.

[23] M. P. Seah and E. D. Hondros, "Grain boundary embrittlement of steels studied by Auger electron spectroscopy," *Metallurgia and Metal Forming*, vol. 39, no. 3, pp. 100–103, Mar. 1972.

[24] D. A. Muller and M. J. Mills, "Electron microscopy: Probing the atomic structure and chemistry of grain boundaries, interfaces and defects," *Materials Science and Engineering A*, vol. 260, no. 1-2, pp. 12–28, Feb. 1999.

[25] J. Bernardini, P. Gas, E. D. Hondros, and M. P. Seah, "The role of solute segregation in grain-boundary diffusion," *Proceedings of the Royal Society of London Series A*, vol. 379, no. 1776, pp. 159–178, Jan. 1982.

[26] C. M. Liu, T. Nagoya, K. Abiko, and H. Kimura, "Effect of boron on the grain-boundary segregation of phosphorus and intergranular fracture in high-purity Fe-0.2 pct P-B alloys," *Metallurgical Transactions A - Physical Metallurgy and Materials Science*, vol. 23, no. 1, pp. 263–269, Jan. 1992.

[27] A. Larere, M. Guttmann, P. Dumoulin, and C. Roquescarmes, "Auger-electron spectroscopy study of the kinetics of intergranular and surface segregations in nickel during annealing," *Acta Metallurgica*, vol. 30, no. 3, pp. 685–693, Mar. 1982.

[28] A. Partridge and G. J. Tatlock, "The preferential segregation of sulfur to the free-surface of nickel via grain-boundary diffusion," *Scripta Metallurgica et Materialia*, vol. 27, no. 2, pp. 241–241, Jul. 1992.

[29] G. Saindrenan and A. Larere, "Dynamic segregations of sulfur in nickel-270," *Scripta Metallurgica*, vol. 18, no. 9, pp. 969–972, Sep. 1984.

[30] M. Brown, G. Allen, and P. Flewitt, "Nanochemistry of grain boundaries," *Physics World*, vol. 10, no. 5, pp. 45–49, Jul. 1997.

[31] J. K. Heuer, P. R. Okamoto, N. Q. Lam, and J. F. Stubbins, "Relationship between segregation-induced intergranular fracture and melting in the nickel-sulfur system," *Applied Physics Letters*, vol. 76, no. 23, pp. 3403–3405, Jul. 2000.

[32] R. Kirchheim, "Reducing grain boundary, dislocation line and vacancy formation energies by solute segregation," *Acta Materialia*, vol. 55, no. 15, pp. 5139–5148, Sep. 2007.

[33] P. Doig, D. Lonsdale, and P. E. J. Flewitt, "Segregation of embrittling elements to prior austenite grain-boundaries in 2-25Cr-1 Mo steel," *Metal Science*, vol. 16, no. 7, pp. 335–344, Jul. 1982.

[34] R. Herschitz and D. N. Seidman, "Atomic resolution observations of solute atom segregation to stacking-faults in a Co-0.96 atomic percent Nb alloy," *Scripta Metallurgica*, vol. 16, no. 7, pp. 849–854, Jul. 1982.

[35] D. Bouchet, C. Colliex, P. Flora, O. Krivanek, C. Mory, and M. Tence, "Analytical electron-microscopy at the atomic level with parallel electron-energy loss spectroscopy," *Microscopy Microanalysis Microstructures*, vol. 1, no. 5-6, pp. 443–454, Oct. 1990.

[36] R. Jayaram and M. K. Miller, "An APFIM analysis of grain-boundaries and precipitation in boron-doped NiAl," *Surface Science*, vol. 266, no. 1-3, pp. 310–315, Apr. 1992.

[37] D. A. Muller, S. Subramanian, P. E. Batson, J. Silcox, and S. L. Sass, "Structure, chemistry and bonding at grain boundaries in Ni3Al: The role of boron in ductilizing grain boundaries," *Acta Materialia*, vol. 44, no. 4, pp. 1637–1645, Apr. 1996.

[38] V. J. Keast, J. Bruley, P. Rez, J. M. Maclaren, and D. B. Williams, "Chemistry and bonding changes associated with the segregation of Bi to grain boundaries in Cu," *Acta Materialia*, vol. 46, no. 2, pp. 481–490, Jan. 1998.

[39] K. Sieradzki and R. C. Newman, "Stres corrosion cracking," *Journal of Physics and Chemistry of Solids*, vol. 48, no. 11, pp. 1101–1113, Jul. 1987.

[40] R. P. Messmer, D. R. Salahub, K. H. Johnson, and C. Y. Yang, "Interaction of atomic-hydrogen with Ni, Pd, and Pt clusters," *Chemical Physics Letters*, vol. 51, no. 1, pp. 84–89, Oct. 1977.

[41] F. M. Mazzolai, G. Paparo, and R. Franco, "Changes of the Young modulus induced by hydrogen or deuterium in the palladium-silver alloys," *Journal de Physique*, vol. 44, no. 9, pp. 411–417, Dec. 1983.

[42] R. J. Farraro and R. B. Mclellan, "Elastic properties of dilute palladium-hydrogen solid-solutions," *Journal of Physics and Chemistry of Solids*, vol. 39, no. 7, pp. 781–785, Jan. 1978.

[43] H. K. Birnbaum and P. Sofronis, "Hydrogen-enhanced localized plasticity - a mechanism for hydrogen-related fracture," *Materials Science and Engineering, - A Structural Materials Properties Microstructure and Processing*, vol. 176, no. 1-2, pp. 191–202, Mar. 1994.

[44] D. G. Westlake, "A generalized model for hydrogen embrittlement," *ASM Transactions Quarterly*, vol. 62, no. 4, pp. 1000–1006, Dec. 1969.

[45] R. A. Oriani and P. H. Josephic, "Equilibrium aspects of hydrogen-induced cracking of steels," *Acta Metallugica*, vol. 22, no. 9, pp. 1065–1074, Sep. 1974.

[46] M. Hashimoto, Y. Ishida, R. Yamamoto, M. Doyama, and T. Fujiwara, "Atomistic and electronic studies of the grain-boundary segregation - phosphorus or boron in iron," *Journal of Metals*, vol. 35, no. 8, pp. A24–A24, Jun. 1983.

[47] M. Hashimoto, Y. Ishida, S. Wakayama, R. Yamamoto, M. Doyama, and T. Fujiwara, "Fe-P and Fe-B alloys: Electronic-structure and intergranular embrittlement," *Acta Metallurgica*, vol. 32, no. 1, pp. 13–20, Jan. 1984.

[48] M. Hashimoto, Y. Ishida, R. Yamamoto, and M. Doyama, "Atomistic studies of grain-boundary segregation in Fe-P and Fe-B alloys: atomic-structure and stress-distribution," *Acta Metallurgica*, vol. 32, no. 1, pp. 1–11, Jan. 1984.

[49] S. Wakayama, M. Hashimoto, Y. Ishida, R. Yamamoto, and M. Doyama, "Atomistic studies of grain-boundary segregation in Fe-P and Fe-B slloys: Vibrational-states of atoms at the grain-boundaries," *Acta Metallurgica*, vol. 32, no. 1, pp. 21–27, Jan. 1984.

[50] C. L. Briant and R. P. Messmer, "Electronic effects of sulfur in nickel: A model for grain-boundary embrittlement," *Philosophical Magazine B - Physics of Condensed Matter Statistical Mechanics Electronic Optical and Magnetic Properties*, vol. 42, no. 4, pp. 569–576, Oct. 1980.

[51] C. L. Briant and R. P. Messmer, "An electronic model for the effect of alloying elements on the phosphorus induced grain-boundary embrittlement of steel," *Acta Metallurgica*, vol. 30, no. 9, pp. 1811–1818, Sep. 1982.

[52] C. L. Briant and A. I. Taub, "Grain-boundary segregation of boron and sulfur and its effect on ductility in rapidly solidified Ni-base L12 compounds," *Acta Metallurgica*, vol. 36, no. 10, pp. 2761–2770, Oct. 1988.

[53] A. H. Cottrell, "Unified theory of effects of segregated interstitials on grain-boundary cohesion," *Materials Science and Technology*, vol. 6, no. 9, pp. 807–810, Sep. 1990.

[54] G. S. Painter and F. W. Averill, "Effects of segregation on grain-boundary cohesion - a density-functional cluster model of boron and sulfur in nickel," *Physical Review Letters*, vol. 58, no. 3, pp. 234–237, Jan. 1987.

[55] S. P. Tang, A. J. Freeman, and G. B. Olson, "Local-density studies of the structure and electronic-properties of B and S in an Fe grain-boundary," *Physical Review B*, vol. 50, no. 1, pp. 1–4, Jul. 1994.

[56] R. Q. Wu, A. J. Freeman, and G. B. Olson, "First principles determination of the effects of phosphorus and boron on iron grain-boundary cohesion," *Science*, vol. 265, no. 5170, pp. 376–380, Jul. 1994.

[57] R. Q. Wu, A. J. Freeman, and G. B. Olson, "Effects of carbon on Fe-grain-boundary cohesion: First-principles determination," *Physical Review B*, vol. 53, no. 11, pp. 7504–7509, Mar. 1996.

[58] W. T. Geng, A. J. Freeman, R. Wu, C. B. Geller, and J. E. Raynolds, "Embrittling and strengthening effects of hydrogen, boron, and phosphorus on a sigma 5 nickel grain boundary," *Physical Review B*, vol. 60, no. 10, pp. 7149–7155, Sep. 1999.

[59] W. T. Geng, A. J. Freeman, R. Wu, and G. B. Olson, "Effect of Mo and Pd on the grain-boundary cohesion of Fe," *Physical Review B*, vol. 62, no. 10, pp. 6208–6214, Sep. 2000.

[60] R. W. Smith, W. T. Geng, C. B. Geller, R. Wu, and A. J. Freeman, "The effect of Li, He and Ca on grain boundary cohesive strength in Ni," *Scripta Materialia*, vol. 43, no. 10, pp. 957–961, Oct. 2000.

[61] L. P. Zhong, R. Q. Wu, A. J. Freeman, and G. B. Olson, "Charge transfer mechanism of hydrogen-induced intergranular embrittlement of iron," *Physical Review B*, vol. 62, no. 21, pp. 13938–13941, Dec. 2000.

[62] Y. Zhang, G. H. Lu, T. M. Wang, S. H. Deng, X. L. Shu, M. Kohyama, and R. Yamamoto, "First-principles study of the effects of segregated Ga on an Al grain boundary," *Journal of Physics - Condensed Matter*, vol. 18, no. 22, pp. 5121–5128, Jun. 2006.

[63] J. R. Rice and J. S. Wang, "Embrittlement of interfaces by solute segregation," *Materials Science and Engineering A - Structural Materials Properties Microstructure and Processing*, vol. 107, pp. 23–40, Jan. 1989.

[64] W. T. Geng, A. J. Freeman, and G. B. Olson, "Influence of alloying additions on the impurity induced grain boundary embrittlement," *Solid State Communications*, vol. 119, no. 10-11, pp. 585–590, Aug. 2001.

[65] W. T. Geng, A. J. Freeman, and G. B. Olson, "Atomic size effect in impurity induced grain boundary embrittlement," *Materials Transactions*, vol. 47, no. 8, pp. 2113–2114, Aug. 2006.

[66] M. Kim, C. B. Geller, and A. J. Freeman, "The effect of interstitial N on grain boundary cohesive strength in Fe," *Scripta Materialia*, vol. 50, no. 10, pp. 1341–1343, May. 2004.

[67] M. Yamaguchi, M. Shiga, and H. Kaburaki, "Energetics of segregation and embrittling potency for non-transition elements in the Ni Sigma 5 (012) symmetrical tilt grain boundary: A first-principles study," *Journal of Physics*, vol. 16, no. 23, pp. 3933–3956, Jun. 2004.

[68] M. Yamaguchi, M. Shiga, and H. Kaburaki, "Grain boundary decohesion by impurity segregation in a nickel-sulfur system," *Science*, vol. 307, no. 5708, pp. 393–397, Jan. 2005.

[69] M. Yamaguchi, M. Shiga, and H. Kaburaki, "Grain boundary decohesion by sulfur segregation in ferromagnetic iron and nickel - a first-principles study," *Materials Transactions*, vol. 47, no. 11, pp. 2682–2689, Nov. 2006.

[70] H. H. Kart, M. Uludogan, and T. Cagin, "DFT studies of sulfur induced stress corrosion cracking in nickel," *Computational Materials Science*, vol. 44, no. 4, pp. 1236–1242, Feb. 2009.

[71] H. H. Kart and T. Cagin, "The effects of boron impurity atoms on nickel Sigma 5 (012) grain boundary by first principles calculations," *Journal of Achievement in Materials and Manufacturing Engineering*, vol. 30, no. 2, pp. 177–181, Jun. 2008.

[72] D. Briggs and M. P. Seah, *Practical Surface Analysis*, New York: Wiley, 1990.

[73] A. Benninghoven, F. G. Rdenauer, and H. W. Werner, *Secondary Ion Mass Spectrometry: Basic Concepts, Instrumental Aspects, Applications and Trends*, New York: Wiley, 1987.

[74] D. C. Young, *Computational Chemistry: A Practical Guide for Applying Techniques to Real World Problems*, New York: Wiley, 2001.

[75] J. Hafner, "Atomic-scale computational materials science," *Acta Materialia*, vol. 48, no. 1, pp. 71–92, Jan. 2000.

[76] W. Kohn and L. J. Sham, "Self-consistent equations including exchange and correlation effects," *Physical Review*, vol. 140, no. 4A, pp. 1133–1138, Nov. 1965.

[77] J. P. Perdew and W. Yue, "Accurate and simple density functional for the electronic exchange energy - generalized gradient approximation," *Physical Review B*, vol. 33, no. 12, pp. 8800–8802, Jul. 1986.

[78] J. P. Perdew and Y. Wang, "Accurate and simple analytic representation of the electron-gas correlation-energy," *Physical Review B*, vol. 45, no. 23, pp. 13244–13249, Jul. 1992.

[79] J. P. Perdew, K. Burke, and M. Ernzerhof, "Generalized gradient approximation made simple," *Physical Review Letters*, vol. 77, no. 18, pp. 3865–3868, Oct. 1996.

[80] F. Cleri and V. Rosato, "Tight-binding potentials for transition metals and alloys," *Physical Review B*, vol. 48, no. 1, pp. 22–33, Jul. 1993.

[81] J. K. Norskov, "Covalent effects in the effective-medium theory of chemical-binding - hydrogen heats of solution in the 3d-metals," *Physical Review B*, vol. 26, no. 6, pp. 2875–2885, Sep. 1982.

[82] M. S. Daw and M. I. Baskes, "Embedded-atom method - derivation and application to impurities, surfaces, and other defects in metals," *Physical Review B*, vol. 29, no. 12, pp. 6443–6453, Jun. 1984.

[83] M. W. Finnis and J. E. Sinclair, "A simple empirical n-body potential for transition metals," *Philosophical Magazine A*, vol. 50, no. 1, pp. 45–55, Jan. 1984.

[84] A. P. Sutton and J. Chen, "Long-range Finnis-Sinclair potentials," *Philosophical Magazine Letters*, vol. 61, no. 3, pp. 139–146, Mar. 1990.

[85] V. Rosato, M. Guillope, and B. Legrand, "Thermodynamical and structural-properties of fcc transition-metals using a simple tight-binding model," *Philosophical Magazine A - Physics of Condensed Matter Structure Defects and Mechanical Properties*, vol. 59, no. 2, pp. 321–336, Feb. 1989.

[86] D. Frenkel and B. Smit, *Understanding Molecular Simulation: From Algorithms to Applications*, London: Academic, 2002.

[87] T. Cagin and J. R. Ray, "3rd-order elastic-constants from molecular-dynamics - theory and an example calculation," *Physical Review B*, vol. 38, no. 12, pp. 7940–7946, Oct. 1988.

[88] S.-N. Luo, Q. An, T. C. Germann, and L.-B. Han, "Shock-induced spall in solid and liquid Cu at extreme strain rates," *Journal of Applied Physics*, vol. 106, no. 1, pp. 013502, Jul. 2009.

[89] D. Hull and D. J. Bacon, *Introduction to Dislocations*, Oxford: Butterworth-Heinemann, 2001.

[90] A. Lew, K. Caspersen, E. A. Carter, and M. Ortiz, "Quantum mechanics based multiscale modeling of stress-induced phase transformations in iron," *Journal of the Mechanics and Physics of Solids*, vol. 54, no. 6, pp. 1276–1303, Jun. 2006.

[91] Y. Hiki, "Higher-order elastic-constants of solids," *Annual Review of Materials Science*, vol. 11, pp. 51–73, Aug. 1981.

[92] T. Cagin and B. M. Pettitt, "Elastic-constants of nickel - variations with respect to temperature and pressure," *Physical Review B*, vol. 39, no. 17, pp. 12484–12491, Jun. 1989.

[93] R. A. Graham, "Determination of third-order and fourth-order longitudinal elastic-constants by shock compression techniques - application to sapphire and fused quartz," *Journal of the Acoustical Society of America*, vol. 51, no. 5, pp. 1576–1581, Apr. 1972.

[94] X. D. Song and P. G. Richards, "Seismological evidence for differential rotation of the Earth's inner core," *Nature*, vol. 382, no. 6588, pp. 221–224, Jul. 1996.

[95] G. Steinle-Neumann, L. Stixrude, R. E. Cohen, and O. Gulseren, "Elasticity of iron at the temperature of the Earth's inner core," *Nature*, vol. 413, no. 6851, pp. 57–60, Sep. 2001.

[96] L. Stixrude and R. E. Cohen, "High-pressure elasticity of iron and anisotropy of the Earth's inner core," *Science*, vol. 267, no. 5206, pp. 1972–1975, Mar. 1995.

[97] I. J. Fritz and R. A. Graham, "Second-order elastic-constants of high-purity vitreous silica," *Journal of Applied Physics*, vol. 45, no. 9, pp. 4124–4125, May 1974.

[98] K. Brugger, "Thermodynamic definition of higher order elastic coefficients," *Physical Review A*, vol. 133, no. 6A, pp. 1611–1612, Mar. 1964.

[99] Y. Nakagawa, K. Yamanouc, and K. Shibayam, "Third-order elastic-constants of lithium-niobate," *Journal of Applied Physics*, vol. 44, no. 9, pp. 3969–3974, Mar. 1973.

[100] A. S. Johal and D. J. Dunstan, "Reappraisal of experimental values of third-order elastic constants of some cubic semiconductors and metals," *Physical Review B*, vol. 73, no. 2, pp. 24106, Jan. 2006.

[101] T. Cagin, N. Karasawa, and W. A. Dasgupta, S. Goddard, "Thermodynamic and elastic properties of polyethylene at elevated-temperature," in *Computational Methods in Materials Science*, J. E. Mark, M. E. Glicksman, and S. Marsh, Eds. San Francisco: Materials Research Society, 1992, pp. 61-66.

[102] T. Cagin, K. Kimura, Y. Qi, H. Li, H. Ikeda, W. L. Johnson, and W. A. Goddard, "Calculation of mechanical, thermodynamic and transport properties of metallic glass formers," in *Bulk Metallic Glasses*, W. L. Johnson, A. Inoue, and C. T. Liu, Eds. Pennsylvania: Materials Research Society, 1999, pp. 43-48.

[103] M. Lopuszynski and J. A. Majewski, "Ab initio calculations of third-order elastic constants and related properties for selected semiconductors," *Physical Review B*, vol. 76, no. 4, pp. 45202, Jul. 2007.

[104] O. H. Nielsen, "Optical phonons and elasticity of diamond at megabar stresses," *Physical Review B*, vol. 34, no. 8, pp. 5808–5819, Oct. 1986.

[105] J. J. Zhao, J. M. Winey, and Y. M. Gupta, "First-principles calculations of second- and third-order elastic constants for single crystals of arbitrary symmetry," *Physical Review B*, vol. 75, no. 9, pp. 94105, Mar. 2007.

[106] M. Uludogan, D. P. Guarin, Z. E. Gomez, T. Cagin, and W. A. Goddard, "DFT studies on ferroelectric ceramics and their alloys: BaTiO3, PbTiO3, SrTiO3, AgNbO3, AgTAO(3), PbxBa(1-x)TiO3 and Sr7(x)Ba(1-x)TiO(3)," *Computer Modeling in Engineering & Sciences*, vol. 24, no. 2-3, pp. 215–238, Feb. 2008.

[107] S. O. Kart, M. Tomak, M. UludoganUludogan, and T. Cagin, "Structural, thermodynamical, and transport properties of undercooled binary Pd-Ni alloys," *Materials Science and Engineering A*, vol. 435, pp. 736–744, Nov. 2006.

[108] C. Sevik and T. Cagin, "Mechanical and electronic properties of CeO2, ThO2, and (Ce,Th)O2 alloys," *Physical Review B*, vol. 80, no. 1, pp. 14108, Jul. 2009.

[109] F. D. Murnaghan, *Finite Deformation of an Elastic Solid*, New York: Dover Publications, 1967.

[110] D. C. Wallace, *Thermodynamics of Crystals*, New York: Wiley, 1972.

[111] M. J. Mehl, J. E. Osburn, D. A. Papaconstantopoulos, and B. M. Klein, "Structural-properties of ordered high-melting-temperature intermetallic alloys from 1st-principles total-energy calculations," *Physical Review B*, vol. 41, no. 15, pp. 10311–10323, May 1990.

[112] J. F. Nye, *Physical Properties of Crystals - Their Representation by Tensors and Matrices*, Oxford: Clarendon Press, 1985.

[113] F. G. Fumi, "3rd-order elastic coefficients of crystals," *Physical Review*, vol. 83, no. 6, pp. 1274–1275, Sep. 1951.

[114] G. Kresse and J. Furthmuller, "Efficient iterative schemes for ab initio total-energy calculations using a plane-wave basis set," *Physical Review B*, vol. 54, no. 16, pp. 11169–11186, Oct. 1996.

[115] P. E. Blöchl, "Projector augmented-wave method," *Physical Review B*, vol. 50, no. 24, pp. 17953–17979, Dec. 1994.

[116] H. J. Monkhorst and J. D. Pack, "Special points for Brillouin-zone integrations," *Physical Review B*, vol. 13, no. 12, pp. 5188–5192, Jun. 1976.

[117] C. S. Yoo, J. Akella, A. J. Campbell, H. K. Mao, and R. J. Hemley, "Phase diagram of iron by in-situ X-ray diffraction: Implications for Earth core," *Science*, vol. 270, no. 5241, pp. 1473–1475, Dec. 1995.

[118] A. Jephcoat and P. Olson, "Is the inner core of the Earth pure iron," *Nature*, vol. 325, no. 6102, pp. 332–335, Jan. 1987.

[119] A. Laio, S. Bernard, G. L. Chiarotti, S. Scandolo, and E. Tosatti, "Physics of iron at Earth's core conditions," *Science*, vol. 287, no. 5455, pp. 1027–1030, Feb. 2000.

[120] X. W. Sha and R. E. Cohen, "Lattice dynamics and thermodynamics of bcc iron under pressure: First-principles linear response study," *Physical Review B*, vol. 73, no. 10, pp. 104303, Mar. 2006.

[121] D. E. Jiang and E. A. Carter, "Carbon dissolution and diffusion in ferrite and austenite from first principles," *Physical Review B*, vol. 67, no. 21, pp. 214103, Jun. 2003.

[122] J. H. Li, S. H. Liang, H. B. Guo, and B. X. Liu, "Four-parameter equation of state of solids," *Applied Physics Letters*, vol. 87, no. 19, pp. 194111, Nov. 2005.

[123] P. Vinet, J. Ferrante, J. H. Rose, and J. R. Smith, "Compressibility of solids," *Journal of Geophysical Research - Solid Earth and Planets*, vol. 92, no. B9, pp. 9319–9325, Aug. 1987.

[124] J. H. Wang, S. Yip, S. R. Phillpot, and D. Wolf, "Crystal instabilities at finite strain," *Physical Review Letters*, vol. 71, no. 25, pp. 4182–4185, Dec. 1993.

[125] H. Hasegawa, M. W. Finnis, and D. G. Pettifor, "Phonon softening in ferromagnetic bcc iron," *Journal of Physics F - Metal Physics*, vol. 17, no. 10, pp. 2049–2055, Oct. 1987.

[126] S. Tang, A. J. Freeman, and G. B. Olson, "Phosphorus-induced relaxation in an iron grain-boundary - a cluster-model study," *Physical Review B*, vol. 47, no. 5, pp. 2441–2445, Feb. 1993.

[127] V. Breger and E. Gileadi, "Adsorption and absorption of hydrogen in palladium," *Electrochimica Acta*, vol. 16, no. 2, pp. 177–190, Feb. 1971.

[128] M. Boudart and H. S. Hwang, "Solubility of hydrogen in small particles of palladium," *Journal of Catalysis*, vol. 39, no. 1, pp. 44–52, Jan. 1975.

[129] H. Conrad, G. Ertl, and E. E. Latta, "Adsorption of hydrogen on palladium single-crystal surfaces," *Surface Science*, vol. 41, no. 2, pp. 435–446, Feb. 1974.

[130] J. F. Paul and P. Sautet, "Density-functional periodic study of the adsorption of hydrogen on a palladium (111) surface," *Physical Review B*, vol. 53, no. 12, pp. 8015–8027, Mar. 1996.

[131] M. G. Cattania, V. Penka, R. J. Behm, K. Christmann, and G. Ertl, "Interaction of hydrogen with a palladium (110) surface," *Surface Science*, vol. 126, no. 1-3, pp. 382–391, Mar. 1983.

[132] D. Lupu, A. R. Biris, I. Misan, A. Jianu, G. Holzhuter, and E. Burkel, "Hydrogen uptake by carbon nanofibers catalyzed by palladium," *International Journal of Hydrogen Energy*, vol. 29, no. 1, pp. 97–102, Jan. 2004.

[133] S. Uemiya, N. Sato, H. Ando, Y. Kude, T. Matsuda, and E. Kikuchi, "Separation of hydrogen through palladium thin-film supported on a porous-glass tube," *Journal of Membrane Science*, vol. 56, no. 3, pp. 303–313, Mar. 1991.

[134] K. J. Bryden and J. Y. Ying, "Nanostructured palladium-iron membranes for hydrogen separation and membrane hydrogenation reactions," *Journal of Membrane Science*, vol. 203, no. 1-2, pp. 29–42, Jun. 2002.

[135] T. L. Ward and T. Dao, "Model of hydrogen permeation behavior in palladium membranes," *Journal of Membrane Science*, vol. 153, no. 2, pp. 211–231, Feb. 1999.

[136] B. D. Morreale, M. V. Ciocco, R. M. Enick, B. I. Morsi, B. H. Howard, A. V. Cugini, and K. S. Rothenberger, "The permeability of hydrogen in bulk palladium at elevated temperatures and pressures," *Journal of Membrane Science*, vol. 212, no. 1-2, pp. 87–97, Feb. 2003.

[137] F. Favier, E. C. Walter, M. P. Zach, T. Benter, and R. M. Penner, "Hydrogen sensors and switches from electrodeposited palladium mesowire arrays," *Science*, vol. 293, no. 5538, pp. 2227–2231, Sep. 2001.

[138] S. F. Yu, U. Welp, L. Z. Hua, A. Rydh, W. K. Kwok, and H. H. Wang, "Fabrication of palladium nanotubes and their application in hydrogen sensing," *Chemistry of Materials*, vol. 17, no. 13, pp. 3445–3450, Jun. 2005.

[139] S. Mubeen, T. Zhang, B. Yoo, M. A. Deshusses, and N. V. Myung, "Palladium nanoparticles decorated single-walled carbon nanotube hydrogen sensor," *Journal of Physical Chemistry C*, vol. 111, no. 17, pp. 6321–6327, May. 2007.

[140] S. Kishore, J. A. Nelson, J. H. Adair, and P. C. Eklund, "Hydrogen storage in spherical and platelet palladium nanoparticles," *Journal of Alloys and Compounds*, vol. 389, no. 1-2, pp. 234–242, May 2005.

[141] M. Yamauchi, R. Ikeda, H. Kitagawa, and M. Takata, "Nanosize effects on hydrogen storage in palladium," *Journal of Physical Chemistry C*, vol. 112, no. 9, pp. 3294–3299, May 2008.

[142] P. F Timmins, *Solutions to Hydrogen Attack in Steels*, Ohio: Materials Park, 1997.

[143] A. Turnbull, *Hydrogen Transport and Cracking in Metals: Proceedings of a Conference Held at the National Physical Laboratory*, London : Institute of Materials, 1995.

[144] G. Lu and E. Kaxiras, "Hydrogen embrittlement of aluminum: The crucial role of vacancies," *Physical Review Letter*, vol. 94, no. 15, pp. 155501, Apr. 2005.

[145] Y. Fukai, Y. Ishii, Y. Goto, and K. Watanabe, "Formation of superabundant vacancies in Pd-H alloys," *Journal of Alloys and Compounds*, vol. 313, no. 1-2, pp. 121–132, Dec. 2000.

[146] Y. Fukai, "Formation of superabundant vacancies in M-H alloys and some of its consequences: A review," *Journal of Alloys and Compounds*, vol. 356-357, pp. 263–269, Aug. 2003.

[147] Y. Fukai and N. Okuma, "Formation of superabundant vacancies in Pd hydride under high hydrogen pressures," *Physical Review Letter*, vol. 73, no. 12, pp. 1640–1643, Sep. 1994.

[148] G. M. Bond, I. M. Robertson, and H. K. Birnbaum, "On the mechanisms of hydrogen embrittlement of Ni3Al alloys," *Acta Metallurgica*, vol. 37, no. 5, pp. 1407–1413, May 1989.

[149] C. T. Liu, "Environmental embrittlement and grain-boundary fracture in Ni3Al," *Scripta Metallurgica et Materialia*, vol. 27, no. 1, pp. 25–28, Jul. 1992.

[150] S. M. Myers, M. I. Baskes, H. K. Birnbaum, J. W. Corbett, G. G. Deleo, S. K. Estreicher, E. E. Haller, P. Jena, N. M. Johnson, R. Kirchheim, S. J. Pearton, and M. J. Stavola, "Hydrogen interactions with defects in crystalline solids," *Reviews of Modern Physics*, vol. 64, no. 2, pp. 559–617, Apr. 1992.

[151] W. T. Geng, A. J. Freeman, and G. B. Olson, "Influence of alloying additions on grain boundary cohesion of transition metals: First-principles determination and its phenomenological extension," *Physical Review B*, vol. 63, no. 16, pp. 165415, Apr. 2001.

[152] O. Yu. Vekilova, D. I. Bazhanov, S. I. Simak, and I. A. Abrikosov, "First-principles study of vacancy-hydrogen interaction in Pd," *Physical Review B*, vol. 80, no. 2, pp. 024101, Jul. 2009.

[153] Y. Kraftmakher, "Equilibrium vacancies and thermophysical properties of metals," *Physics Reports*, vol. 299, no. 2-3, pp. 80–188, Jun. 1998.

[154] W. T. Geng, A. J. Freeman, G. B. Olson, Y. Tateyama, and T. Ohno, "Hydrogen-promoted grain boundary embrittlement and vacancy activity in metals: Insights from ab initio total energy calculatons," *Materials Transactions*, vol. 46, no. 4, pp. 756–760, Apr. 2005.

[155] L. P. Zhong, R. Q. Wu, A. J. Freeman, and G. B. Olson, "Charge transfer mechanism of hydrogen-induced intergranular embrittlement of iron," *Physical Review B*, vol. 62, no. 21, pp. 13938–13941, Dec. 2000.

[156] S. S. Kulkov, S. V. Eremeev, and S. E. Kulkova, "Theoretical study of hydrogen absorption near symmetric tilt grain boundaries in Pd and TiFe," *Technical Physics*, vol. 54, no. 8, pp. 1204–1209, Aug. 2009.

[157] M. Osawa, H. Shiraishi, T. Yokokawa, H. Harada, and T. Kobayashi, "3D-FEM calculations of rafting in Ni-base superalloys based and high temperature elastic and lattice parameters," in *Superalloys*, K. A. Green, T. M. Pollock, H. Harada, T. E. Howson, R. C. Reed, J. J. Schirra, and S. Walston, Eds. Pennsylvania: TMS, 2004, pp. 977-982.

[158] D. Gerlich and E. S. Fisher, "The high temperature elastic moduli of aluminum," *Journal of Physics and Chemistry of Solids*, vol. 30, no. 5, pp. 1197–1205, May 1969.

[159] G. N. Kamm and G. A. Alers, "Low-temperature elastic moduli of aluminum," *Journal of Applied Physics*, vol. 35, no. 2, pp. 327–331, Jul.1964.

[160] P. M. Sutton, "The variation of the elastic constants of crystalline aluminum with temperature between 63K and 773K," *Physical Review*, vol. 91, no. 4, pp. 816–821, Apr. 1953.

[161] A. Tallon, "Temperature dependence of the elastic constants of aluminum," *Journal of Physics and Chemistry of Solids*, vol. 40, no. 11, pp. 831–837, Mar. 1979.

[162] R. Arroyave, D. Shin, and Z. K. Liu, "Ab initio thermodynamic properties of stoichiometric phases in the Ni-Al system," *Acta Materialia*, vol. 53, no. 6, pp. 1809–1819, Apr. 2005.

[163] F. Cleri and V. Rosato, "Lattice dynamics of ordered and disordered Cu3Au with a tight-binding potential model," *Philosophical Magazine Letters*, vol. 67, no. 6, pp. 369–378, Jun. 1993.

[164] M. Forsblom, N. Sandberg, and G. Grimvall, "Anharmonic effects in the heat capacity of Al," *Physical Review B*, vol. 69, no. 16, pp. 165106, Apr. 2004.

[165] M. Forsblom and G. Grimvall, "Heat capacity of liquid Al: Molecular dynamics simulations," *Physical Review B*, vol. 72, no. 13, pp. 132204, Oct. 2005.

[166] B. Grabowski, L. Ismer, T. Hickel, and J. Neugebauer, "Ab initio up to the melting point: Anharmonicity and vacancies in aluminum," *Physical Review B*, vol. 79, no. 13, pp. 134106, Apr. 2009.

[167] M. Kresch, M. Lucas, O. Delaire, J. Y. Y. Lin, and B. Fultz, "Phonons in aluminum at high temperatures studied by inelastic neutron scattering," *Physical Review B*, vol. 77, no. 2, pp. 24301, Jan. 2008.

[168] M. Zoli and V. Bortolani, "Thermodynamic properties of FCC metals: Cu and Al," *Journal of Physics: Condensed Matter*, vol. 2, no. 3, pp. 525–539, Jan. 1990.

[169] M. Radovic, E. Lara-Curzio, and L. Riester, "Comparison of different experimental techniques for determination of elastic properties of solids," *Materials Science and Engineering*, vol. 368, no. 1-2, pp. 56–70, Mar. 2004.

[170] T. Cagin, G. Dereli, M. Uludogan, and M. Tomak, "Thermal and mechanical properties of some fcc transition metals," *Physical Review B*, vol. 59, no. 5, pp. 3468–3473, Feb. 1999.

[171] G. Dereli, T. Cagin, M. Uludogan, and M. Tomak, "Thermal and mechanical properties of Pt-Rh alloys," *Philosophical Magazine Letters*, vol. 75, no. 4, pp. 209–217, Apr. 1997.

[172] H. H. Kart, M. Tomak, and T. Cagin, "Thermal and mechanical properties of Cu-Au intermetallic alloys," *Modelling and Simulation in Materials Science and Engineering*, vol. 13, no. 5, pp. 657–669, Jul. 2005.

[173] M. S. Daw and M. I. Baskes, "Semiempirical, quantum mechanical calculation of hydrogen embrittlement in metals," *Physical Review Letter*, vol. 50, no. 17, pp. 1285–1288, Apr. 1983.

[174] W. Zhong, Y. Cai, and D. Tomanek, "Computer-simulation of hydrogen embrittlement in metals," *Nature*, vol. 362, no. 6419, pp. 435–437, Apr. 1993.

[175] B. Coluzzi, C. Costa, P. Marzola, and F. M. Mazzolai, "Elastic constants of a Pd85Pt15 single-crystal containing hydrogen," *Journal of Physics*, vol. 1, no. 36, pp. 6335–6342, Sep. 1989.

[176] Y. K. Tovbin and E. V. Votyakov, "Evaluation of the influence of dissolved hydrogen on mechanical properties of palladium," *Physics of the Solid State*, vol. 42, no. 7, pp. 1192–1195, Jul. 2000.

[177] M. S. Daw, S. M. Foiles, and M. I. Baskes, "The embedded-atom method - a review of theory and applications," *Materials Science Reports*, vol. 9, no. 7-8, pp. 251–310, Mar. 1993.

[178] M. I. Baskes and M. S. Daw, "Applications of the embedded atom method to hydrogen embrittlement," *Journal of Metals*, vol. 37, no. 8, pp. A22–A22, May 1985.

[179] R. W. Smith and G. S. Was, "Application of molecular dynamics to the study of hydrogen embrittlement in Ni-Cr-Fe alloys," *Physical Review B*, vol. 40, no. 15, pp. 10322–10336, Nov. 1989.

[180] X. J. Xu, M. Wen, S. Fukuyama, and K. Yokogawa, "Simulation of hydrogen embrittlement at crack tip in nickel single crystal by embedded atom method," *Materials Transactions*, vol. 42, no. 11, pp. 2283–2289, Nov. 2001.

[181] M. Shiga, M. Yamaguchi, and H. Kaburaki, "Structure and energetics of clean and hydrogenated ni surfaces and symmetrical tilt grain boundaries using the embedded-atom method," *Physical Review B*, vol. 68, no. 24, pp. 245402, Dec. 2003.

[182] X. W. Zhou, J. A. Zimmerman, B. M. Wong, and J. J. Hoyt, "An embedded-atom method interatomic potential for Pd-H alloys," *Journal of Materials Research*, vol. 23, no. 3, pp. 704–718, Mar. 2008.

[183] R. Zugic, B. Szpunar, V. D. Krstic, and U. Erb, "Effect of porosity on the elastic response of brittle materials: An embedded-atom method approach," *Philosophical Magazine A - Physics of Condensed Matter Structure Defects and Mechanical Properties*, vol. 75, no. 4, pp. 1041–1055, Apr. 1997.

[184] J. Li, "Atomeye: An efficient atomistic configuration viewer," *Modelling and Simulation in Materials Science and Engineering*, vol. 11, no. 2, pp. 173–177, Mar. 2003.

[185] D. S. Shih, I. M. Robertson, and H. K. Birnbaum, "Hydrogen embrittlement of alpha-titanium - insitu tem studies," *Acta Metallurgica*, vol. 36, no. 1, pp. 111–124, Jan. 1988.

[186] J. R. Asay and M. Shahinpoor, *High-Pressure Shock Compression of Solids*, New York: Springer-Verlag, 1993.

[187] A. Sawaoka, *Shock Waves in Materials Science*, New York: Springer-Verlag, 1993.

[188] T. C. Germann, B. L. Holian, P. S. Lomdahl, and R. Ravelo, "Orientation dependence in molecular dynamics simulations of shocked single crystals," *Physical Review Letter*, vol. 84, no. 23, pp. 5351–5354, Jun. 2000.

[189] E. M. Bringa, A. Caro, Y. M. Wang, M. Victoria, J. M. McNaney, B. A. Remington, R. F. Smith, B. R. Torralva, and H. Van Swygenhoven, "Ultrahigh strength in nanocrystalline materials under shock loading," *Science*, vol. 309, no. 5742, pp. 1838–1841, Sep. 2005.

[190] E. M. Bringa, A. Caro, M. Victoria, and N. Park, "The atomistic modeling of wave propagation in nanocrystals," *Journal of the Minerals, Metals and Materials Society*, vol. 57, no. 9, pp. 67–70, Sep. 2005.

[191] V. Dremov, A. Petrovtsev, P. Sapozhnikov, M. Smirnova, D. L. Preston, and M. A. Zocher, "Molecular dynamics simulations of the initial stages of spall in nanocrystalline copper," *Physical Review B*, vol. 74, no. 14, pp. 144110, Oct. 2006.

[192] S. G. Srinivasan, M. I. Baskes, and G. J. Wagner, "Atomistic simulations of shock induced microstructural evolution and spallation in single crystal nickel," *Journal of Applied Physics*, vol. 101, no. 4, pp. 043504, Feb. 2007.

[193] V. V. Stegailov and A. V. Yanilkin, "Structural transformations in single-crystal iron during shock-wave compression and tension: Molecular dynamics simulation," *Journal of Experimental and Theoretical Physics*, vol. 104, no. 6, pp. 928–935, Jun. 2007.

[194] C. Pozzi, T. C. Germann, and R. G. Hoagland, "Molecular dynamics simulation of dislocation emission from shocked aluminum grain boundaries," in *Shock Compression of Condensed Matter*. New York: AIP Conference Proceedings, 2009, pp. 765-768.

[195] B. Arman, S.-N. Luo, T. C. Germann, and T. Cagin, "Dynamic response of Cu46Zr54 metallic glass to high-strain-rate shock loading: Plasticity, spall, and atomic-level structures," *Physical Review B*, vol. 81, no. 14, pp. 144201, Apr. 2010.

[196] S.-N. Luo, T. C. Germann, T. G. Desai, D. L. Tonks, and Q. An, "Anisotropic shock response of columnar nanocrystalline Cu," *Journal of Applied Physics*, vol. 107, no. 5, pp. 123507, Jun. 2010.

[197] S.-N. Luo, T. C. Germann, D. L. Tonks, and Q. An, "Shock wave loading and spallation of copper bicrystals with asymmetric sigma 3 (110) tilt grain boundaries," *Journal of Applied Physics*, vol. 108, no. 9, pp. 093526, Nov. 2010.

[198] B. Arman, Q. An, S.-N. Luo, T. G. Desai, D. L. Tonks, T. Cagin, and W. A. Goddard III, "Dynamic response of phenolic resin and its carbon-nanotube composites to shock wave loading," *Journal of Applied Physics*, vol. 109, no. 1, pp. 013503, Jan. 2011.

[199] V. V. Dremov, Ph. A. Sapozhnikov, and E. M. Bringa, "Molecular dynamics simulation of interaction between shock wave and high-symmetry intergranular boundary," in *Shock Compression of Condensed Matter*. New York: AIP Conference Proceedings, 2006, pp. 387-390.

[200] C. L. Kelchner, S. J. Plimpton, and J. C. Hamilton, "Dislocation nucleation and defect structure during surface indentation," *Physical Review B*, vol. 58, no. 17, pp. 11085, Nov. 1998.

[201] A. Hasnaoui, H. Van Swygenhoven, and P. M. Derlet, "Cooperative processes during plastic deformation in nanocrystalline fcc metals: A molecular dynamics simulation," *Physical Review B*, vol. 66, no. 18, pp. 184112, Nov. 2002.

VITA

Hieu Hong Pham grew up in the harbor city of Hai Phong, Vietnam. He earned his undergraduate degree at Gubkin Russian State University of Oil and Gas in June, 2004, specializing in chemical technology of natural energy resources and carbonaceous materials. In 2006, he entered Texas A&M University in College Station to pursue a doctoral degree in Chemical Engineering. While at Texas A&M, his research focused on using advanced molecular simulation techniques to study materials sciences, physics and chemistry phenomena. His received his Ph.D. in August 2011 and was appointed to a postdoctoral research associate position at Materials Science and Technology Division, Los Alamos National Laboratory, New Mexico, 87544. He can also be reached via email at hieuhpham@gmail.com